Fall 12-2021

Phytoplankton Community Response to Upwelling Events: Distribution and Abundance Investigated Using Genomic Methods

Sveinn V. Einarsson
Old Dominion University, sveinn.einars@gmail.com

PHYTOPLANKTON COMMUNITY RESPONSE TO UPWELLING EVENTS:

DISTRIBUTION AND ABUNDANCE INVESTIGATED USING GENOMIC METHODS

by

Sveinn V. Einarsson
B.S. May 2016, Old Dominion University
M.S. August 2018, Old Dominion University

A Dissertation Submitted to the Faculty of
Old Dominion University in Partial Fulfillment of the
Requirements for the Degree of

DOCTOR OF PHILOSOPHY

OCEANOGRAPHY

OLD DOMINION UNIVERSITY
December 2021

Approved by:

P. Dreux Chappell (Director)

Sophie Clayton (Member)

Holly Gaff (Member)

ABSTRACT

PHYTOPLANKTON COMMUNITY RESPONSE TO UPWELLING EVENTS: DISTRIBUTION AND ABUNDANCE INVESTIGATED USING GENOMIC METHODS

Sveinn V. Einarsson
Old Dominion University, 2021
Director: Dr. P. Dreux Chappell

Upwelling events are known to support blooms of phytoplankton, important primary producers at the base of the oceanic food web. Phytoplankton community structure changes in response to upwelling support higher trophic level growth and increased efficiency of carbon export from the euphotic zone. While these events occur globally, this study examined upwelling in coastal regions, where alongshore winds can drive Ekman transport and upwelling of deeper waters. The two upwelling regimes examined were the California Current System and the Alaskan Beaufort Sea. In the California Current System, the relative diatom community composition was examined using 18S sequencing to determine how diatoms respond to two physically and chemically different upwelling plumes. Results showing that different species of diatoms responded to each upwelling event were discussed in the context of future predictions of diatom proliferation, transport, and carbon export in the California Current System. Upwelling in the Beaufort Sea is becoming more frequent as sea ice melts and the Arctic becomes warmer. The upwelling system in the Beaufort Sea was examined during three upwelling events, specifically focusing on how the phytoplankton community on the shelf responded to upwelling, through sequencing of the 18S v9 region of eukaryotic DNA. Before the first upwelling event *Alexandrium tamerense,* a dinoflagellate known for its ability to produce the neurotoxin that

causes paralytic shellfish poisoning, dominated sequencing reads. Once upwelling began, the relative abundance of *Alexandrium* sequences disappeared and was replaced by elevated relative sequence abundance of diatoms, picoeukarytoes, and other dinoflagellates. While these results indicate expansion of a possible harmful algae further into the Arctic than previously seen, likely because of climate warming, they also suggest that upwelling events can lead to the proliferation of other phytoplankton, which could in turn diminish the prominence of this harmful algae. The implications of how this dynamic system may change due to increasing strength and number of upwelling events were discussed. Overall, these results underscore the importance of understanding the response of phytoplankton community composition to coastal sub mesoscale dynamics such as upwelling, which is of particular interest given upwelling is predicted to change in a warming climate.

This dissertation is dedicated to my wife, Hannah, my happiness, and to my family for their unwavering support throughout the years.

ACKNOWLEDGMENTS

I would like to acknowledge my advisor Dreux Chappell, who introduced me to research in Oceanography, and her continuous support throughout my research and graduate schoolwork. To think that 15 years ago, I was working in a fishing net factory in a small town in Iceland and 15 years later I've visited 6 continents in support of researching Oceanography, is amazing to me. I have Dreux to thank for all of it. I'd like to thank my wife, Hannah, for her support and always believing in me. My pug chop, Noi, for all his snorts and fun walks. My family for always being supportive, even though they don't really know what I do. My mom and dad, for their advice and encouragement, and giving me the right ratio of carelessness and motivation to make me successful. Thank you to all the members of the research cruises I went on, NBP16-08 GEOTRACES GP15, and SCALE 2019, for amazing experiences.

I'd like to acknowledge the faculty in the Ocean and Earth Sciences department for their support and guidance and to my committee members, Holly Gaff, Sophie Clayton, and Richard Zimmerman, who put me on a path to be successful. Sophie Clayton for introducing me to machine learning, and techniques to explain physical dynamics of my study sites. Kim Powell and Zuzy Abdala, who made lab work fun and for all of our chats throughout the years. I'd also like to thank Dan Barshis of the ODU Biology Department, whose computing course was one of the most useful courses I could've taken.

I'd like to thank Kate Lowry, for collecting samples and all her amazing work aboard the R/V *Sikuliaq*, without which this project would not have been possible, and the Ocean Carbon Biogeochemistry Summer Workshop and early career funding, which allowed for Kate and I to meet and ultimately collaborate. Carin Ashjian for the collaboration to collect the samples, Peigen Lin and Robert Pickart for their mooring data and analysis supporting the physical

dynamics, without which the dataset would've been lacking. I would thank the captain, crew, and marine science technicians of the R/V *Sikuliaq* for facilitating sample collection, Kim Powell for assisting in DNA sample processing, and Steve Okkonen for help determining the physical dynamics of the upwelling event, Amala Mahadevan for the use of her SUNA V2 nitrate sensor, and Laurie Juranek for analyzing the nitrate samples that we collected. Funding for this work was provided by awards from the Jeffress Trust Awards Program in Interdisciplinary Research to P. Dreux Chappell, the Jacques S. Zaneveld endowed scholarship to Sveinn V. Einarsson, and the Weston Howland Jr. Postdoctoral Scholarship and WHOI Access to Sea Fund to Kate Lowry. Fieldwork was supported in part by National Science Foundation (NSF) grant PLR-1603941 (CA). A portion of the analysis was funded by NSF grant OPP-1733564 and National Oceanic and Atmospheric Administration grant NA14OAR4320158 (Peigin Lin and Robert Pickart). The Dorothy Brown Smith Travel fund for allowing conference attendance and the ability to collaborate with so many people. I'd also like to thank Ken Bruland, chief scientist of the IRN-BRU cruise and the captain and crew of the R/V Melville. Funding for this work was provided by awards from the VA Space Grant Consortium New Investigator Program and the National Science Foundation (NSF) OCE-1524482 to P. Dreux Chappell. Ship time as well as the nutrient and trace metal measurements by Tyler Coale and Claire Till, respectively, were supported by NSF award OCE-1259776 to Ken Bruland.

NOMENCLATURE

ACW	Atlantic Coastal Current
AON	Arctic Observing Network
AW	Atlantic Water
BDL	Below detection limit
BH	Beaufort High
BS	Beaufort Sea
BSW	Bering Summer Water
CCS	California Current System
CO_2	Carbon dioxide
dFe	Dissolved Iron
DNQ	Did not quantify
ELOD	Effective limit of detection
ELOQ	Effective limit of quantification
NO_3	Nitrate
OA	Okadaic acid
PO_4	Phosphate
SiO_4	Silicate

SST Sea Surface Temperature

SSH Sea Surface Height

TABLE OF CONTENTS

Page

Page

LIST OF TABLES

LIST OF FIGURES

Figure Page

CHAPTER I

BACKGROUND AND RATIONALE

Understanding the effect upwelling has on the marine phytoplankton community is important as their primary production supports higher trophic levels (Falk-Petersen *et al.*, 2015) and has the capacity to enhance carbon export (Hendy, 2015). Upwelling events in areas of Eastern Boundary Currents are especially productive (Cushing, 1971; Tenore *et al.*, 1995; Jackson *et al.*, 2011; Iles *et al.*, 2012) and support 50% of global fish production (Johnson *et al.*, 1999). One of these regions, the eastern equatorial Pacific, accounts for 20-50% of global new biological production (Loubere, 2000). Recent work suggests that upwelling events are predicted to become stronger, less frequent, and longer in duration due to climate change (Iles *et al.*, 2012). Implications of which will change carbon export in one of the most productive areas in the ocean. This dissertation seeks to examine how the phytoplankton community changes in response to upwelling events. In addition, several important factors related to upwelling that could influence phytoplankton community composition will be addressed.

Phytoplankton blooms can occur due to light availability, stratification or in response to a pulse of nutrients, such as those that occur in upwelling or water mass mixing events (Degerlund and Eilertsen, 2010; Gerringa *et al.*, 2012). Coastal upwelling is primarily observed due to favorable wind direction resulting in Ekman transport (Bravo *et al.*, 2016). As the coastal surface waters move offshore, colder and deeper water takes its place at the surface often resulting in a temperature decrease of up to 5°C (Ganachaud *et al.*, 2010). The cold upwelled water is nutrient rich, which drives phytoplankton growth (Davis *et al.*, 2014). Each upwelling event can be different based on factors such as weather, which can influence the length and duration of the

wind event, as well as topography. Topography can affect the composition of the water mass that is being upwelled, for example some water masses are in contact with sediments on continental shelves which can lead to micronutrients, such as iron, getting entrained in the water (Gerringa *et al.*, 2012). The amount of iron entrained in upwelled waters is of importance as iron has been found to be the limiting nutrient for multiple phytoplankton groups in large regions of the surface ocean (Moore *et al.*, 2004). The length of time bottom water is in contact with the sediment also affects the chemical composition of the water mass, where thin continental shelves are associated with lower micronutrient concentrations and wider continental shelves are associated with higher micronutrient concentrations in the bottom water mass that is upwelled (Bruland *et al.*, 2001). As a water mass reaches the surface through upwelling, the chemical composition of that water mass may, in turn, affect the phytoplankton responding to the influx of nutrients. Along the California coast, for example, upwelling occurring near thin continental shelf regions has been associated with iron limitation, while upwelling over a broad continental shelf region has been found to be iron replete (Hutchins and Bruland, 1998; Bruland *et al.*, 2001; Biller *et al.*, 2013). These prior results suggest that both geography and topography surrounding an upwelling area need to be kept in mind when predicting phytoplankton community shifts in response to upwelling. While phytoplankton blooms are associated with upwelling (Kiørboe *et al.*, 1998), it has been found that changes in new production in the eastern equatorial Pacific has been associated more with the chemical composition of the upwelled water than the upwelling itself (Loubere, 2000). Indicating that the chemical composition of upwelling is important to predict phytoplankton response to upwelling.

A phytoplankton group of particular interest is the diatoms. Diatoms are unicellular photosynthetic eukaryotes known to grow faster than other phytoplankton in nutrient replete

conditions, that have the ability to respond quickly to nutrient pulses, allowing them to bloom in upwelling environments (Biller *et al.*, 2013). Diatoms have evolved from deeper more turbid environments on the shelf, making them uniquely suited to respond to upwelling events (Benoiston *et al.*, 2017), which are well mixed and likely lead to resuspension of sediments if the upwelling originates from the sediment surface. They are known to have a tendency to aggregate after a bloom leading to high sedimentation (Kiørboe *et al.*, 1998) either through sinking or as part of grazer fecal pellets (Korb *et al.*, 2012). Even though diatoms tend to bloom for short periods of time they account for most of the annual net primary production in the oceans, especially in polar oceans (Krause *et al.*, 2019). In addition to low iron potentially causing shifts in diatom community (Chappell *et al.*, 2019), as certain diatom species are able to survive and even have a high growth rate in low iron conditions (Armbrust 2009 and references therein), it has been observed that when upwelling occurs over a thin shelf associated with low iron concentrations, such as Big Sur, California or off the coast of Oregon, the resulting diatom blooms are more siliceous and sink faster (Hutchins and Bruland, 1998). This change in diatom ballasting is an indicator of iron limitation, as silicic acid is preferentially taken up compared to nitrate in iron limited waters (Brzezinski *et al.*, 2015) leading to possible high sedimentation due to heavier diatoms in low iron upwelling. Carbon export can depend on the diatom species and amount of silicification, or how much silicic acid they take up. Diatoms have a silica cell wall, which can lead to more carbon export when diatom blooms sink as their silica exoskeleton creates an additional barrier to bacterial degradation that is not found in other phytoplankton (Kiørboe *et al.* 1998). Additionally, the heavier a phytoplankton is, the faster its sinking speed, the more likely it is to sink below the euphotic zone without being remineralized or grazed upon (Hilligsøe *et al.* 2011) and more silicification will increase the mass of a diatom cell.

Larger diatom cells account for most of the biogenic silica production in the diatom population (McNair *et al.* 2018) but they have a growth rate that is usually slower than that of smaller diatoms. A recent study found that the diatom population in an upwelling plume was dominated by medium sized and faster growing diatoms, such as of the *Chaetoceros* genus, which were found to account for most of the biogenic silica production in the recently upwelled water but their importance to silica production waned as the plume moved further offshore and nutrients were depleted (McNair *et al.* 2018). Generally, *Chaetoceros* is predominantly found in nutrient replete areas (Assmy *et al.*, 2007; Hoffmann *et al.*, 2008) and is known to efficiently export carbon once nutrients are depleted because their resting spores aggregate together and lead to grazer resistant sinking pellets (Hendy, 2015). The fact that some diatoms contribute more to export production than others and that they may have different impacts on silica cycling underscores the importance of understanding how these phytoplankton communities respond to upwelling events. Chapter II examines CCS upwelling, where two upwelling plumes with different initial iron concentrations were sampled. The low iron upwelling transect began west of Cape Bianco over the shelf slope and the high iron upwelling transect began on the shelf north-west of the San Francisco Bay area.

Individual phytoplankton traits have been used to explain the dominance or presence of a phytoplankton species in a specific spatial environment (Krause *et al.*, 2020), so it is also important to consider how physical processes affect the phytoplankton community. For example, when upwelling occurs Ekman transport moves water offshore and deeper water takes its place (Jacox *et al.*, 2018). Additionally, upwelling events can lead to changing the direction of prevailing currents in a region, which may laterally transport phytoplankton communities from other areas (Rossi *et al.*, 2008). In general, the CCS is a physically dynamic region with shifting

currents and eddies that transport parcels of from the coast offshore. How these physical dynamics influence both nutrient availability and the dispersal of phytoplankton and their resulting impact on diatom community composition in the CCS will be addressed in chapter II.

Upwelling in the Beaufort Sea (BS) is due to a shift from westerly to easterly winds, which results in the reversal of the direction of the shelfbreak jet (Pickart *et al.*, 2011). When a BS upwelling event occurs, instead of transporting surface water from the West, the prevailing current reverses bringing in colder surface water from the East and nutrient rich deeper water originating from the Atlantic is also upwelled (Pickart *et al.*, 2009). In addition to the effect that nutrient pulses have on the phytoplankton community, these physical processes can influence phytoplankton community composition by transporting phytoplankton in from other areas and/or mixing of adjacent water masses. This is especially influential in the Arctic, where heat transport is predicted to increase into the Arctic with the Bering Strait (BS) counting for most of the imported heat (Marshall *et al.*, 2014; Marshall *et al.*, 2015). The shelfbreak jet connects the Alaskan Coastal Current (ACC) to the Alaskan BS shelf, connecting the heat import through the BS to our study site on the Alaskan BS shelf and shelfbreak. Chapter III specifically addresses how the increasingly warmer surface currents bringing warm Pacific surface water into the Alaskan BS is influencing dispersal into the region of normally temperate dinoflagellates. In the context of upwelling, this dispersal ceases once upwelling begins, indicating competing physical dynamics that are both changing due to climate change.

Beaufort Sea upwelling is primarily driven by prolonged easterly winds and is strongest when there is less sea ice (Schulze and Pickart, 2012). If there is a sustained easterly wind for over 8 hours it will lead to upwelling of saltier nutrient rich Atlantic Water (AW) onto the shelf (Pickart *et al.*, 2013a). In the past, there were years when the BS would stay completely ice

covered throughout the year, but as a result of the warming climate the BS shelf has seen retreating sea ice cover and an increase in upwelling strength leading to an increase in primary production in the fall (Schulze and Pickart, 2012). As a result, the winds that drive the upwelling in the BS are becoming more frequent (Pickart *et al.*, 2013a). As sea ice in the Arctic continues to retreat, it can be predicted that the increase of nutrient rich upwelling water as a result of more frequent upwelling events will drive blooms of diatoms and copepods, which in turn will feed bowhead whales, other marine mammals, and seabirds (Falk-Petersen *et al.*, 2015). Chapter IV will examine samples collected during 3 separate upwelling events that occurred across the shelfbreak in the Alaskan BS region, specifically focusing on how the phytoplankton community on the shelf shifts in response to these events. While diatoms are important in coastal upwelling communities, which is why they were the focus of the CCS study (chapter II), they are not the only phytoplankton found there. Thus, chapter IV will also examine BS upwelling and changes to the greater eukaryotic phytoplankton community, more specifically, picoeukaryotes, dinoflagellates and haptophytes, which together with diatoms account for most of the eukaryotic phytoplankton found in today's coastal oceans (Benoiston *et al.*, 2017).

Sampling upwelling events can be challenging as the events themselves are difficult to predict, being that they usually develop during upwelling favorable coastal winds from displaced high-low pressure dipoles (Pitcher *et al.*, 2010). Thus, it is difficult to plan an expedition to sample such an event. That said, satellite remote sensing of sea surface temperature and salinity can be used to determine if an event is occurring or has recently occurred. The overarching goal of this project is to analyze how the phytoplankton communities are influenced by the different conditions of each upwelling event with the goal of finding common causes of changes to the phytoplankton community in response to upwelling. Being able to predict how the phytoplankton

community responds to these events will, in turn, enable better predictions of carbon export in some of the most productive regions of the ocean.

CHAPTER II

DIATOM COMMUNITY RESPONSE TO TWO UPWELLING PLUMES IN THE CALIFORNIA CURRENT SYSTEM

INTRODUCTION

The California Current System (CCS) is an especially productive area known for upwelling events that cause phytoplankton blooms along the coast of California (Bruland *et al.*, 2001). The CCS is a physically dynamic region with shifting winds, meandering eddies, and variable currents often dependent on climate modes such as El Nino-Southern Oscillation (Kahru *et al.*, 2018; Xiu *et al.*, 2018). These physical dynamics are predicted to change due to climate change with increased stratification and stronger upwelling expected to occur in the CCS (Xiu *et al.*, 2018). Along the California coast, upwelling occurring near narrow continental shelf regions has been associated with iron limitation, while upwelling over a broad continental shelf region has been found to be iron replete (Hutchins and Bruland, 1998; Bruland *et al.*, 2001; Biller *et al.*, 2013). Iron is well known to limit growth for multiple different phytoplankton groups in the ocean (Moore *et al.*, 2004) and especially for diatoms who almost exclusively need nitrate reductase for nitrogen uptake, an iron expensive enzyme (Marchetti and Maldonado, 2016; Sutak *et al.*, 2020). While phytoplankton blooms are associated with upwelling (Kiørboe *et al.*, 1998), changes in past new production in the eastern equatorial Pacific have been associated more with the chemical composition of the upwelled water than wind driven changes to upwelling rates (Loubere, 2000). These prior results suggest both nearby geography and topography surrounding

an upwelling area, which influence iron concentration in upwelling plumes, need to be kept in mind when predicting phytoplankton community shifts in response to upwelling.

Diatoms are unicellular photosynthetic eukaryotes known to grow faster than other phytoplankton, that have the ability to respond quickly to nutrient pulses, allowing them to bloom in upwelling environments (Biller *et al.*, 2013). Diatoms have evolved from deeper more turbid environments on the shelf, making them uniquely suited to respond to upwelling events (Benoiston *et al.*, 2017). They are known to have an affinity to aggregate after a bloom leading to high sedimentation (Kiørboe *et al.*, 1998) either through sinking or as part of grazer fecal pellets (Korb *et al.*, 2012). Even though diatoms tend to bloom for short periods of time, they account for most of the annual net primary production in some regions of the global ocean, such as the Arctic (Krause *et al.*, 2019). A recent study off the California coast, which included both transects in this study though examined via optical methods, found that the diatom population in an upwelling plume was dominated by medium sized and faster growing diatoms, such as of the *Chaetoceros* genus, which accounted for most of the biogenic silica production in recently upwelled water though their importance to silica production waned as the plume moved further offshore (McNair *et al.*, 2018). *Chaetoceros* diatoms are known to efficiently export carbon because they generate resting spores that aggregate together and lead to grazer resistant sinking pellets once nutrients are depleted (Smetacek, 1999; Hendy, 2015).

The fact that some diatoms contribute more to carbon export than others and as a result influence nutrient cycling of biogenic elements such as silica (Ragueneau *et al.*, 2000) underscores the importance of understanding how diatom community composition responds to upwelling events. This study examines the diatom community composition using high-throughput amplicon sequencing from two transects that followed upwelling plumes from

different locations along the coast of California (Fig. 1). The southern transect followed an upwelling plume that started just north of San Francisco Bay in a region of the shelf with higher initial iron concentrations as it moved off the shelf and crossed the California Current frontal zone (Fig. 1). The northern transect followed an upwelling plume that started over the shelfbreak in a region with lower initial iron concentrations and ended in the California Current (Fig. 1). Diatom community composition from both transects are examined in the context of physicochemical variability and the results suggest that factors that influence iron concentration in upwelled waters (shelf width and nearby riverine input) affect the type of diatoms that respond to upwelling events. These analyses aim to constrain the relationship between diatom response and upwelling in an effort to more effectively predict phytoplankton species abundance, distribution, and subsequent locations of enhanced carbon export in the CCS.

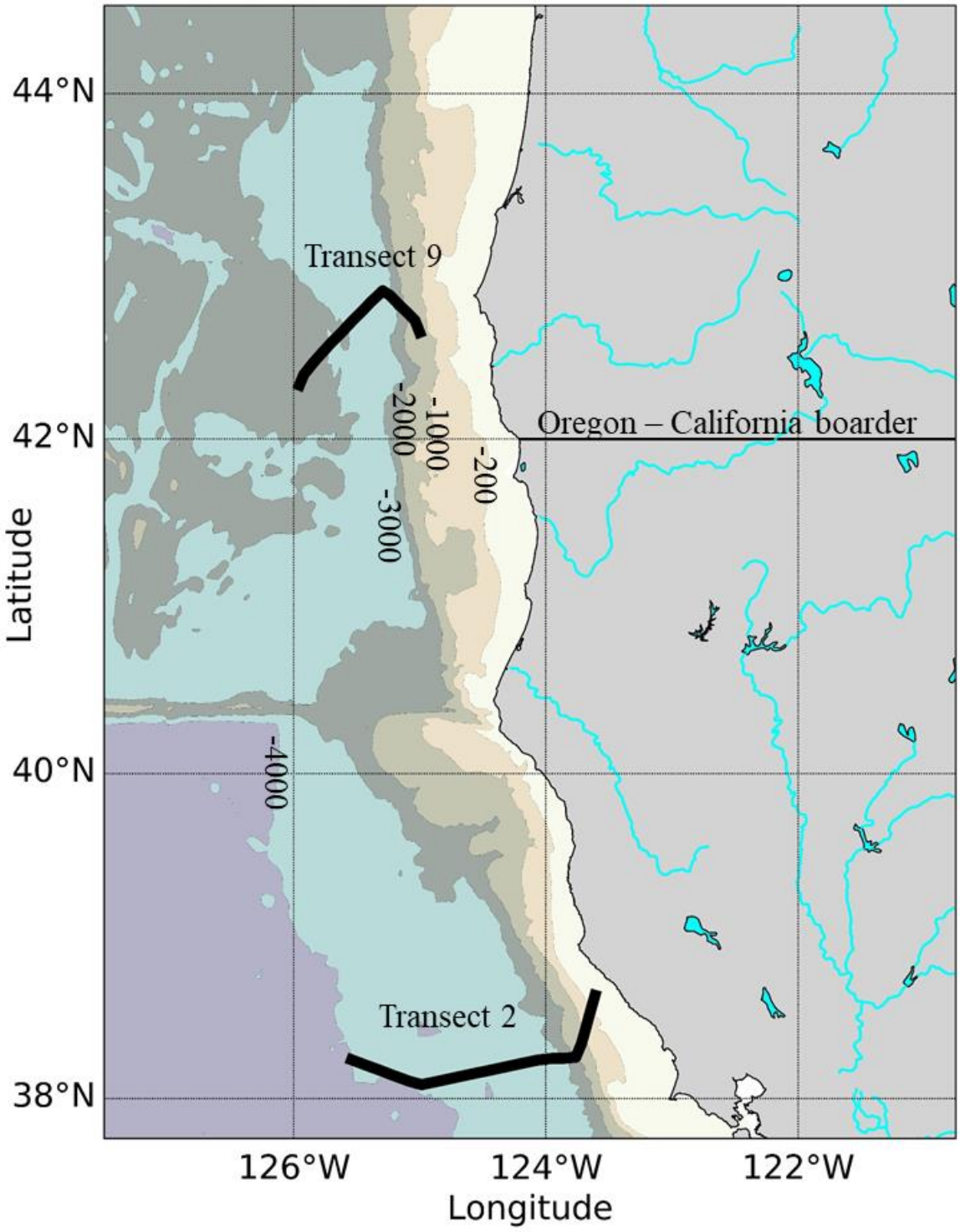

Fig. 1. Sampling area along Oregon and California coast, with ocean bathymetry showing shelf location and width in relation to transects 2 and 9. Aqua colored rivers show location of river input to the ocean. Bathymetry was generated from ETOPO1 (Amante and Eakins, 2009).

METHODS

Sample collection

Surface water samples were collected from the CCS across two transects that followed upwelling plumes from the coast offshore during the July 2014 IRN-BRU cruise on the R/V Melville (MV 1405). The southern transect (hereafter referred to as transect 2) followed upwelling waters close to a broad continental shelf with high riverine sources (higher iron) and the northern transect (hereafter referred to as transect 9) followed upwelling waters over the narrower shelf break in a drier region (lower iron) (Figs. 2 and 3). Samples were collected approximately every 30 minutes along each transect using a trace metal clean surface tow-fish system (Bruland *et al.*, 2005) into 10% HCl acid cleaned cubitainers® (Hedwin). At each sampling timepoint 1-1.5L of water was filtered onto Sterlitech 25mm diameter 1.2 µm PES (Polyethersulfone) Membrane filters, placed in RLT buffer (Qiagen), frozen in liquid nitrogen and then stored at -80 °C until extraction. Water samples for both surface macronutrient analyses, and surface dissolved iron analyses were collected concurrently and filtered through an acid-cleaned, seawater-flushed 0.2 µm Acropak filter capsule (Pall 500, Fisher Scientific). Nitrate + nitrite, phosphate, and silicate were analyzed onboard following standard spectrophotometric methods (Till *et al.*, 2019) using a Lachat QuickChem 8000 Flow Injection Analysis System. Surface dissolved iron was analyzed onboard as described in Till *et al.* (2019), where dissolved iron concentrations for transect 9 have been previously published.

Environmental data

Sea surface temperature (SST) and salinity were measured using an SBE 21 Thermosalinograph (SeaBird Electronics) and fluorescence using a Turner 10AU fluorometer

from waters collected via the flowthrough intake as part of the meteorological system on the ship. Daily CMEMS (E.U. Copernicus Marine Environment Monitoring Service) GLORYS12V1 global reanalysis for the CCS region was obtained for the entire month of July 2014. Resolution was 0.083° x 0.083° variables included SST, salinity, sea surface height (SSH), and sea water velocity (U-V) and are plotted in Figs. 2 and 3 for the calendar day that transect was sampled. Gridded U-V values were linearly interpolated, and back tracing of the surface water mass was estimated every 4 hours by moving backwards based on the current velocity interpolated to that point location. Distance traveled and direction were then calculated from U-V to move the point to the estimated location where the water mass was located 4 hours earlier. This was done for 92 hours or 4 days, to estimate origination of the surface water. While this allowed for estimating water mass origination, the resolution was ~9km x 9km thus the error associated with the back tracing could be an area of 81 km^2. Regardless of this potential error, the tracing indicated by the bold lines in Figs. 2 and 3 can serve as general indicators of where the surface water mass is likely coming from.

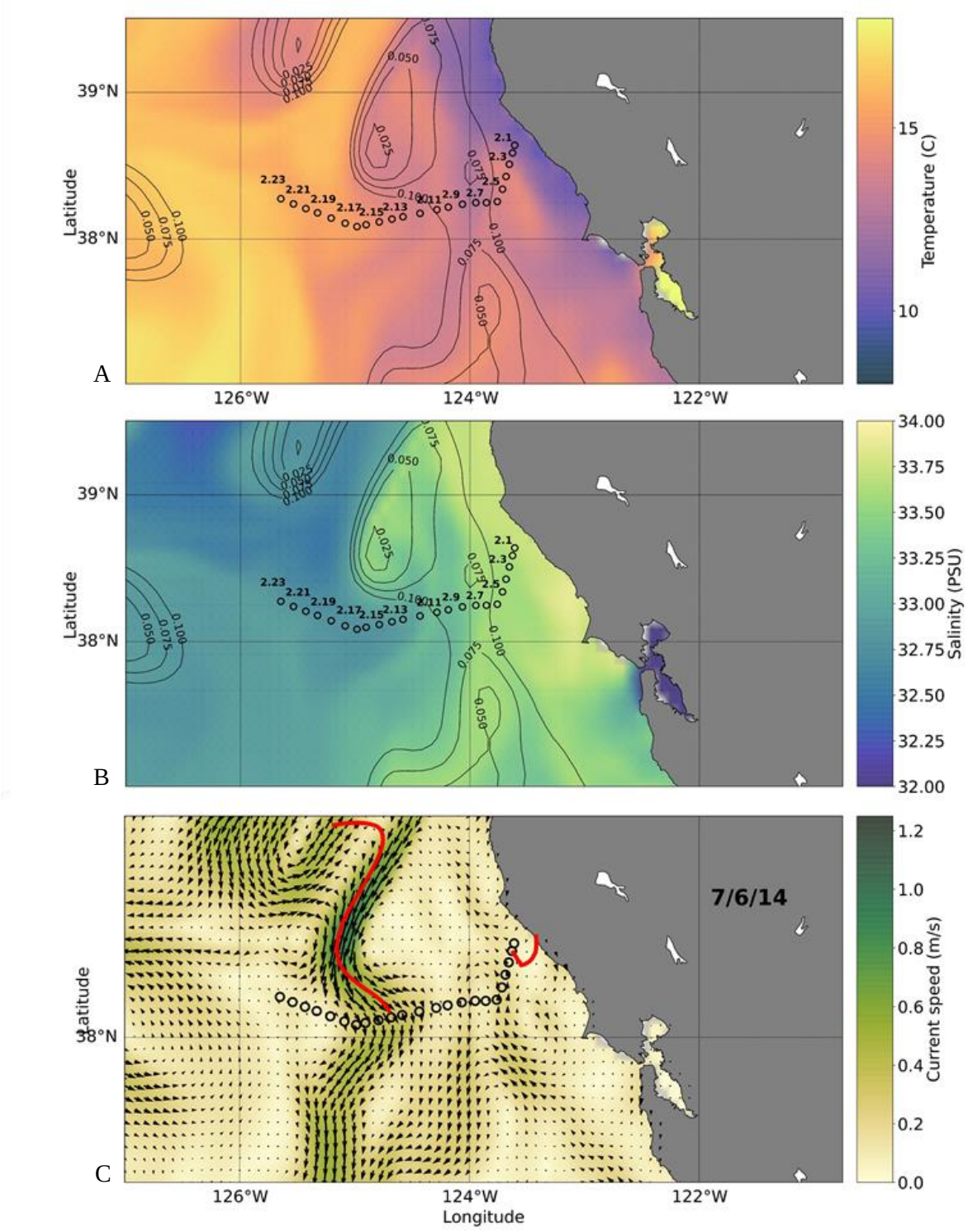

Fig. 2. Transect 2 sampling locations with every other sample labeled are plotted over a background of satellite parameters from CMEMS GLORYS12V1 global reanalysis data for July 6th, 2014.

Fig. 2. Continued. (A) SST (color bar) overlain with SSH in 2.5 cm increments (contours). (B) Sea surface salinity (colorbar) overlain with SSH in 2.5 cm increments (contours). (C) Direction (black arrows) and speed (colorbar) of surface ocean geostrophic currents. Red lines indicate 96-hour back tracing of surface water for stations 2 and 14. Animation of 96 hours of surface ocean geostrophic currents can be found here 10.6084/m9.figshare.16990387.

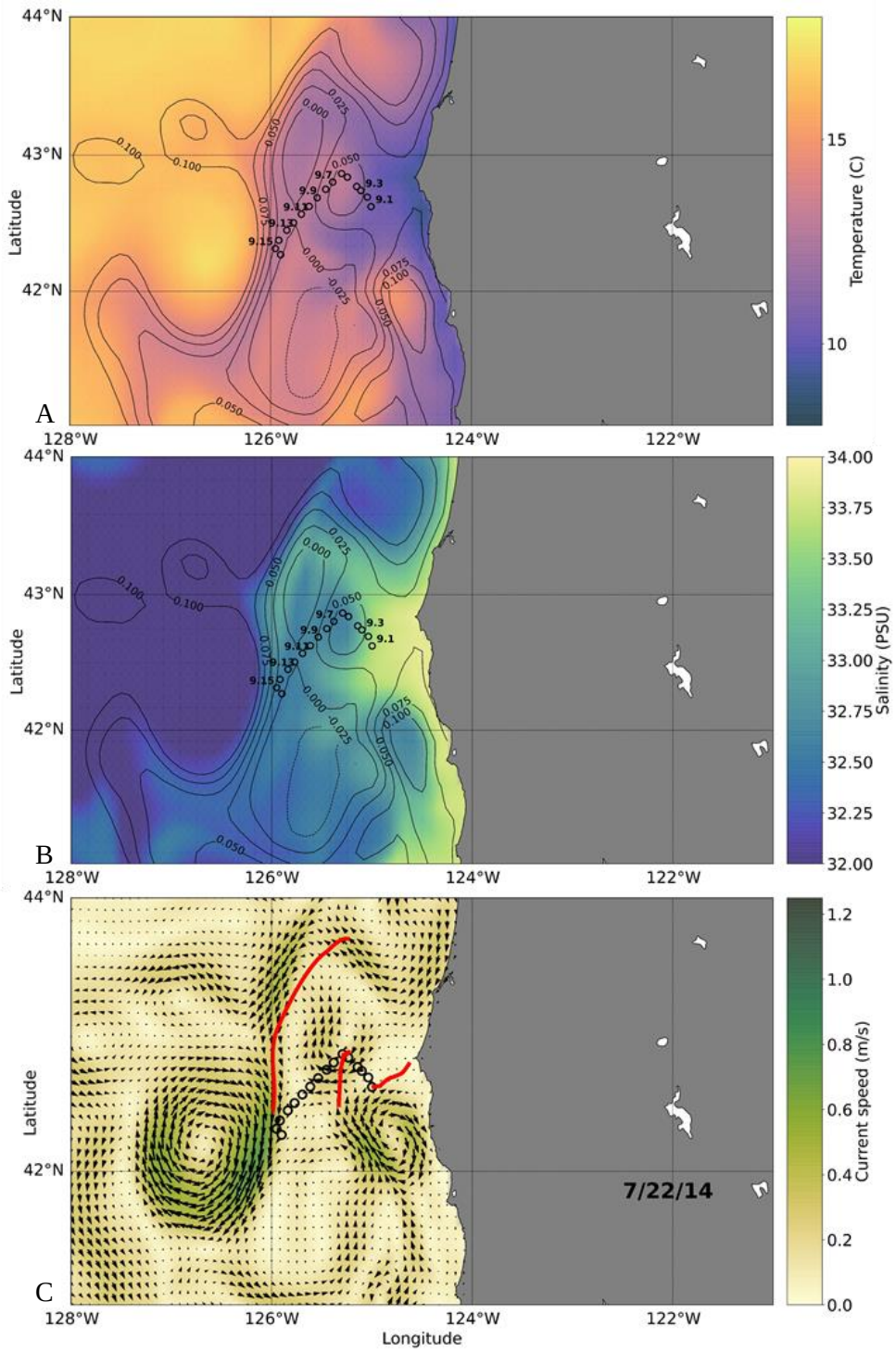

Fig. 3. Transect 9 sampling locations with every other sample labeled are plotted over a background of satellite parameters from CMEMS GLORYS12V1 global reanalysis data for July 21st, 2014.

Fig. 3. Continued. (A) SST (color bar) overlain with SSH in 2.5 cm increments (contours). (B) Sea surface salinity (colorbar) overlain with SSH in 2.5 cm increments (contours). (C) Direction (black arrows) and speed (colorbar) of surface ocean geostrophic currents. Red lines indicate 96-hour back tracing of surface water for stations 1, 6 and 15. Animation of 96 hours of surface ocean geostrophic currents can be found here 10.6084/m9.figshare.16991749.

DNA extraction, amplification and sequencing

DNA/RNA were co-extracted using the Allprep RNA/DNA Mini Kit (Qiagen). The extracted DNA was amplified in triplicate using primers from Zimmermann *et al.* (2011), which isolates the v4 region of the 18S marker gene to analyze for total diatom community composition (Zimmermann *et al.*, 2011) as modified for Illumina sequencing (Chappell *et al.*, 2019). The amplified DNA products were pooled and purified by Mag-Bead purification using AMPure XP (Beckman Coulter). The amplified DNA was then subject to another round of PCR, to attach MiSeq indices (Illumina), and Mag-Bead purified again. Sequencing was done using the Illumina MiSeq Desktop Sequencer at Old Dominion University (Norfolk, Virginia, USA) using a 2×300-bp kit.

Sequencing analysis

The DNA sequences were analyzed by pipeline analysis using DADA2 (Callahan *et al.*, 2016) with modifications described in (Oliver *et al.*, 2021). ASV's were identified using BLASTn (Altschul *et al.*, 1990) algorithm to an in-house database including eukaryotic sequences from SILVA (the German Network for Bioinformatics Infrastructure) and 18S stramenopile sequences from the National Center for Biotechnology and Information (NCBI). Identified ASV's were classified to the species level if they had a >99% identity hit to a diatom sequence, to species-like if 97-99% (akin to the cf. designation in morphology), and to genus level if below 97%. ASV's were then clustered using the CD-HIT algorithm and combined into operational taxonomic units (OTU_{99}) if they had less than 1% percent identity difference between them. The untransformed OTU_{99} sequencing data was used to calculate Shannon diversity, Margalef species richness, and Pielou's evenness.

Primer 7 (Primer-e) was used for multivariate analysis on the 18S diatom community. Each transect was imported, square root transformed, and a dendrogram was generated using Bray-Curtis as the resemblance measure (Bray and Curtis, 1957). A SIMPROF test was conducted with 1000 permutations to determine if branches of the dendrogram could not be distinguished. Environmental variables (sea surface salinity and SST, fluorescence, nitrate, silicate, phosphate and dissolved iron) were normalized and Euclidean distance was used as the resemblance measure for BEST analysis with the Bio-env algorithm (Clarke and Ainsworth, 1993). Spearman rank correlation between changes in environmental variables and community shifts were calculated and to determine significance of the correlation, 1000 permutations of the correlation test were conducted.

Table 1. Diversity metrics of diatom community composition and dFe measurements for CCS stations.

Station	N	Richness	Evenness	Diversity	dFe (nmol/kg)
T2S1	71626	8.408463	0.485657	2.211623	1.08
T2S2	70895	12.80335	0.433522	2.154524	1.04
T2S3	95179	9.333961	0.361709	1.693568	1.13
T2S4	119394	9.837313	0.53213	2.529528	1
T2S5	97583	16.10312	0.478104	2.498452	0.58
T2S6	30501	12.00909	0.642138	3.100444	0.44
T2S7	32678	5.868512	0.497862	2.054742	0.27
T2S8	46959	7.251072	0.484483	2.116923	0.47
T2S9	51445	8.296255	0.464535	2.09545	0.45
T2S10	49101	11.6649	0.551026	2.669275	0.38
T2S11	59934	9.999092	0.495922	2.335557	0.5
T2S12	19915	6.263114	0.596207	2.470168	0.48
T2S13	28442	5.265405	0.577555	2.314456	0.26
T2S14	21206	9.5362	0.591738	2.7009	0.15
T2S15	19530	8.502276	0.608724	2.704349	0.13
T2S16	13601	3.782348	0.622146	2.246519	0.36
T2S17	73818	8.653484	0.256292	1.175091	0.21
T2S18	131243	9.079488	0.395547	1.852005	0.29
T2S19	98280	9.481909	0.480309	2.257681	0.24
T2S20	97822	9.398738	0.404964	1.899825	0.21
T2S21	82595	8.567615	0.319218	1.463606	0.46
T2S22	84798	11.19137	0.65974	3.201078	0.13
T2S23	109451	17.40894	0.482535	2.563806	0.15
T9S1	69351	8.3431	0.575665	2.615415	NaN
T9S2	60314	5.450918	0.457069	1.878953	0.36
T9S3	66950	5.579704	0.461242	1.910989	0.36
T9S4	75205	10.77666	0.48053	2.308474	0.4
T9S5	63038	11.94409	0.644731	3.152959	0.34
T9S6	48231	11.03511	0.659051	3.1552	0.27
T9S7	49335	9.531398	0.530165	2.462296	0.29
T9S8	28162	7.320123	0.585625	2.536188	0.31
T9S9	32210	10.30825	0.685997	3.21193	0.31
T9S10	95978	12.3781	0.557186	2.765229	0.26
T9S11	77705	10.56775	0.617831	2.957862	0.36
T9S12	67435	14.56976	0.540509	2.753218	0.3
T9S13	80614	11.94962	0.485443	2.384816	0.31
T9S14	65256	11.99703	0.63334	3.101996	0.31
T9S15	54337	11.00618	0.64287	3.08307	0.26
T9S16	76631	8.802537	0.349226	1.608245	0.24

RESULTS AND DISCUSSION

Physical dynamics

Transect 2 sampled an upwelling plume just north of San Francisco Bay following the plume as it moved offshore and joined the California Current (Fig. 2). 96-hour back tracing of surface currents shows the surface waters from samples 1-3 originating from the coast where upwelling was and is occurring as evidenced by colder sea surface temperatures and higher salinity (Fig. 2C). Similar analysis shows that the surface waters from sample 14 originated upstream in the California Current. Examining the transect in temperature-salinity (T-S) space (Fig. 4A) shows that the transect transitioned from low temperature/high salinity waters to higher temperature/lower salinity waters with no obvious outliers. Based on T-S properties, it appears that there is a frontal zone corresponding to where samples 12-15 were collected as there are large temperature/salinity changes between these sampling locations spanning ~30 km (Fig. 4). This frontal zone is also associated with high surface current velocities (Fig. 2C), which suggests it is likely the California Current. Examining surface nitrate concentrations, temperature, and salinity along the transect (Fig. 4A) shows cold, saline and high nitrate water in the recent upwelling near the coast with increasing temperature and decreasing nitrate and salinity as the transect approaches and crosses the frontal zone. Additionally, nitrate:silicic acid ratios drop below one in the frontal zone (Fig. 4B) which is indicative of potential for silicic acid limitation of diatoms (Brzezinski *et al.*, 2003). In addition to high macronutrient concentrations (nitrate, phosphate, silicic acid), the beginning of transect 2 also had elevated dissolved iron concentrations (Table 1).

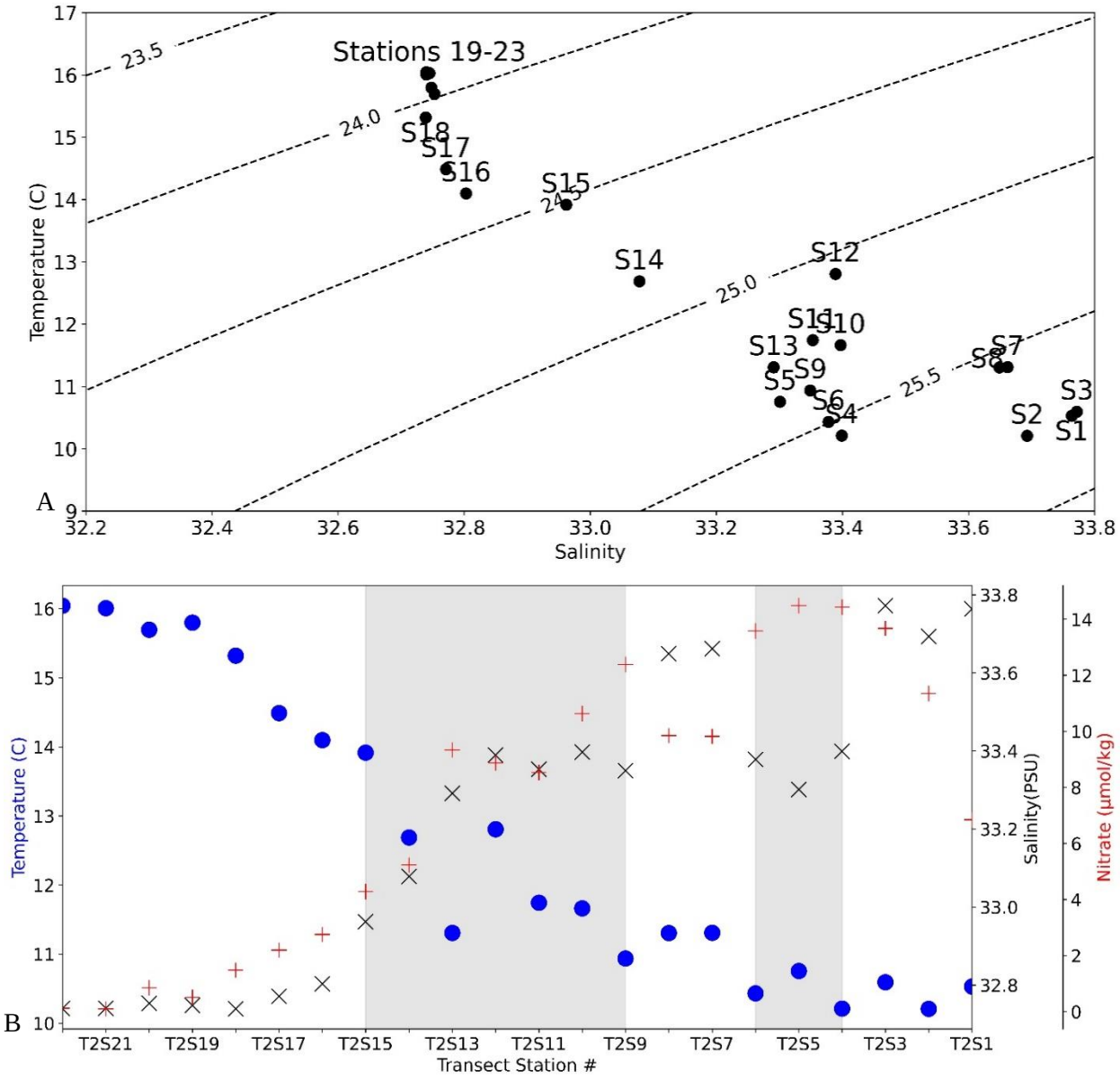

Fig. 4. Physiochemical properties along transect 2. (A) Temperature – Salinity plot with density (σ_t) contours of transect 2. (B) SST, salinity, and nitrate are plotted along transect 2. The gray shading indicates a nitrate:silicic acid ratio below 1, which is considered to be a sign of potential for silicic acid limitation. Blue circles = Temperature, Red plus = Nitrate, Black X = Salinity.

Transect 9 sampled more complex physical dynamics than transect 2 thus it was not as clear that sampling followed the upwelling plume as it ages. As in transect 2, transect 9 originated in colder more saline water indicative of upwelling at the coast along Cape Blanco (Fig. 3). As the transect moves offshore it follows the upwelling plume but also traverses an anticyclonic eddy indicated by elevated positive SSH and clockwise current direction around the center at samples 4-8 (Fig. 3C), and as a result, samples 5-7 appear as outliers from the transition from high salinity/low temperature waters to low salinity/high temperature waters of the other transect samples (Fig. 5A). The animation of sea surface currents (URL in Fig. 2 and 3 caption) shows a clearer picture of where the northerly moving eddy is coming from and which samples it influences. An examination of 96-hr surface current back tracing reveals that sample 1 originated from the coast to the east, sample 5 originated from the eddy that is moving north, and samples 15/16 originated from the coast to the northeast. These results suggest that the samples furthest offshore (~12-16) may have originated from a different upwelling plume north of Cape Blanco along the coast and over a wider shelf (Figs. 1 and 3). In terms of hydrography and macronutrient concentrations, transect 9 samples showed similar dynamics compared to what was observed in transect 2, where cold water with high salinity and high nitrate concentrations is seen in recent upwelling close to the coast (Fig. 5B). Moving offshore in transect 9, higher temperatures, low salinity and low nitrate concentrations are measured in samples from the anticyclone eddy, which is consistent with deepening of the pycnocline often observed in an anticyclonic eddy in the Northern Hemisphere (Dufois *et al.*, 2016). Based on nitrate:silicic acid, it also appears that there is the potential for diatom silicic acid limitation approaching and crossing the front into the California Current (Fig. 5B). Contrary to what was observed in transect 2, while macronutrient concentrations (nitrate, phosphate, silicate) were elevated close to

the coast, dissolved iron concentrations throughout transect 9 remained very low (<0.4 nmol/kg) throughout the transect (Table 1).

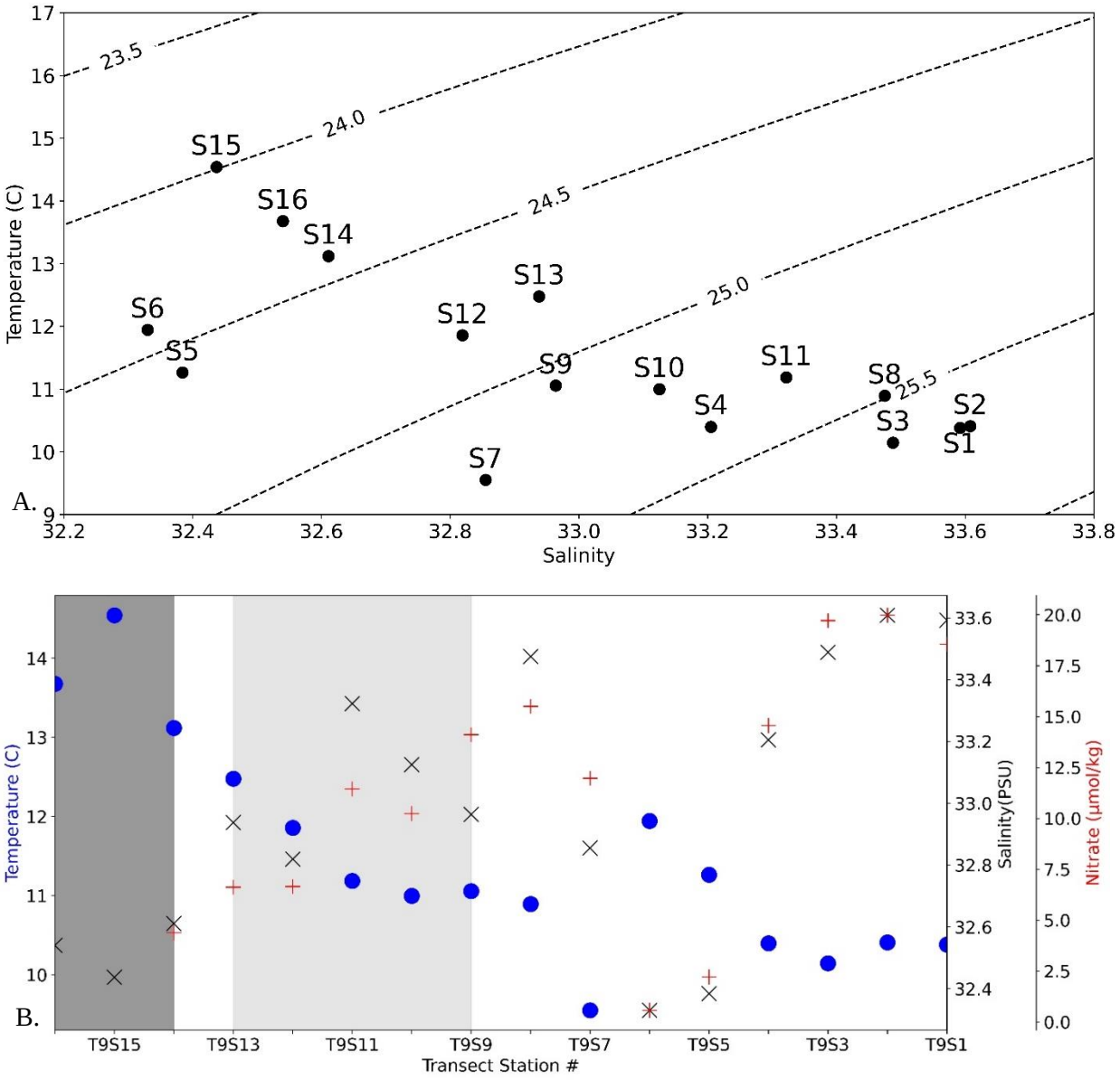

Fig. 5. Physiochemical properties along transect 9. (A) Temperature – Salinity plot with density (σ_t) contours of transect 9. (B) SST, salinity and nitrate are plotted along transect 9. The gray shading indicates a nitrate:silicic acid ratio below 1 which is considered to be a sign of potential for silicic acid limitation. Dark gray shading (samples 15 and 16) indicate no macro-nutrients were collected. Blue circles = Temperature, Red plus = Nitrate, Black X = Salinity.

Diatom community similarity analysis

Looking at the Bray-Curtis similarity of diatom community composition for transect 2, the dendrogram branches into two main groups between samples 1-13 and 14-23 (Fig. 6A), which is coincident with the location of the frontal zone described above. The BEST analysis revealed a statistically significant relationship between sea surface salinity and temperature with the Bray-Curtis resemblance matrix of transect 2 ($\rho = 0.801$, $p=0.001$), which along with the pattern seen in the nMDS plot (Fig. 6B) suggests that the diatom community shifts were primarily driven by factors associated with upwelling (high salinity, nutrients, and dissolved iron) before the frontal zone and primarily associated with elevated SST after the frontal zone and depleted nutrients.

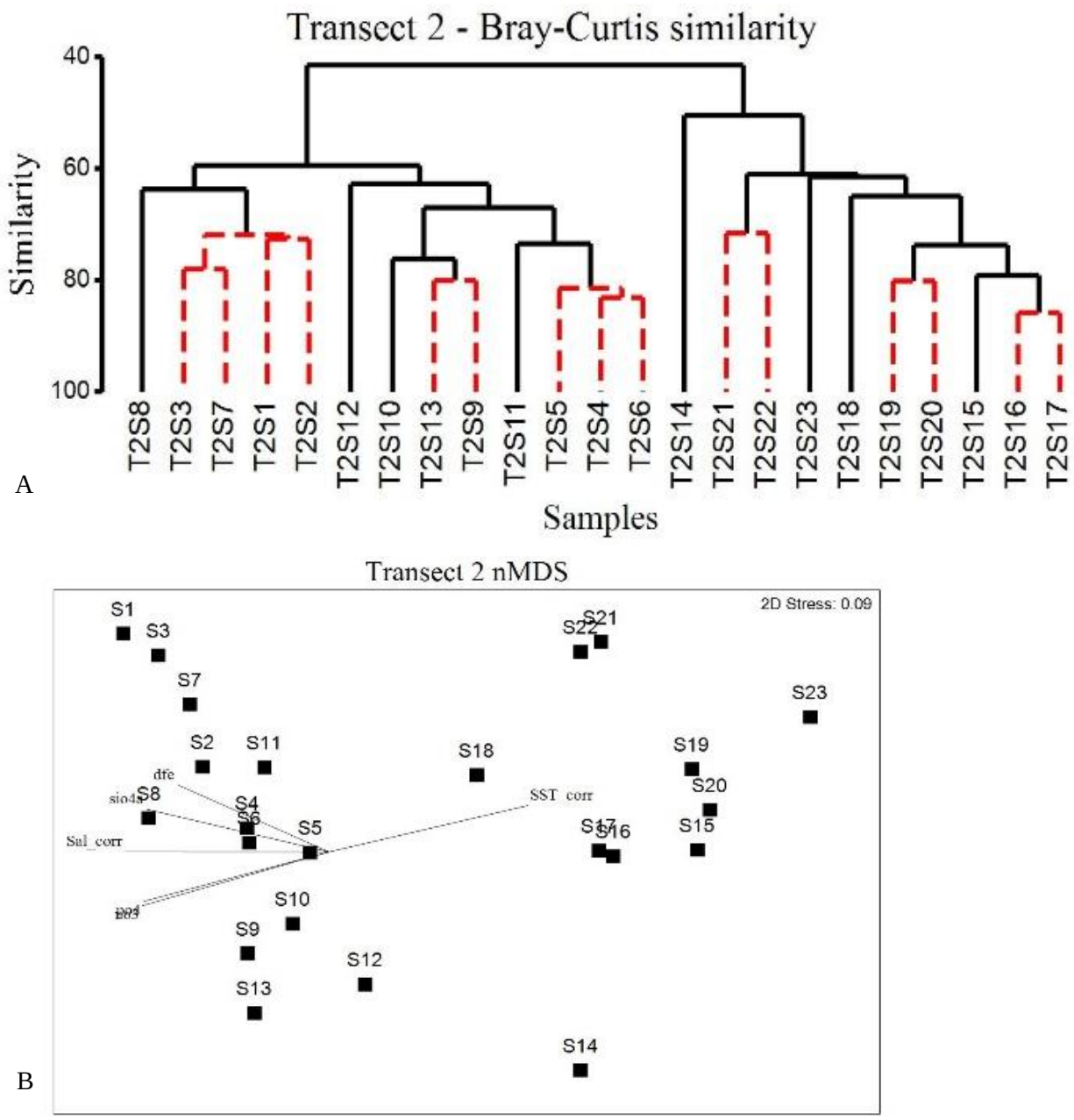

Fig. 6. Diatom community analysis of transect 2**.** (A) Diatom 18S OTU_{99} community analysis for transect 2 is plotted in a Bray-Curtis similarity dendrogram. SIMPROF test (1000 permutations) are shown with dashed red branches, where samples are not statistically different. (B) nMDS plot overlain with environmental variables driving ordination, BEST results $\rho = 0.801$ (SST and salinity), $p = 0.001$. (C) Relative abundance of the top 20 diatom 18S OTU_{99} are shown along transect 2.

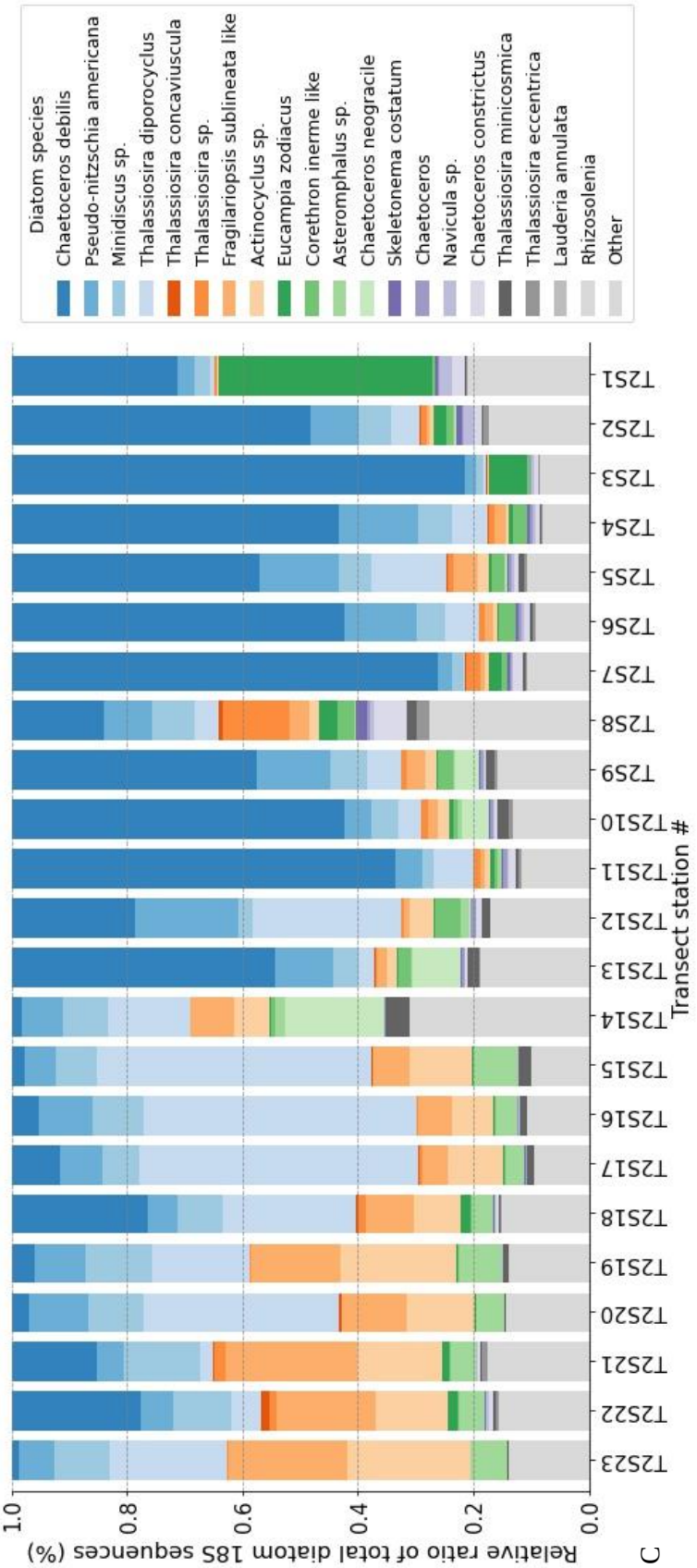

Fig. 6. Continued.

The primary and dominant diatoms in the recent upwelling of transect 2, which was elevated in both macronutrient concentrations and dissolved iron, were *Chaetoceros debilis*, and *Eucampia zodiacus* (Fig. 6C, Table S1). *E. zodiacus* is a ubiquitous diatom, initially associated with warmer waters previously found off the coast of southern California (Cupp, 1943). *E. zodiacus* is known to be efficient at nitrogen uptake in cold water and the abundance at the very beginning of transect 2 is likely due to this efficient uptake and lower grazing in cold recently upwelled water (Nishikawa *et al.*, 2009). Coinciding with high relative abundance of *E. zodiacus* in sample T2S1, low nitrate concentrations at the very beginning of transect 2 possible indicate that *E. zodiacus* is drawing down nitrate at a significant rate. *C. debilis* is a medium sized chain forming diatom that has been found to bloom off the coast of California, normally during early spring (Cupp, 1943). This species is known to favor higher iron conditions (Assmy *et al.*, 2007) while having poor growth under iron and silica limitation (Hoffmann *et al.*, 2008). Given this information about *C. debilis* and its preference for high iron and high macronutrients, it is perhaps not surprising that this species is abundant in the recent upwelling samples of transect 2 with elevated iron and macronutrient concentrations.

As the upwelling plume in transect 2 moves offshore and nutrients are consumed, *C. debilis* relative abundance decreases, dropping dramatically when the transect crosses the front at sample 14. However, even after crossing the front, *C. debilis* sequencing reads are still quantifiable as a member of the diatom community. This continued presence is likely due to its ability to survive a wide range of nutrient conditions and higher temperatures (Hyun *et al.*, 2014). At the frontal zone of transect 2, the diatom community shifts from a *Chaetoceros*-dominated community to a slightly more diverse diatom community driven by an increase in richness and decrease in evenness (Table 1), where sequences associated with the *Actinocyclus*

sp. MPA-2013 strain isolated from the Pacific Ocean, *Fragilariopsis sublineata* like, and *Thalassiosira diporocyclus* increase in relative abundance (Fig. 6C). *T. diporocyclus* is a small diatom found primarily in warm temperate waters and tend to be found in dense colonies (Hoppenrath *et al.*, 2007; Fernandes and Frassão-Santos, 2011). Its small size likely gives it an advantage to proliferate in the low nutrient concentrations and higher temperatures after the front in transect 2. *Actinocyclus sp.* is likely a large slowly growing diatom (Hoffmann *et al.*, 2008). While *Fragilariopsis sublineata* is an Antarctic pennate diatom known to be adapted to low light levels (McMinn *et al.*, 2010), it has not been previously sequenced in the CCS. The primers used to amplify the diatom 18S gene in this study cannot differentiate between *Fragilariopsis* species (Chappell *et al.*, 2019; Abdala, 2020) and since this sequence hit percentage is below 99% it is not possible to say for certain that the species is in fact *F. sublineata.* Further sequencing of *Fragilariopsis* species is required to determine the strain that is found off California.

As previously described, transect 9 sampled a more dynamic physical environment than was sampled in transect 2 and that is reflected in its Bray-Curtis similarity dendrogram of diatom community composition (Fig. 7A). Likely because of the transect passing through the anticyclonic eddy in the middle of samples 1-8, the samples collected before the front, the branching pattern differentiating between diatom communities from samples 1-8 and 9-16 are not as distinct in the dendrogram as what was observed for before and after the front in transect 2. However, there do appear to be diatom community similarities at similar locations relative to the center of the eddy based on SSH and current direction (Fig. 3). For example, samples 5 and 6, which have statistically indistinguishable diatom communities (Fig. 7A) are in the middle of the eddy, corresponding with low nutrients, high temperature and lower salinity (Fig. 5B). Samples 4 and 7, which also have statistically indistinguishable diatom communities from one

another that are the most similar to diatom communities in samples 5 and 6, are on an outer ring of the eddy, where nutrient concentrations and salinity were higher and temperature was lower than what was measured at samples 5 and 6. Samples 2 and 3 are correlated with factors related to upwelling (high salinity, macro-nutrients, and dissolved iron) seen in the nMDS plot (Fig. 7B). Interestingly, samples 1 and 8 cluster together, which may be attributed to being on the outside ring of the eddy and both samples may be influenced by higher nutrients from recent coastal upwelling. Samples 9-16 all cluster together, which coincides with the decrease in nitrate, lower salinity, and higher temperatures (Fig. 5B) indicating the frontal zone of the upwelling plume. The BEST analysis showed a significant relationship between sea surface salinity and silicate with the Bray-Curtis resemblance matrix of transect 9 ($\rho = 0.546$, $p=0.002$), indicating overall that the resemblance matrix is correlated with upwelling. Although sampling of the upwelling plume in transect 9 is complicated by an anticyclonic eddy, results from the BEST analysis indicate diatom community similarities in both transects correlate with environmental variables affected by upwelling, suggesting that the diatom community changes are likely being driven by upwelling.

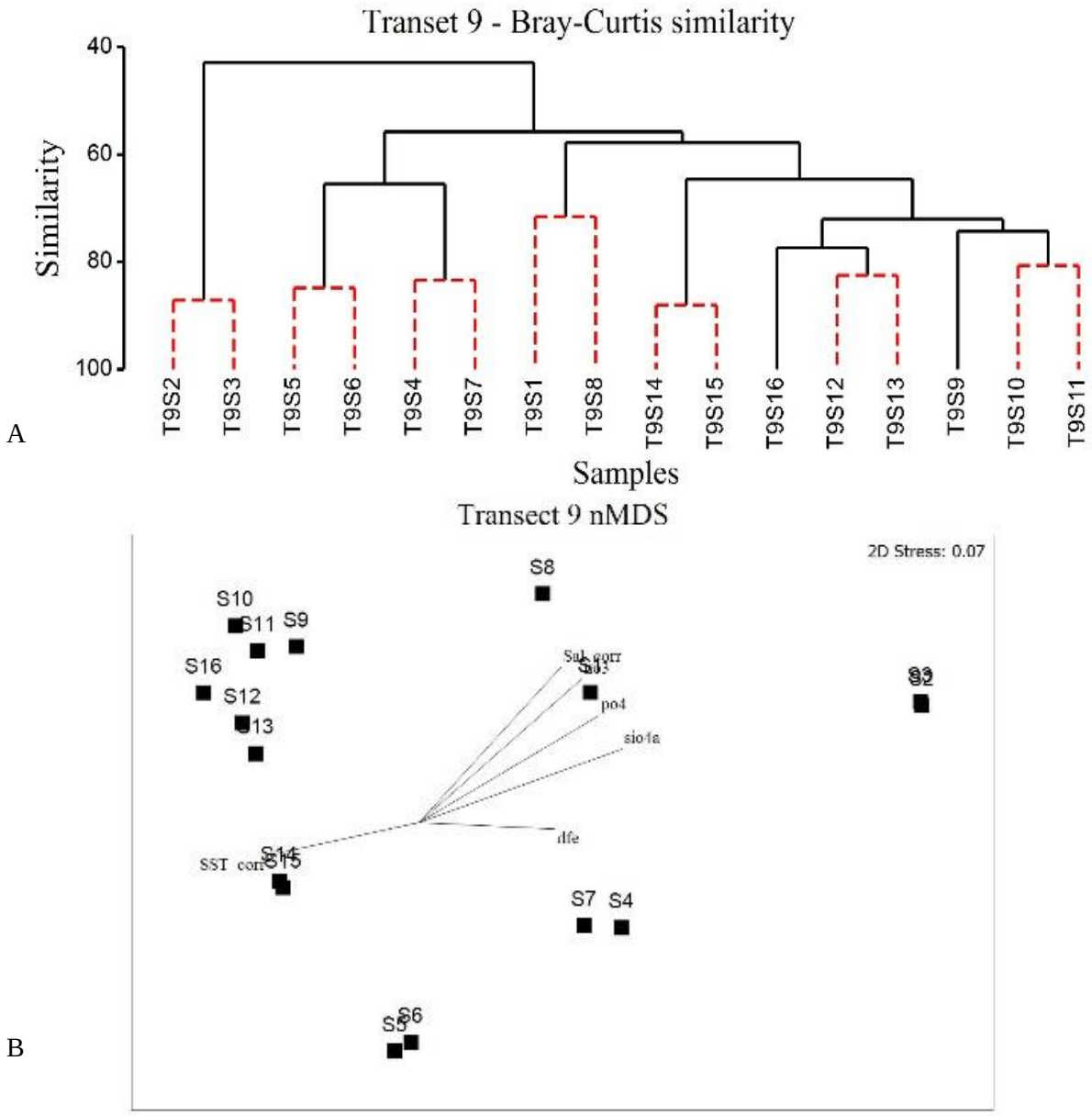

Fig. 7. Diatom community analysis of transect 9. (A) Diatom 18S OTU_{99} community analysis for transect 9 is plotted in a Bray-Curtis similarity dendrogram. SIMPROF test (1000 permutations) are shown with dashed red branches, where samples are not statistically different. (B) nMDS plot overlain with environmental variables driving ordination, BEST results $\rho = 0.546$ (Sea surface salinity and silicate), $p = 0.002$. (C) Relative abundance of the top 20 diatom 18S OTU_{99} are shown along transect 9.

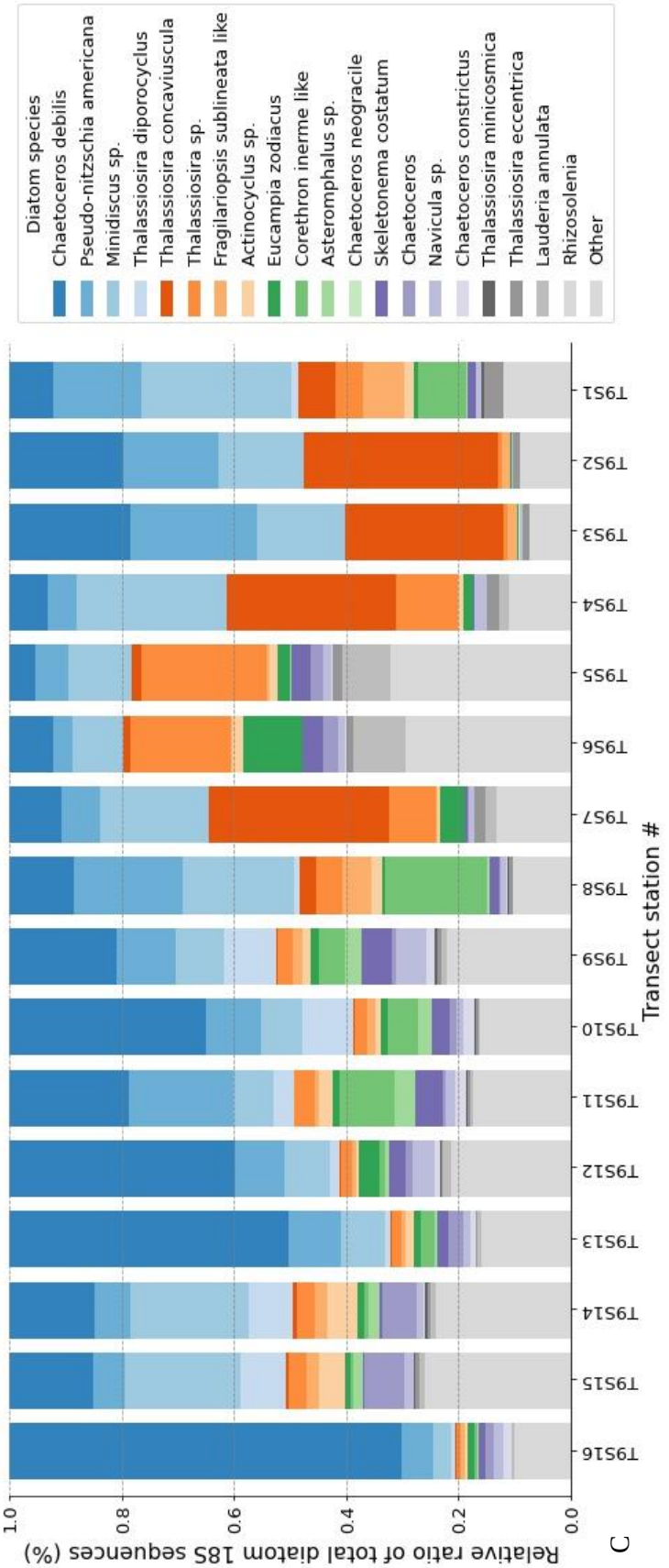

C

Fig. 7. Continued.

While *C. debilis* was also a prominent part of the diatom community in transect 9 in the later part of the transect, other diatoms are more abundant than *C. debilis* in the samples from the most recent upwelling (samples 2 and 3) based on salinity, temperature, and macronutrient concentrations (Fig. 7C, Table S1). As stated earlier, the macronutrient concentrations in the recent upwelling samples from transect 9 were higher than the recent upwelling samples from transect 2 though dissolved iron concentrations were much lower. This suggests that the lower iron concentrations in transect 9 upwelling, compared to transect 2 upwelling, may be influencing the *C. debilis* growth and limiting its dominance of the diatom community. While *C. debilis* is present in samples 2 and 3 of transect 9, it does not dominate the diatom community as *Pseudo-nitzschia americana, Minidiscus sp. strain RCC4582,* and *Thalassiosira concaviuscula* are also abundant. *P. americana* is a pennate diatom of a genus relatively resistant to low iron concentrations and can give off domoic acid (Lelong *et al.*, 2012; Lampe *et al.*, 2018). *Minidiscus* is a genus of small diatoms generally less than 5 µm diameter and considered the smallest centric diatom (Hasle and Syvertsen, 1997; Leblanc *et al.*, 2018). *T. concaviuscula* is normally only slightly larger than *Minidiscus* (Joon Sang Park, 2009). This suggests that the prominent diatoms in the lower iron upwelling of transect 9 are smaller diatoms generally more resistant to low iron concentration than the larger *C. debilis* that dominates the upwelling from transect 2.

Till *et al.* (2018), sampled the same transect and found evidence of phytoplankton iron limitation during transect 9, where iron concentrations were always low (Table 1). This evidence of phytoplankton iron limitation suggests that the low iron conditions influenced the diatom community relative to transect 2, which had higher iron concentrations, as certain diatom species are able to survive and even have a high growth rate in low iron conditions (Armbrust 2009; and

references therein). Generally, smaller diatoms can be presumed to export less carbon from the euphotic zone than larger diatoms, due to aggregate mass during export (De La Rocha and Passow, 2007). However, low iron upwelling in the CCS over a thin continental shelf has resulted in diatom blooms that are more siliceous and sink faster (Hutchins and Bruland, 1998). This change in diatom ballasting is an indicator of iron limitation, as silicic acid is preferentially taken up compared to nitrate in iron limited waters (Brzezinski *et al.*, 2015) leading to possible high sedimentation due to heavier diatoms in low iron upwelling. Although it appears that smaller diatoms are responding to the low iron upwelling in transect 9, which might be expected based on an understanding of how iron influences diatom community composition, these data cannot be used to determine if these smaller diatoms are also more silicious as a result of iron limitation, which could lead to their being a greater sink of carbon than previously thought.

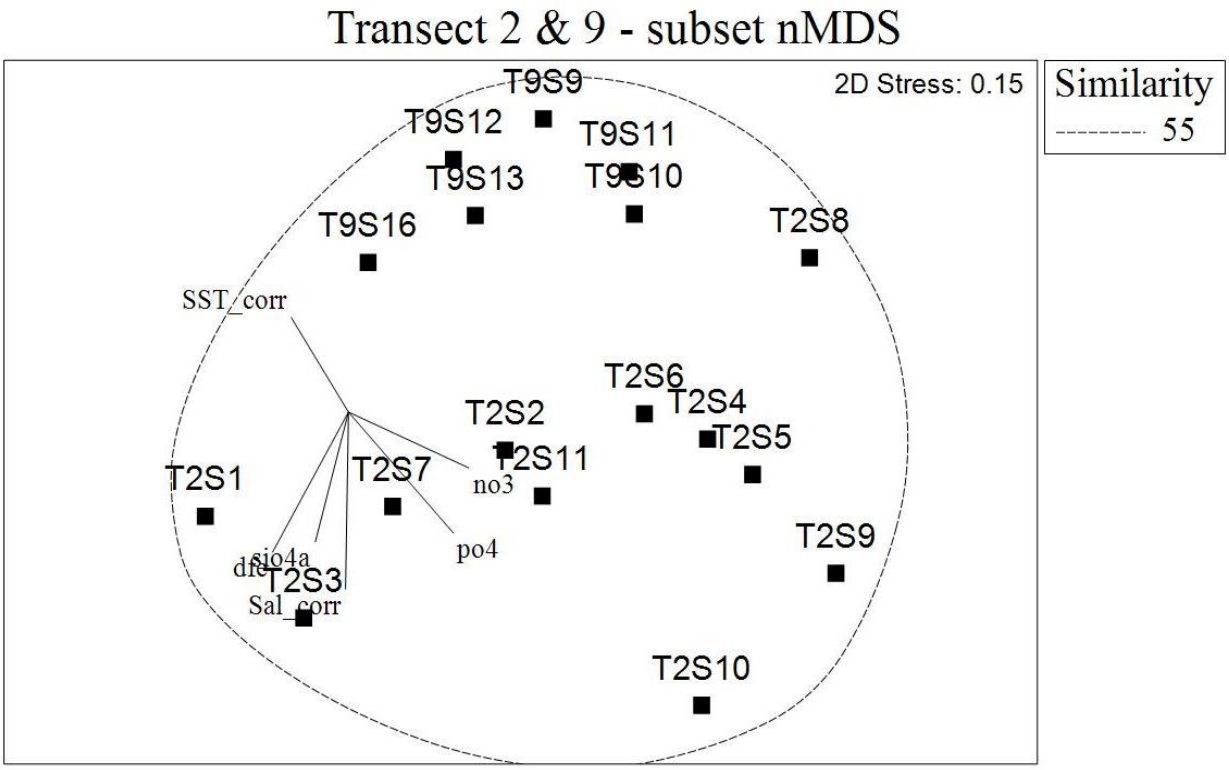

Fig. 8. nMDS plot of subset of samples within a 55% Bray-Curtis similarity between transect 2 & 9. Environmental variables driving ordination are overlain.

While the diatom communities from the recently upwelled waters of transect 9 are quite distinct from those of the recently upwelled waters of transect 2, interestingly, the diatom community after the front in transect 9 has similarities to that of the samples collected before the front in transect 2 (Fig. 8). *C. debilis* dominated the community in recent upwelling (and before the front) in transect 2 (Fig. 6C) but was found to be prominent in samples furthest away from the coast (and after the front) in transect 9 (Fig. 7C). This is peculiar as *C. debilis* is described as liking high nutrients and high levels of iron, but is abundant after the upwelling front in transect 9 where nutrients are depleted. Focusing in on the subset of similar samples between both transects in an ordination plot (Fig. 8) confirms that the diatom communities are similar even though they are spatially separated with differing nutrients concentrations. By overlaying the environmental variable correlations, it appears that the transect 2 samples from this subset correlate with variables associated with upwelling (elevated macronutrients, iron, and salinity) while the transect 9 samples correlate with elevated SST. It is curious to observe an elevated relative abundance of *C. debilis* in low nutrient, less saline, and warmer waters. However, an examination of the 96-hr back tracing of the waters from samples 15-16 in transect 9 may provide an explanation for this potential anomaly as these surface waters appear to have originated from the coast north of Cape Blanco, where it appears that upwelling is also occurring, and surface water is being transported offshore (Fig. 3C). Considering the track from Fig. 3C a higher salinity signature is indicated along the surface current moving away from shore, north of transect 9. These salinity signatures likely originated from the coast north of Cape Blanco. This back tracing analysis also reveals how quickly the surface current from the northeast was moving, as it only takes ~4-6 days for the surface water to reach outer transect 9 stations from an area likely influenced by upwelling on the coast. Although there are higher

temperatures and lower salinity at the end of transect 9, samples 12-16 likely originated in upwelling close to the coast north of Cape Blanco. Unlike the coastal region where upwelling is occurring at the start of transect nine, the Heceta Bank north of Cape Blanco has high iron inputs (Chase *et al.*, 2005) and upwelling in this region may have caused the later transect 9 samples to have high relative abundances of diatoms such as *C. debilis* similar to those found in the recent upwelling in transect 2 that was initiated with elevated dissolved iron concentrations.

By splitting each transect into before the upwelling front and after the upwelling front and relating that to the sizes of the most abundant diatoms, larger diatoms are found before the upwelling front in transect 2, shifting to smaller diatoms after the upwelling front. The diatom size fractionation is flipped in transect 9, where smaller diatoms were found before the upwelling front, likely due to lower iron concentrations in the upwelled water as explained previously, while larger diatoms were seen after the upwelling front in transect 9. As the oceans become increasingly stratified in a warming climate (Behrenfeld *et al.*, 2006) the source depth of the upwelled water mass is likely to become shallower (Durski and Allen, 2005; Capet *et al.*, 2008), which means that upwelled water that reaches the surface will likely have lower nutrient concentrations. Even if this upwelled water originates from below the euphotic zone, where macronutrients are likely more abundant, the source depth would need to originate from a depth where water is in contact with the sediment for the water mass to have higher iron concentrations. Strengthening of upwelling has still been related to temperature, nutrients, and chlorophyll-*a*, through the last 4 decades (Iles *et al.*, 2012) and it remains to be seen how quickly increased stratification will change these dynamics but even if the source depth shoals slightly, this will likely have a profound impact on the responding diatom community and associated upper trophic level productivity and carbon export. This leads me to hypothesize that in a future

more stratified ocean, diatom communities responding to upwelling will likely be smaller and thus associated with less carbon export from the surface ocean and less efficient trophic level transport, and overall leading to less productive upwelling events. However, iron limited diatoms have higher export efficiency and enhance carbon export due to enhanced silicification under iron stress (Brzezinski *et al.*, 2015). It merits further study to compare export between iron limited and iron replete diatoms to determine if heavily silicified diatoms export more carbon, or just more silica. Nevertheless, smaller, heavily silicified diatoms are likely to decrease trophic level transport and production. CO_2 outgassing is associated with upwelled waters adding to carbon dioxide concentrations in the atmosphere (Torres *et al.*, 2011) and if a more stratified ocean is associated with lower carbon export as well, the net CO_2 concentrations associated with upwelling will likely be enhanced into the atmosphere. Further increasing atmospheric CO_2 concentrations and enhancing global warming. Diatoms are known to have viable resting stages that survive decades in sediments (Ribeiro *et al.*, 2011). So, although the diatom community may shift to smaller species in this upwelling rich region, it would not be surprising to see larger species of diatoms respond should upwelling favorable winds once again upwell waters in contact with the sediment to the surface even decades into a warmer stratified ocean.

The different diatom community responses to upwelling observed in this study highlight the variability of the system and has implications for understanding of subsequent carbon export from the CCS system. Smaller diatoms do not sink as quickly and efficiently as larger diatoms, such as *C. debilis*. The diatoms in the recent upwelling coastal portion of transect 9, which had lower iron concentrations, were smaller species than those in the elevated recent upwelling in transect 2, suggesting that there is less carbon export below the mixed layer associated with this upwelling. However, the prevalence of *C debilis* at the end of transect 9 shows the need to

monitor strong upwelling currents that join the California Current that might be coming from upwelling in regions with higher iron. Additionally, the California Current also seemed to displace the *C. debilis* community in the latter half of transect 2, which is likely being dispersed south along the current. This seemingly wide dispersal of *C. debilis* indicates that the California Current has the potential to expand the region of high carbon export from high iron upwelling events, even if these areas have depleted nutrients. Global warming and increased stratification is thought to lead to upwelling with lower nutrient concentrations, and thus less primary productivity (Behrenfeld *et al.*, 2006) while one study indicates CCS upwelling may actually become even more productive with increased future upwelling (Rykaczewski and Dunne, 2010). Even if CCS upwelling becomes more productive, the dissolved iron concentrations will likely be lower, resulting in smaller phytoplankton being abundant in this enhanced primary production and thus lower carbon export. While the future of CCS upwelling may be uncertain in a changing climate, additional insight into how diatom species respond to both low and high iron upwelling will enable better predictions of the diatom community responses, dispersal, and likely areas of enhanced carbon export in a multitude of different future scenarios.

CHAPTER III

ALEXANDRIUM ON THE ALASKAN BEAUFORT SEA SHELF: IMPACT OF UPWELLING

INTRODUCTION

The Arctic Ocean has been warming faster than any other place on Earth, as sea ice retreats more and more each year (Manabe and Stouffer, 1980; Holland and Bitz, 2003). It is predicted the Arctic will continue to warm because of enhanced ocean current heat transport (Marshall *et al.*, 2014; Marshall *et al.*, 2015) and Arctic amplification (Kim *et al.*, 2016). The heat transport through Bering Strait has increased significantly over the past three decades (Woodgate, 2018) and is forecast to be one of the most influential imports of heat to the Arctic (van der Linden *et al.*, 2019). The inflow through Bering Strait is of particular interest to this study because it brings Pacific summer water to the Alaskan BS shelf. This warm water is advected into the Alaskan BS via the ACC which, upon exiting Barrow Canyon, forms the eastward-flowing Beaufort Shelfbreak Jet (Nikolopoulos *et al.*, 2009) (Fig. 1). Under intensified easterly winds, the shelfbreak jet reverses to the west, followed shortly thereafter by upwelling (Pickart *et al.*, 2009). This upwelling can deliver nutrient-rich Pacific-origin winter water from the basin onto the shelf (Pickart *et al.*, 2011; Lin *et al.*, 2019). Upwelling in the BS is predicted to increase in strength and occurrence as a result of a warming climate (Pickart *et al.*, 2013a).

The upwelled nutrient-rich cold water can reach the surface euphotic zone where phytoplankton and other biota have access to it, often leading to a bloom of phytoplankton and subsequently to an increase in upper trophic level biomass in the Alaskan BS (Ashjian *et al.*, 2010). Some phytoplankton respond better than others to water column turbulence and increased

nutrient concentrations. Diatoms are unicellular phytoplankton known to grow faster than other phytoplankton and can respond quickly to nutrient pulses, allowing them to bloom in upwelling environments (Biller *et al.*, 2013). By contrast, dinoflagellates are generally more suited to bloom when the upper water column is stratified, such as after upwelling events when the wind mixing ceases (Smayda and Trainer, 2010). When upwelling relaxes, the environment becomes more favorable to dinoflagellates and diatom growth often enters a lag phase (Smayda and Trainer, 2010).

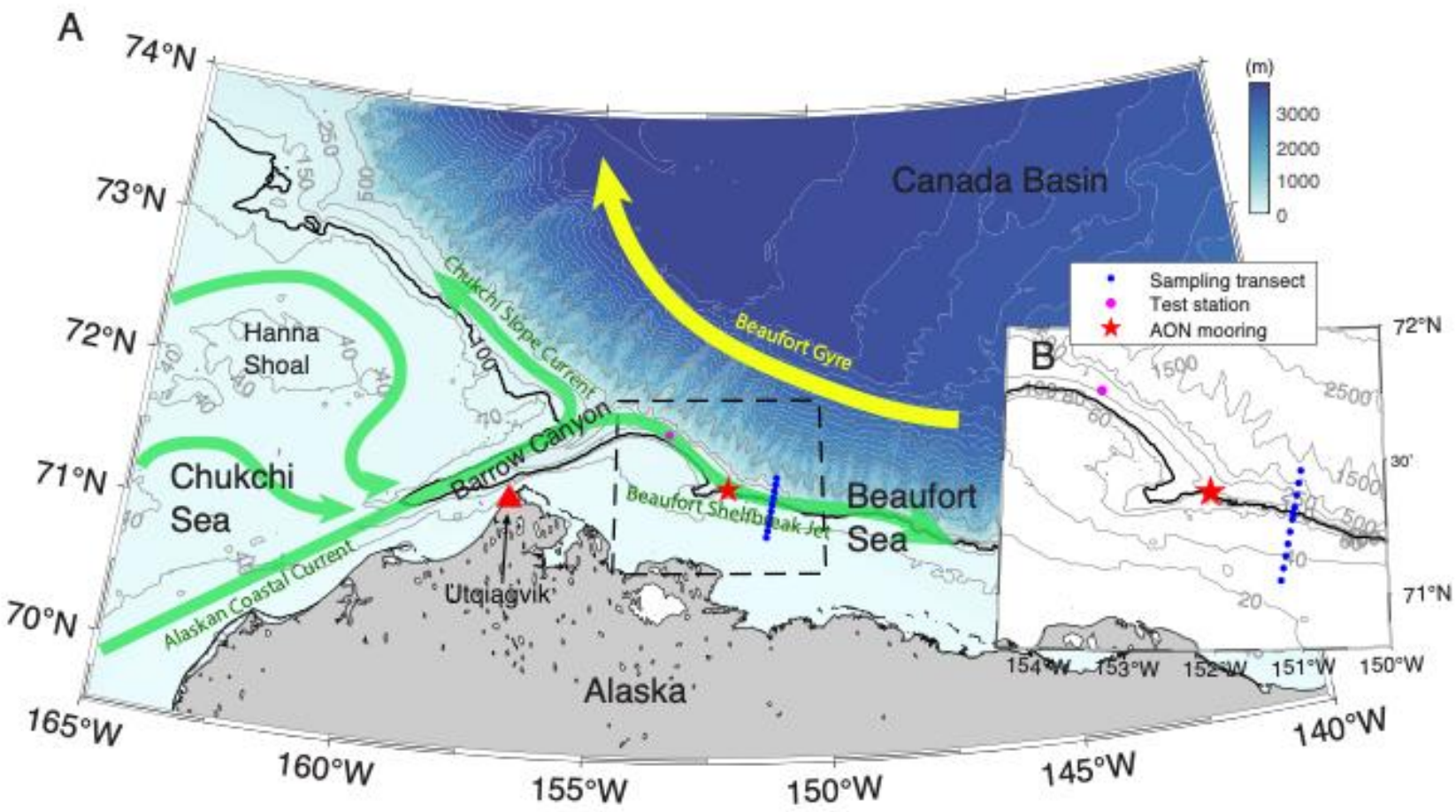

Fig. 9. Map of the study area, including place names, and schematic circulation of the region. The flow emanating from Barrow Canyon splits, with the eastward-flowing portion forming the Beaufort Shelfbreak Jet. The locations of the repeat transect, the AON mooring, and the test station are marked (see the legend). The bathymetry is from IBCAO v3. The inset shows an enlarged view of the measurement sites used in the study.

During a research cruise in late summer 2017 to the Alaskan BS shelf to study upwelling dynamics, *Alexandrium* was detected in samples run on the microscopic imaging equipment FlowCAM early in the expedition, at the onset of upwelling. Until 1970, *Alexandrium tamarense* was only found in Europe, North America, and Japan, but has been increasingly detected all over the globe – although it is characteristically found in temperate and subtropical regions (Lilly *et al.*, 2007). *A. tamarense* is a well-studied dinoflagellate known for its ability to produce saxitoxin that causes paralytic shellfish poisoning (John *et al.*, 2014). Saxitoxin can be bioaccumulated through filter feeders and fish (Wang, 2008; Cusick and Sayler, 2013), and has been documented in marine mammal beachings along the Alaskan coast up to Pt. Barrow (Lefebvre *et al.*, 2016). As the Arctic warms (Manabe and Stouffer, 1980; Holland and Bitz, 2003), there is considerable concern that *Alexandrium* may be expanding further into the Arctic.

This study combines multiple methods to evaluate *Alexandrium* abundance in the Beaufort shelf region collected at the onset, during, and after an upwelling event. The presence of *Alexandrium* is shown here further into the western Arctic domain than previously documented. While *Alexandrium* cells were imaged using a FlowCam imaging system, the species of *Alexandrium* cannot be differentiated between species by imaging alone. The species was subsequently confirmed to be *A. tamarense* using both an 18S sequencing method and a 28S real-time quantitative PCR method. As this area, and the Arctic in general, continues to warm, it may promote future toxic blooms of *A. tamarense* in the Alaskan BS.

METHODS

Physical data collection

A research cruise on R/V *Sikuliaq* took place in August-September 2017 as part of a program investigating upwelling in the western BS. During the cruise, a shelf-slope transect near 151°W was occupied four times between 30 August and 5 September (Fig. 1). An additional test station was sampled at 71.77°N 153.34°W and is included here. Conductivity-temperature-depth (CTD) stations were carried out using a Sea-Bird Electronics SBE 911-plus (Bellevue, WA, USA) with dual temperature and conductivity sensors, as well as a dissolved oxygen sensor (Sea-Bird SBE43) and a fluorometer (Wetlabs FLRTD). ~ 10 stations per transect were spaced ≤5 km apart, and each occupation of the transect took between 10 and 18 hrs to complete. The transect was located near a long-term mooring deployed as part of the Arctic Observing Network (AON) (Lin *et al.*, 2019). The mooring is situated at the 147 m isobath in the core of the Beaufort Shelfbreak Jet, roughly 35 km west of the transect (Fig. 1). Velocity was measured hourly from the mooring throughout the *Sikuliaq* cruise using an upward-facing Nortek Signature 250 kHz acoustic Doppler current profiler (ADCP) with 4 m bins, and temperature and conductivity (salinity) were measured hourly using 8 SBE MicroCATs (Sea-Bird) spaced through the water column from 33 m to near the seafloor (see Fig. 3). Wind data at 9.4 m height were obtained from the meteorological station in Utqiaġvik, AK (Fig. 1), and 10-m wind and sea-level pressure fields from the ERA5 reanalysis (Hersbach *et al.*, 2018) were used as well. We consider the alongcoast wind (105°True, positive out of west), and the alongstream velocity (125°True, positive to the east) (Nikolopoulos *et al.*, 2009; Lin *et al.*, 2019).

Sample collection

Near-surface water and water from the chlorophyll *a* max depth were collected using Niskin bottles on the CTD rosette. Up to 4L of seawater were drawn into 10% HCl acid cleaned Nalgene bottles (ThermoFisher Scientific; Waltham, MA, USA), then subsequently filtered through a 0.22 µm Sterivex (Millipore Sigma, Merck KGaA; Darmstadt, Germany) filter using a peristaltic pump. Filters were immediately frozen at -80°C until DNA extraction. Seawater was also pre-filtered through a 100 µm Nitex mesh, and 5mL of filtered seawater was run at 40x (300 µm) and 100x (100 µm) magnification (Fig. S2) on the FlowCAM (Yokogawa Fluid Imaging Technologies; Scarborough, ME, USA). Nitrate profiles were collected at 7 to 10 stations per transect occupation with an optical nitrate sensor (SUNA V2, Sea-Bird) powered with an external 51 Ah battery pack. To create depth profiles, we aligned the SUNA and CTD data by recorded time. Water samples from 4-6 depths at 12 stations selected from the broader cruise sampling efforts, which also included additional transects along the Beaufort shelfbreak not presented here, were taken for direct nitrate concentration measurements to calibrate the nitrate sensor. Nitrate concentrations in water samples were measured using an Alpkem RFA continuous flow analyzer following standard colorimetric protocols (Gordon, 1993). SUNA nitrate profiles were calibrated by fitting a linear regression to direct measurements from corresponding depths.

DNA extraction

An ethanol cleaned PVC pipe cutter was used to open the 0.22 µm Sterivex (Millipore Sigma) filters and an autoclaved scalpel used to remove the filter. Each filter was added to a 2 mL tube containing AP1 Buffer (Qiagen; Hilden, Germany) and silicon beads of 0.1- and 0.5-mm size. Bead beating was done for ~2 minutes and DNA was extracted using the DNeasy Plant

Mini Kit (Qiagen) following manufacturers protocol, with an added additional step using the QIA-Shredder column (Qiagen) for homogenization.

DNA amplification and sequencing analysis

DNA was amplified by PCR (SimliAmp, Applied Biosystems; Waltham, MA, USA) in triplicate using 1x master mix (Phusion HF Mastermix, ThermoFisher) and primers based on the 18S Illumina Earth Microbiome Project used to amplify the SSU rRNA 18S V9 marker gene to analyze for eukaryotic community composition (Stoeck *et al.*, 2010). Triplicate PCR products were pooled, and the amplified DNA was purified using Mag-Beads (AMPure XP, Beckman Coulter; Indianapolis, Indiana, USA). The amplified DNA was then subject to another round of PCR, to attach MiSeq indices (Illumina; San Diego, CA, USA), and Mag-Bead purified again. Sequencing was done using the Illumina MiSeq Desktop Sequencer at Old Dominion University (Norfolk, Virginia, USA) using a 2×300-bp kit. Sequences were analyzed by pipeline analysis using DADA2 (Callahan *et al.*, 2016) and Amplicon Sequence Variants (ASV's) were identified using the BLASTN (Altschul *et al.*, 1990) algorithm to an in-house database including 18S eukaryote sequences from the National Center for Biotechnology and Information (NCBI; Bethesda, MD, USA) and eukaryotic sequences from SILVA (the German Network for Bioinformatics Infrastructure; Bremen, Germany). To calculate the 18S *A. tamarense* relative abundance of phytoplankton, the read counts for 4 ASVs for *A. tamarense* (>99% similar) were combined and divided by the combined read counts for to all 18S phytoplankton hits (which includes ASVs classified as diatoms, dinoflagellates, and haptophytes).

qPCR assay

Quantification of the dinoflagellates *A. tamarense* and *Alexandrium catenella* was done in triplicate on a StepOne Plus real-time PCR system (ThermoFisher) using the species specific 28S qPCR assays of Hosoi-Tanabe and Sako (2005) with 1x TaqMan Fast Advanced Master Mix (ThermoFisher). Absolute 28S gene quantification was done using standard curves created by serial dilution of synthetic plasmids (GENEWIZ; South Plainfield, NJ, USA) for both *A. tamarense* and *A. catenella.*

RESULTS

The transect was occupied four times (A, B, C, D) at different stages of a wind-driven upwelling even. Context for the event is provided by the meteorological information together with the AON mooring data (Fig. 10). Earlier studies have demonstrated that the alongcoast winds are most effective at driving upwelling (Nikolopoulos *et al.*, 2009). Prior to the first occupation (A), the alongcoast winds were weakly out of the west (Fig. 10A), and the shelfbreak jet was flowing eastward (Fig. 10B). As the first section was being occupied, the winds were building out of the east and the shelfbreak jet was in the process of reversing. Typically upwelling commences roughly half a day after the shelfbreak jet reverses, but in this case the upwelling was beginning at the same time as the flow switched directions, as indicated by the uplifting of the isopycnals (Fig. 10C and D). The reason for this is that a strong upwelling event took place from 27-29 August (not shown), and the isopycnals hadn't fully relaxed prior to the upwelling event considered here. As such, we refer to the first occupation as "onset of upwelling".

The second occupation (B) took place roughly a day after the peak easterly winds, at which point the isopycnals were close to their maximum elevation but beginning to relax. The upper part of the shelfbreak jet was reversed, while the deeper part was starting to become re-established to the east, which is the typical sequence (Lin *et al.*, 2019). This crossing is referred to as "during upwelling". The third occupation (C) occurred when the bulk of the shelfbreak jet was again flowing eastward and the denser isopycnals had descended significantly deeper, which corresponds to "after upwelling". Although the final occupation (D) of the section was done during the start of another upwelling event, this event was short and weak (Fig. 10), hence this occupation is also referred to as "after upwelling".

The evolution of the large-scale wind and sea-level pressure (SLP) field is shown in Fig. S1. Before the event, the winds were northerly in the study region associated with the eastern side of the atmospheric Beaufort High (BH). During the event, the BH had weakened, but a low-pressure system over Alaska led to a strong zonal SLP gradient over the southern BS. After the event, high SLP was established over Alaska weakening the zonal gradient in the study region, resulting in light easterly winds.

FlowCAM samples taken during occupation A at the onset of upwelling imaged relatively high levels of *Alexandrium* on the BS shelf (Table S2, Fig. S2). Based on the absolute 28S gene abundances of *A. tamarense* along with the ratio of 18S *A. tamarense* sequences to total 18S eukaryotic phytoplankton sequences (diatoms, dinoflagellates, haptophytes), the threshold for being imaged by the FlowCAM was an absolute 28S gene abundance of > 3.92E+09 gc L^{-1} and a relative 18S *A. tamarense* abundance of the total phytoplankton community of > 45% (Table S2).

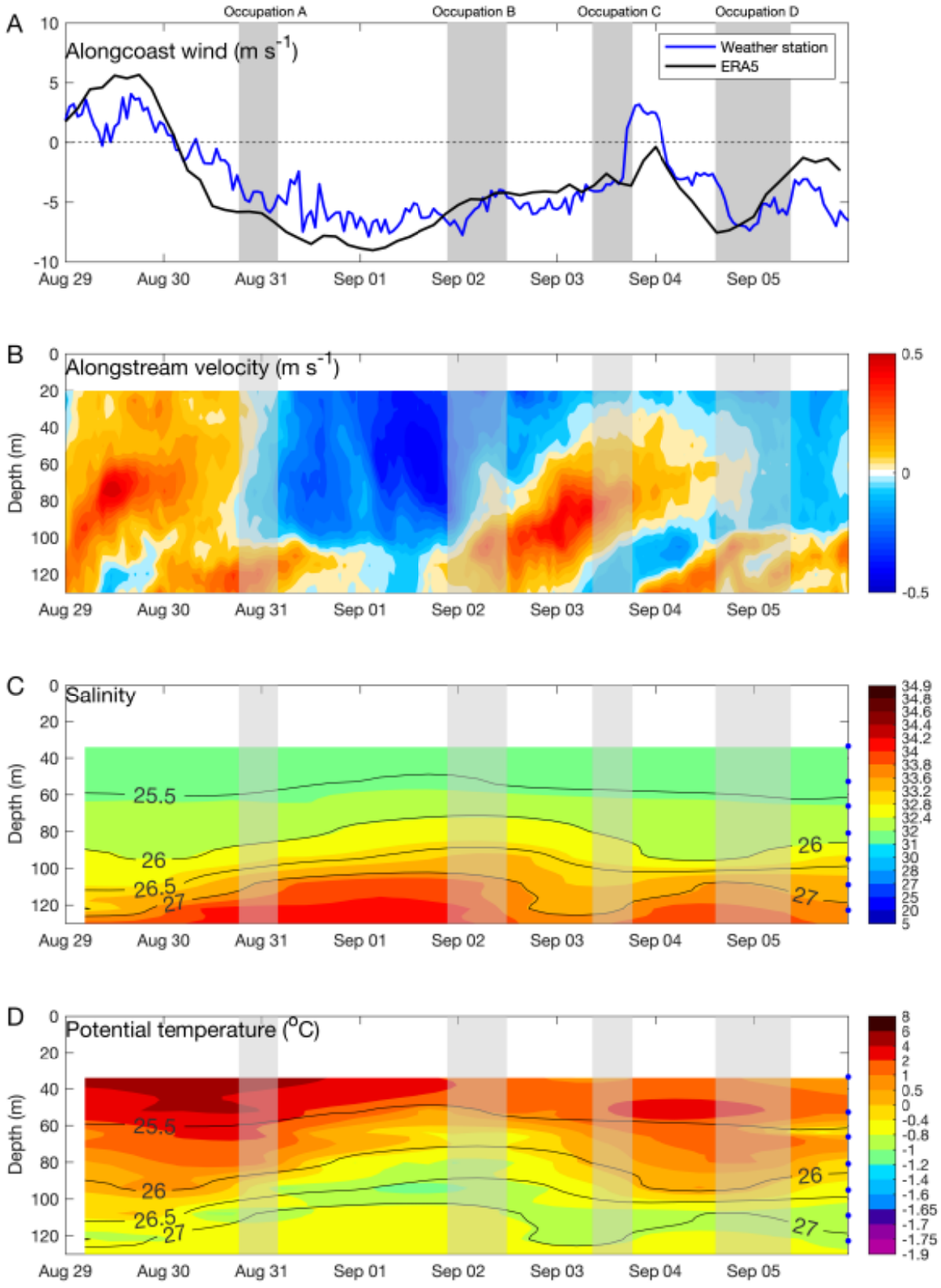

Fig. 10. Timeseries of physicochemical properties during the upwelling event.

Fig. 10. Continued. (A) The alongcoast wind speed from the Utqiaġvik weather station and the ERA5 reanalysis. Negative values correspond to winds from the east. The grey bars denote the time periods of the four ship transects occupations. (B) Alongstream velocity, where positive is to the east. (C) Salinity (color) overlain by potential density (contours, kg m^{-3}). The blue dots denote the locations of the MicroCATs on the mooring. (D) Same as (C) except for potential temperature (color).

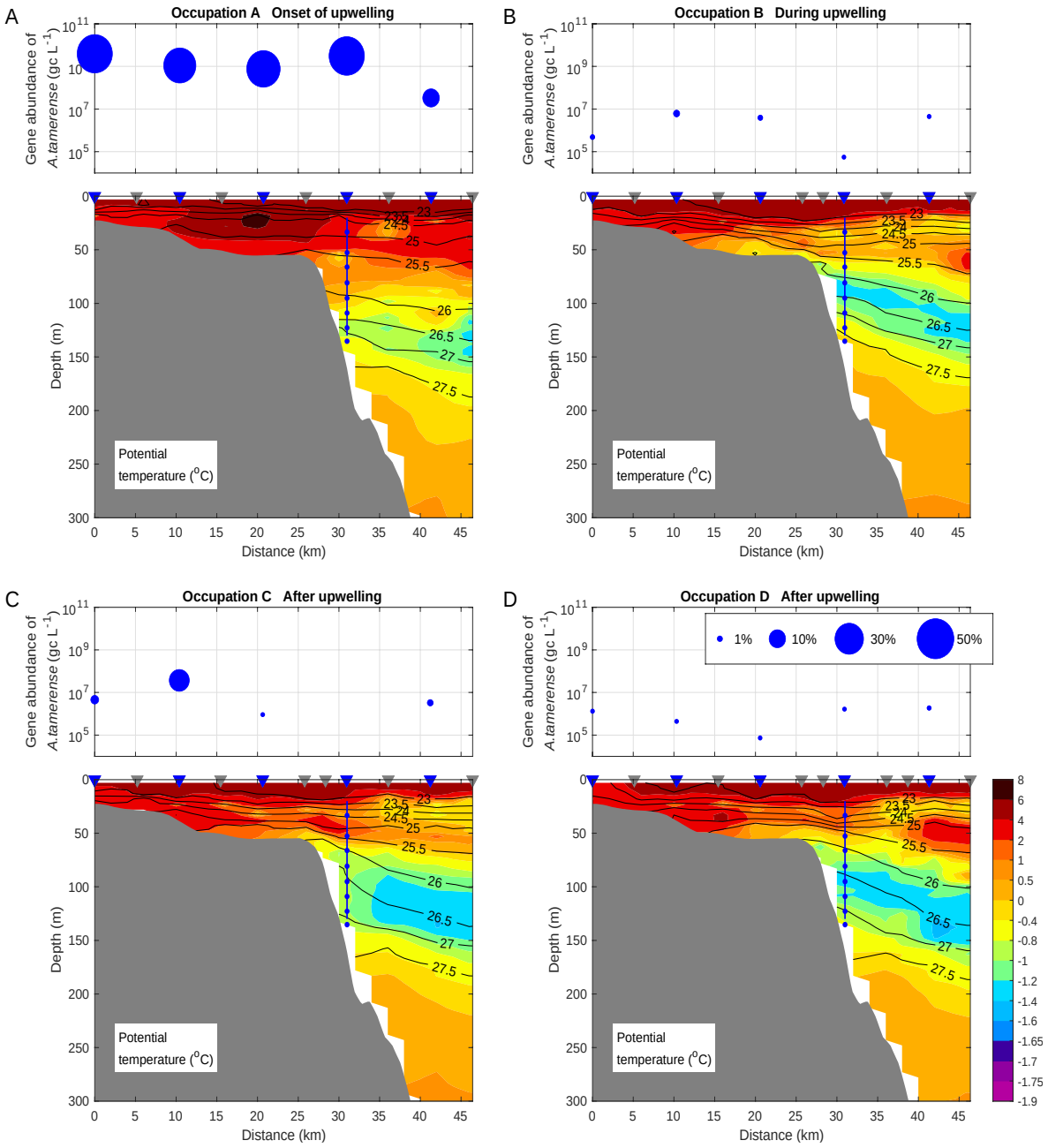

Fig. 11. Vertical sections of potential temperature (color) overlain by potential density (contours, kg m^{-3}) for (A) onset of upwelling, (B) during upwelling, and (C) and (D) after upwelling. Stations locations indicated by triangles across the top of the section with blue triangles indicating those at which surface water was collected.

Fig. 11. Continued. The corresponding concentrations of absolute 28S *A. tamarense* gene abundance from those surface collected samples are plotted above the sections, with the relative fraction of 18S *A. tamarense* of total eukaryotic phytoplankton (dinoflagellates, diatoms, haptophytes) indicated by the symbol size.

The samples on the shelf and in the vicinity of the shelfbreak during occupation A at the onset of the upwelling event had ~2 orders of magnitude higher *A. tamarense* 28S gene copies L^{-1} than samples collected during and after the event (Fig. 11). The same pattern is seen in the 18S relative gene abundance of *A. tamarense*, where it accounts for >40% of the eukaryotic phytoplankton community at the start of upwelling (Fig. 11). After the upwelling, the 18S relative abundance decreases to <1%, except for the surface sample collected at 11 km, from the onshore start of the transect, after upwelling (occupation C). This sample also has a slightly higher absolute gene abundance. The sample collected on the upper slope (~46 km from the onshore start of the transect, max depth 376 m) did not show the same temporal pattern through the upwelling event for absolute 28S gene abundance or 18S relative abundance of *A. tamarense* as the samples on the shelf (Fig. 11, Table S2).

Averaging the surface and chl-*a* max depth samples, the 28S absolute gene abundance on the shelf in occupations A, B, C, and D ($n = 32$) were significantly different from each other using a repeated measures ANOVA ($F = 5.08$, $p = 0.00644$), while the latter three occupations were not significantly different from each other ($F = 1.37$, $p = 0.28$). The same results were seen with the relative abundance of *A. tamarense*, between occupations A, B, C, and D ($F = 16.8$, $p < 0.0001$) and between transect occupations B, C, and D ($F = 1.14$, $p = 0.34$).

The vertical sections of physical variables (temperature and density – Fig. 11, nitrate – Fig. S3) reveal differences throughout the water column between the onset of the upwelling and the subsequent three occupations during/after the event. As the event was beginning during occupation A and the shelfbreak jet was switching directions, weakly stratified warm water was present over the outer shelf. This consisted mainly of Alaskan Coastal Water (> 4°C) with a layer of sea-ice melt water occupying the top 10 m. Seaward of the shelf the cold halocline, centered at

the 26.5 kg m^{-3} isopycnal, was at its deepest depth of the 4 occupations. By contrast, during the next three occupations the warm water on the shelf was largely diminished. In particular, the signature of Alaskan Coastal Water nearly disappeared, replaced by a thicker layer of sea-ice melt water (roughly 25 m thick) and a deep layer of colder, denser Bering Summer Water (BSW) ~-1°C, >32S (Steele *et al.*, 2004) along the bottom of the outer shelf. The stratification in the upper 50m became enhanced, which is consistent with past mooring results (Lin *et al.*, 2019). Furthermore, seaward of the shelf the halocline shoaled and became colder. Note, however, that the denser 27.0 and 27.5 kg m^{-3} isopycnals were at their shallowest depth during occupation B, consistent with the AON mooring data (Fig. 10B) indicating that this was near the height of the upwelling.

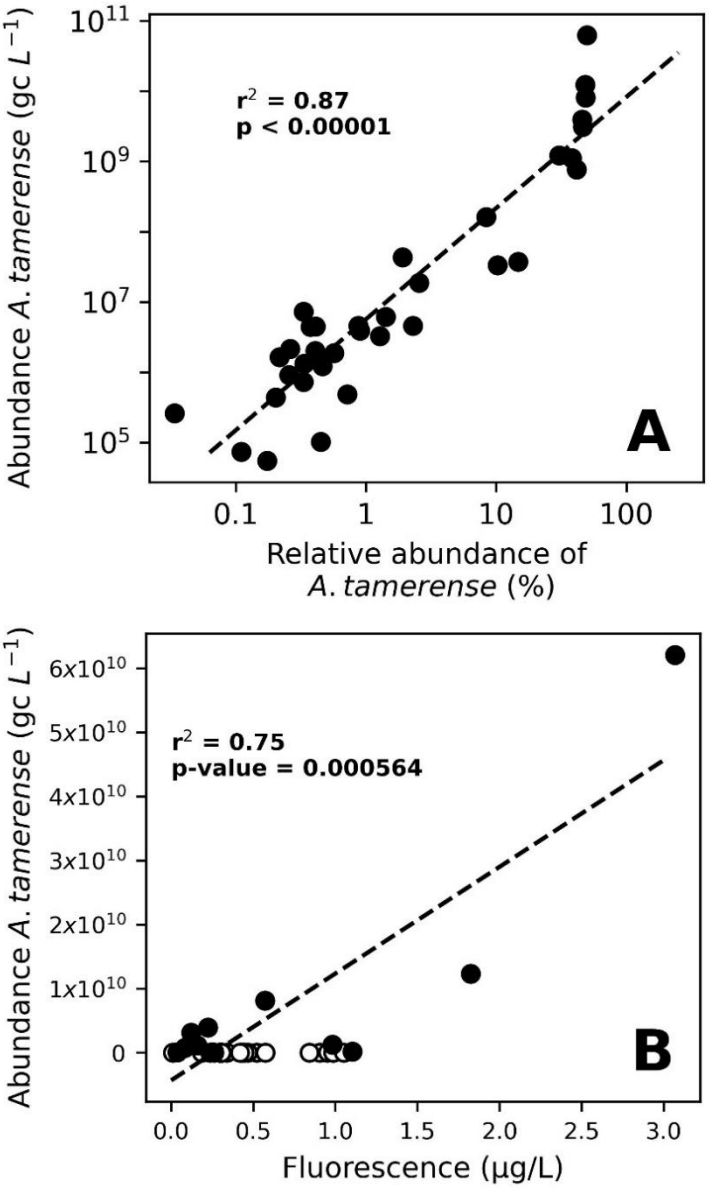

Fig. 12. Observed relationships between *A. tamarense* 28S gene abundance and other measured variables**.** (A) Relationship between relative 18S *A. tamarense* as a fraction of total eukaryotic phytoplankton (dinoflagellates, diatoms, haptophytes) and absolute *A. tamarense* 28S gene abundance; both are on a log scale. (B) Relationship between fluorescence and absolute 28S gene abundance of *A. tamarense*. Samples that had a relative abundance of *A. tamarense* above 5% (from 18S analysis) are solid black circles and samples that had a relative abundance below 5% are empty black circles.

The 18S relative abundance of *A. tamarense* to phytoplankton is plotted against the absolute 28S gene abundance of *A. tamarense* (gc L^{-1}) with both on a log scale in Fig. 12A. The significant correlation ($r^2 = 0.87$, $p < 0.0001$) shows an increase of absolute gene abundance when the relative abundance of *A. tamarense* increases. Fig. 12B shows the relationship between absolute 28S gene abundance of *A. tamarense* (when *A. tamarense* is above 5% 18S relative phytoplankton community) and fluorescence (mg m^{-3}) measured by the CTD with a significant correlation ($r^2 = 0.75$, p-value = 0.000564). When the *A. tamarense* is below 5% of the 18S relative phytoplankton community, no such relationship exists. Absolute gene abundance of *A. catanella* was not found in any of the samples and consequently is not included in Table S2.

DISCUSSION

This study confirms the presence and abundance of *Alexandrium* – specifically the species *A. tamarense* – on the Alaskan BS shelf using imaging and sequencing methods. Dinoflagellates have higher gene copy numbers than other unicellular eukaryotes (Lin, 2011; Cusick and Sayler, 2013), and there is some concern when using 18S sequencing to analyze eukaryotic community composition due to this copy number variability. However, when *Alexandrium* was imaged by FlowCAM (Fig. S2) in a sample (n=5), it corresponded with the five highest samples in terms of *A. tamarense* 18S relative abundance and the five highest absolute 28S gene abundances of *A. tamarense*. Combining these three methods shows that, as the relative abundance of *A. tamarense* increases, so does the absolute gene abundance of *A. tamarense* and the highest levels of *A. tamarense* in both sequencing methods corresponded with the only images of *Alexandrium* seen on the FlowCAM (Table S2).

The results show that the absolute and relative abundances of *A. tamarense* were different at the onset of the upwelling event (occupation A) versus during/after the event (occupations B, C, and D). Although it is widely understood that an increase in nutrients in the euphotic zone leads to higher algal biomass (Cushing, 1971; Tenore *et al.*, 1995; Loubere, 2000; Jackson *et al.*, 2011; Iles *et al.*, 2012), the abundance of *A. tamarense* dramatically dropped during the upwelling, when increased nitrate concentrations were found on the Alaskan BS shelf. Together, our results suggest that the *Alexandrium* population measured during occupation A was being transported eastward by the Beaufort Shelfbreak Jet. This is consistent with previous data collected farther to the west reported by Don Anderson *et al.* (2021) . In that study, high levels of *Alexandrium* were measured on a transect occupied in August immediately east of Barrow Canyon (105 km west of the transect of this study). The cells were located in the warm Alaskan Coastal Water and sea-ice melt water being advected eastward in the Beaufort Shelfbreak Jet, and may have entered the water column from a local seed bed just east of the canyon (Anderson *et al.*, 2021). The absence of both the Alaskan Coastal Water and the *Alexandrium* signal during occupations B, C, and D is likely due to the reversed shelfbreak jet having advected them back to the west. However, the secondary circulation during the upwelling event would tend to transport material offshore in the surface Ekman layer (Schulze and Pickart, 2012), which, together with enhanced wind mixing during upwelling (Spall, 2004) could significantly reduce the surface signature of *Alexandrium* on the shelf.

While the relative abundance of *A. tamarense* accounted for up to 45% of the phytoplankton 18S, it is important to note that this could reflect higher ribosomal gene counts found in dinoflagellates compared with other phytoplankton (Lin, 2011; Gong and Marchetti, 2019). In other words, it would likely be an overestimation to state that *A. tamarense* comprised

45% of the phytoplankton community at this time. While that may be the case, in samples collected at the onset of upwelling (and when *A. tamarense* > %5 of the phytoplankton community), fluorescence had a significant positive relationship with *A. tamarense* absolute gene abundance. Thus, while *A. tamarense* may not have accounted for 45% of the phytoplankton community, we can infer that it was an important part of the phytoplankton biomass at the onset of the upwelling. During and after the upwelling no such relationship is seen between *A. tamarense* gene abundance and fluorescence, no *Alexandrium* images were observed by the FlowCAM, and there was low relative abundance of *A. tamarense* 18S reads. This suggests that, as the shelfbreak jet reversed during upwelling, the *A. tamarense* population decreased and was no longer the dominant phytoplankton. Further evidence that the shelfbreak jet is the main conduit for *Alexandrium* proliferation into the BS is that the sample from the upper slope (~41 km from the onshore start of the transect and further offshore than the shelfbreak jet) showed only slightly enhanced levels of *Alexandrium* at the onset of upwelling (Occupation A).

A. tamarense is one of the species of the genus that forms resting cysts as a part of their life cycle, and *Alexandrium* cysts are known to have an internal clock to bloom when suitable conditions exist (Anderson *et al.*, 2014). *A. tamarense* cysts have been found in temperature ranges from -0.6 to 26.8 °C, with the highest abundances found between 5 - 15 °C (Marret and Zonneveld, 2003). The surface temperature on the shelf at the onset of the upwelling event was > 5 °C. Due to the ability of *Alexandrium* to produce resting cysts to survive and take advantage of suitable conditions (Wall, 1971; Anderson *et al.*, 2014; Brosnahan *et al.*, 2017), it may be important to monitor this area for future *Alexandrium* blooms. The region of the shelf where *A. tamarense* was observed is relatively shallow (~21 m to 56 m), thus strong storms that lead to mixing events on the shelf, could resuspend *Alexandrium* cysts and possibly lead to a bloom. It

has been noted that *Alexandrium* may produce saxitoxin as a pheromone or as an indicator of cyst settlement (Wyatt and Jenkinson, 1997); thus, if an *Alexandrium* bloom is observed in this area, saxitoxin and any further bioaccumulation will need to be monitored closely.

Not all species or even strains of *Alexandrium* produce saxitoxin (Anderson *et al.*, 2012). However, there are documented cases of *Alexandrium,* and saxitoxin bioaccumulation, seen along the Alaskan coast up to and just east of Pt. Barrow (Lefebvre *et al.*, 2016). Presumably, the Alaskan Coastal Current brings warm water suitable for *Alexandrium* populations to thrive and produce enough saxitoxin that eventually leads to deaths in mammals. Finding *A. tamarense* this far east on the Alaskan BS shelf indicates that the shelfbreak jet continues transporting warm water suitable for *Alexandrium* population expansion well past Barrow Canyon. It should also be noted that strong westerly winds are common in this region, which accelerate the shelfbreak jet and lead to downwelling (Foukal *et al.*, 2019). This is notable, as it is similar to an anomaly that aligned with an *A. fundyense* bloom in the Gulf of Maine where downwelling favorable winds were thought to have caused a coastal accumulation of *Alexandrium* (McGillicuddy *et al.*, 2014).

Easterly winds in the Alaskan BS intensify in the fall, and upwelling activity increases (Pickart *et al.*, 2013a; Lin *et al.*, 2016). This tends to slow the shelfbreak jet, flux warm surface water offshore, and upwell colder water from the basin. Indeed, BSW replaced much of the Alaskan Coastal Water over the outer shelf on occupations B-D. This upwelled water was several degrees colder, changing the environmental conditions away from the warmer and less saline conditions more suitable for *Alexandrium* (Weise *et al.*, 2002). These results suggest that if *A. tamarense* were to bloom, it would occur earlier in the Arctic summer when the shelfbreak jet advects warm water to the BS and the region is not subject to as much upwelling. It is worth noting, however, that there are evolutionary adaptations in *Alexandrium* species that could allow

for survival during upwelling, such as temporary chain formations and shifts in swimming velocity to adjust to turbulence (Smayda and Trainer, 2010). These evolutionary advantages suggest that upwelling should not deter *Alexandrium* from surviving on the Alaskan BS shelf.

Dinoflagellates do not have a biogenic exoskeleton like diatoms and haptophytes and the prevalence of *Alexandrium* in the shelfbreak jet and on the Alaskan BS shelf leads me to hypothesize that with increased heat transport into the Arctic *Alexandrium* prevalence will continue. This would likely be associated with lower carbon export and less upper trophic level transport. Ultimately, this would lead to lower production at both primary and upper trophic levels. A caveat is that an increase in upwelling events in a warmer climate with reduced ice coverage could potentially reverse this trend, as will be discussed further in Chapter IV. Although dinoflagellates of the genus *Alexandrium* have been measured along the Alaskan coastline to just east of Barrow Canyon (Lefebvre *et al.*, 2016), to my knowledge *A. tamarense* has not been found this far east on the Alaskan BS shelf before. Heat transport by currents into the Arctic is predicted to continue increasing (Marshall *et al.*, 2014; Marshall *et al.*, 2015) and presumably the Beaufort shelf will continue to warm. Higher temperatures in coastal waters have been determined to cause the accumulation of *A. tamarense* in the Gulf of Maine (He and McGillicuddy Jr., 2008), and with the likely warming of the BS shelf, I hypothesize that the same may occur here. However, since upwelling along the BS shelf is predicted to increase as well (Pickart *et al.*, 2013a), there are competing forces. Either way, it is prudent to begin monitoring *Alexandrium* in this area.

CHAPTER IV

PHYTOPLANKTON COMMUNITY SHIFTS FROM ALASKAN BEAUFORT SEA UPWELLING: IMPLICATIONS FOR A CHANGING ARCTIC

INTRODUCTION

Phytoplankton blooms can occur due to a pulse of nutrients, such as those that occur in upwelling or other water column mixing that brings nutrients to the euphotic zone (Degerlund and Eilertsen, 2010; Gerringa *et al.*, 2012). Cold upwelled water is almost always nutrient rich and is one of the main drivers of phytoplankton growth (Davis *et al.* 2014). BS upwelling is primarily driven by wind, specifically due to a shift from westerly to easterly alongshore winds and is strongest when there is less ice, as the wind is able puts more stress on the water column (Schulze and Pickart, 2012). If there is a sustained easterly wind for over 8 hours, it will lead to upwelling of saltier nutrient rich water onto the shelf (Schulze and Pickart, 2012; Pickart *et al.*, 2013a). In the absence of upwelling, the shelf break jet brings warm Pacific-origin surface water into the BS (Walsh *et al.* 1989) by the Alaskan Coastal Jet, but in response to the upwelling, this current reverses bringing water from the East while warmer and saltier and nutrient rich AW is upwelled (Woodgate *et al.*, 2010; Pickart *et al.*, 2011).

In the past, there were years when the BS would stay completely ice covered throughout the year, but because of the warming climate the BS shelf has seen retreating sea ice cover and an increase in upwelling strength leading to an increase in primary production in the fall (Schulze and Pickart 2012). The predicted increase in upwelling events and decrease in sea ice can lead to more nutrient rich upwelling water reaching the BS shelf than previously seen. This

will likely drive increased abundance of some phytoplankton that respond to upwelled nutrient rich water, such as diatoms (Biller *et al.*, 2013). The increase in phytoplankton on the shelf can also lead to an increase in bowhead whales, other marine mammals, and seabirds (Falk-Petersen *et al.*, 2015), indicating likely changes to the entire ecosystem in this location.

An increase in phytoplankton abundance is not all that matters, as the difference in cell size, functional type, and metabolism of different phytoplankton influences trophic structure and biogeochemical cycling (Mena *et al.*, 2019). In nutrient deplete waters, the community predominantly consists of small phytoplankton, such as picoplankton, while the trophic structure favors remineralization or nutrient recycling, instead of transfer to upper trophic levels, leading to low carbon export (Marañón, 2015; Mena *et al.*, 2019). While nutrient rich regimes, such as those caused by upwelling, are normally dominated by larger phytoplankton such as diatoms with efficient export to higher trophic levels and increased carbon export (Marañón, 2015; Mena *et al.*, 2019), which was also described in detail in Chapter II. Thus, the phytoplankton community structure supports higher trophic level growth and efficiency of carbon export from the euphotic zone when larger phytoplankton, such as large diatoms, are abundant but both growth and efficiency of carbon export decreases when large diatoms are replaced by smaller phytoplankton (Basu and Mackey, 2018).

This study is focused on how upwelling influenced the relative abundance of 4 main groups of phytoplankton, diatoms, haptophytes, dinoflagellates, and other picoeukaryotes. Primarily, aggregate material being exported from the euphotic zone is dependent on the proportion of biominerals, including silicate and carbonate, which include diatom and coccolithophorid tests and liths, respectively (Basu and Mackey 2018; and references therein) . Diatoms are unicellular phytoplankton with a silica exoskeleton generally found to be most

abundant in coastal areas and known to bloom when upwelling brings nutrients to the euphotic zone (Biller *et al.*, 2013). Diatoms have also been shown to aggregate and sink after blooms cease, leading to enhanced carbon export below the euphotic zone (Kiørboe *et al.*, 1998). The haptophyte group consists mostly of coccolithophores, with a calcium exoskeleton and drive significant export of carbon incorporated in fecal pellets (De La Rocha and Passow, 2007). Dinoflagellates on the other hand are primarily not seen to be a significant exporter of carbon, as they don't have shells and are most often associated with stratified low nutrient waters (Smayda and Reynolds, 2003). However, some dinoflagellate species create cysts that can enhance carbon export (Spilling *et al.*, 2018). Picoeukaryotes are <2 µm in size, ubiquitous in the ocean, and account for a major portion of primary production in today's oceans but due to their small size are mostly remineralized within the euphotic zone and are not a major contributor to carbon export (De La Rocha and Passow 2007; and references therein) . These 4 groups account for most of the primary production in the ocean and have a strong influence on upper trophic levels and carbon export, however, the overall impact in each location is dependent on the phytoplankton species composition.

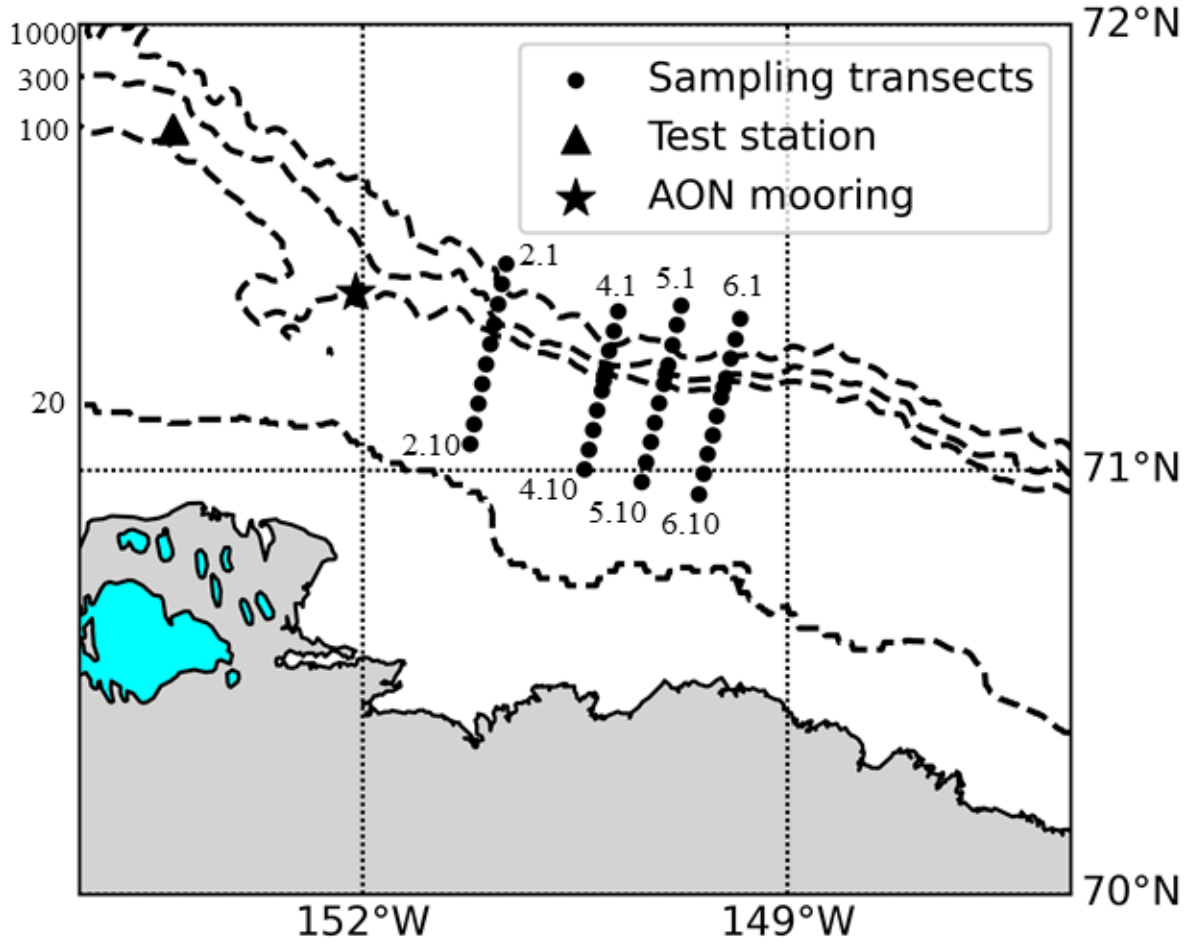

Fig. 13. Location of sample collection sites along the BS shelf break. The labeled stations indicate the station numbers associated with the offshore and nearshore ends of each transect. The dashed lines show the locations of the 20 m, 100m, 300m, and 1000m isobaths. Further visualization of BS Gyre, shelfbreak jet, mooring location is shown in Fig. 9 (Chapter II).

This project studied three separate upwelling events that occurred across the BS shelfbreak from August 30th – September 9th, 2017. A total of 9 occupations of 4 different onshore-offshore transects were sampled (Fig. 13) to determine the influence these upwelling events have on the eukaryotic phytoplankton community. The relative abundance of the 4 major groups of phytoplankton listed above shifted dramatically in response to these upwelling events. This has implications for future predictions of phytoplankton community composition, carbon export, and upper trophic level activity in the Alaskan BS, as upwelling events are predicted to increase in number and strength along the shelf due to global warming. This area is likely to be a location of rapid shifts in the phytoplankton community in response to enhanced warming by the shelfbreak jet and these upwelling events.

METHODS

A research cruise on the R/V Sikuliaq sought to measure the physical and biological dynamics of upwelling in the Alaskan BS. Samples were collected over the shelf and shelfbreak across 9 total transects, with 4 unique transect locations (Fig. 13) over ~10 days (August 30th – September 9th, 2017). The sample collection period spanned 3 different upwelling events. While not all transect locations were repeated, they are all within ~60 km of each other along the shelfbreak. The timeline of upwelling events and sample collection is listed in Table 2.

Physical data collection

Each transect had 8-11 conductivity-temperature-depth (CTD) stations spaced ~5-10 km apart with physical data collected using the same equipment explained in detail in Chapter III. Each transect occupation took between 6-18 hours. The equipment and analysis for the data

collected by the nearby mooring deployed as part of the Arctic Observing Network (AON) (Lin *et al.*, 2019), wind data from the Utqiaġvik, AK meteorological station, and 10-m wind and sea-level pressure fields from the ERA5 reanalysis (Hersbach *et al.*, 2018) is also explained in detail in Chapter III.

Table 2. Simplified description of physical dynamics during each transect in order of occurrence.

Transect	Description	Day
2A	Beginning/Before first upwelling event	1
4A	Peak of first upwelling event	2
2B	At end of first upwelling event	3
2C	Between first/second upwelling event	5
2D	During the second upwelling event	6
4B	Prior to third upwelling event	8
6A	Peak of third upwelling event	10
5A	Close to end of third upwelling event	11
2E	End of third upwelling event	11

DNA sample collection, extraction and sequencing analysis

Near-surface water was collected using Niskin bottles attached to the CTD rosette and sampled into 10% HCl acid cleaned Nalgene bottles. Between 1.2 and 4.5 L of sea water were filtered onto Sterivex filters by peristaltic pump and immediately frozen at -80C until DNA extraction. The DNeasy Plant Mini Kit (Qiagen) was used to extract DNA from Sterivex filters using the same detailed method in Chapter III.

Extracted DNA was amplified in triplicate by PCR (SimpliAmp, Applied Biosystems) using 1x master mix (Phusion HF Mastermix, ThermoFisher) and primers used to amplify the SSU rRNA 18S V9 marker gene based on those designed by the 18S Illumina Earth Microbiome Project (Stoeck *et al.*, 2010). Triplicates were pooled, purified using Mag-Beads (AMPure XP, Beckman Coulter), amplified again to attach MiSeq indices (Illumina), and purified again. Amplified DNA was sequenced on the Illumina MiSeq Desktop Sequencer at Old Dominion University using a 2x300-bp kit.

Sequences were analyzed by pipeline analysis using DADA2 (Callahan *et al.*, 2016), and ASV's were identified using BLASTN (Altschul *et al.*, 1990) using the same in-house database described in Chapter III. Subsequent analysis only focused on ASVs that were identified as having the potential to be photosynthetic to determine changes in the phytoplankton community only. Identified ASVs were grouped first based on class to group into known phytoplankton groups, including diatoms (Bacillariophyceae), haptophytes (Haptophyceae), dinoflagellates (Dinophycaea), and picoeukaryotes (Chlorophyta), were gone through individually to determine photosynthetic ability. ASVs were condensed into OTU_{99}s using CDhit (Li and Godzik, 2006) on the representative fasta sequences if they had >99% similarity, and ASV counts were subtotaled for each OTU_{99} cluster. 18S OTU_{99} sequence hits were grouped into 4 groups for further

analysis, including dinoflagellates, diatoms, haptophytes, and other phytoplankton. The other group consisted primarily of picoeukaryotes. For further analysis of phytoplankton community composition on the shelf only, statistical analysis focus on samples collected from locations with a bottom depth < 120 m, which is the bottom depth of the AON mooring (Fig. 14). This depth was chosen as we can assume that these shelf and shelfbreak samples were directly influenced by shelfbreak jet reversal and upwelling, while samples further offshore are more likely to be affected by Ekman transport off the shelf and thus may have a lag between upwelling event and influence on the phytoplankton community. As such, further statistical analysis described below was done only on these samples, which were further up the shelfbreak and on the shelf. Primer v7 (Primer-e) software was used to square root transform raw sequence counts and calculate Bray-Curtis similarity distances (Bray and Curtis, 1957). Samples were clustered into dendrograms, with a SIMPROF test (1000 permutations) to determine branch significance. BEST analysis was conducted to find similarity distance correlation with environmental variables (SST, salinity, density and fluorescence) using the Bio-env method (Clarke and Ainsworth, 1993) with significance determined by 10000 permutations. Shelf stations samples (bottom depth < 120) were grouped based on the upwelling strength and the direction of the shelfbreak jet. They were grouped based on if the 26 kg m^{-3} isopycnal at the AON mooring is above or below 80 m depth. This depth was chosen as it is an indication of peak upwelling strength based on patterns seen in Fig. 14. Additionally, the samples were grouped based on direction of the shelfbreak jet, 1 for regular directional flow (to the East), 0 for complex flow (switching direction), and -1 for reversed flow (to the West). PERMANOVA (Permutational Manova) was run on the Bray-Curtis distances of these samples and the two different groupings described above, using Primer v7 software.

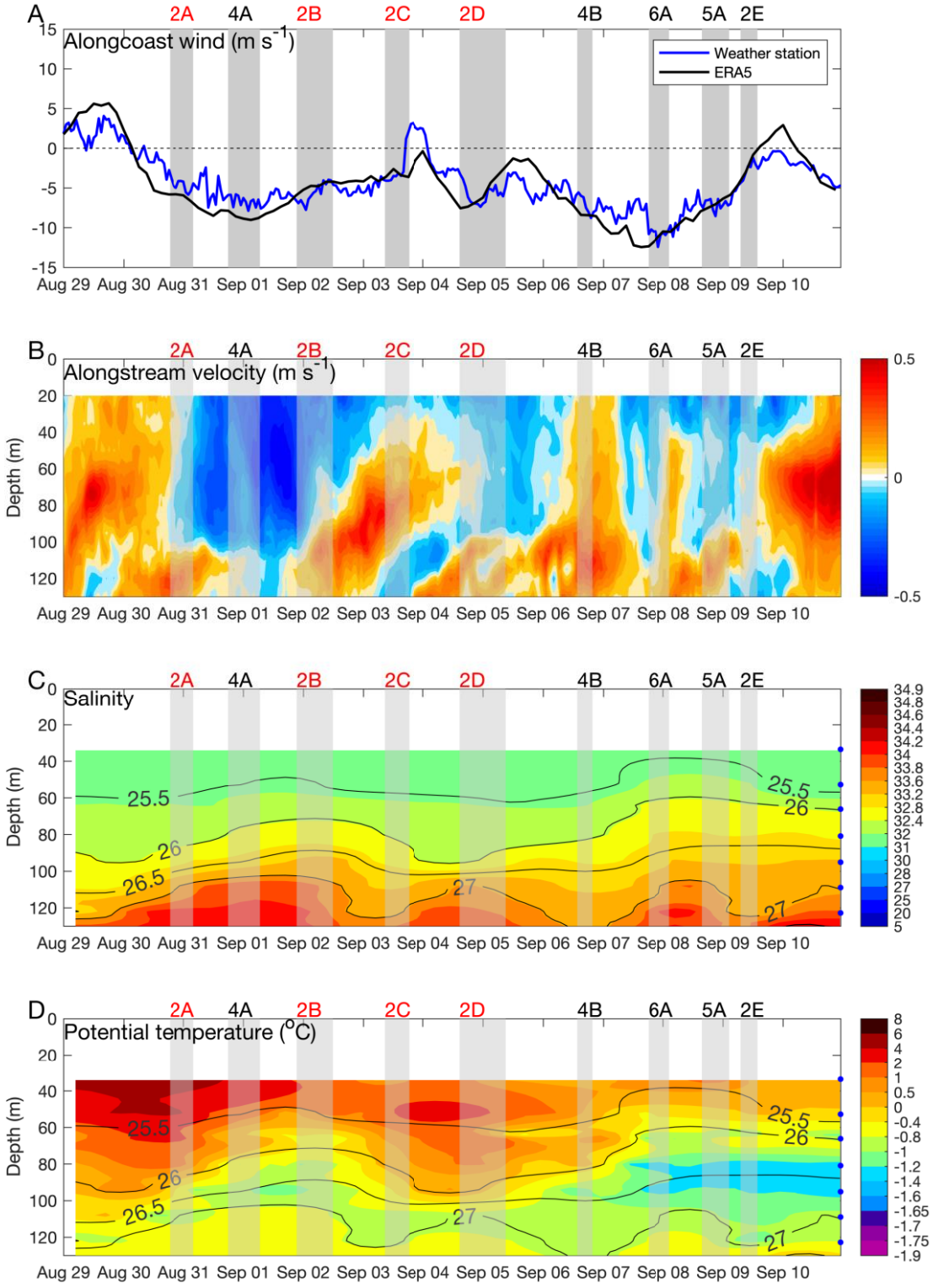

Fig. 14. Timeseries of physiochemical properties during upwelling events. (A) Timeseries of the alongcoast wind speed (m s^{-1}) recorded at the Utqiaġvik weather station and the ERA5 reanalysis.

Fig. 14. Continued. Negative values correspond to winds from the east and positive values correspond to winds from the west. The grey bars denote the time periods of the nine sampling transects during the cruise. (B) Variations of the depth-dependent alongstream velocity (m s^{-1}) recorded at the AON mooring, where positive values indicate current is moving to the east and negative values indicate current is moving to the west. (C) Salinity measured at the AON mooring site overlain by potential density (kg m^{-3}) contours. The blue dots denote the locations of the MicroCATs on the mooring. (D) Potential temperature (^{o}C) measured at the AON mooring site overlain by potential density (kg m^{-3}) contours.

RESULTS AND DISCUSSION

Alongshore surface wind (Fig. 14A), along stream current speed (Fig. 14B) and potential temperature/density (Fig. 14C) measured by the AON mooring reveals that the sampling period covers three separate upwelling events that occurred along the shelfbreak in this region of the Alaskan BS. Before upwelling occurs, the surface shelfbreak jet is bringing > 4°C Alaskan Coastal Water (ACW). When the alongcoast wind is negative (Fig. 14B), due to an Aleutian low storm (Fig. S1), the wind component is easterly, leads to the shelbreak jet reversal and ultimately upwelling, when this easterly wind speed is above 4 m/s (Pickart *et al.*, 2013b). Saltier Atlantic Water (S > 33; von Append and Pickart, 2012) is evident above the 120 m depth (Fig. 14C), and is brought up the shelfbreak as upwelling occurs, consistent with previous literature as a signature for upwelling along the Beaufort shelf (Pickart *et al.*, 2011).

Sampling of transects 2A, 4A, and 2B occurred during different stages of the first upwelling event. During the time that transect 2A was sampled, or before the first upwelling event, the alongstream flow was in the process of reversing throughout the water column, indicating reversal of the shelfbreak jet. Only the bottom layer had not reversed, and indications of saltier, warmer AW was present in the bottom layer (Fig. 14). During the period that transect 4A was sampled, the first upwelling event was close to its peak, while the shelfbreak jet reversal flow was enhanced and the AW water extended to a depth of 100m.

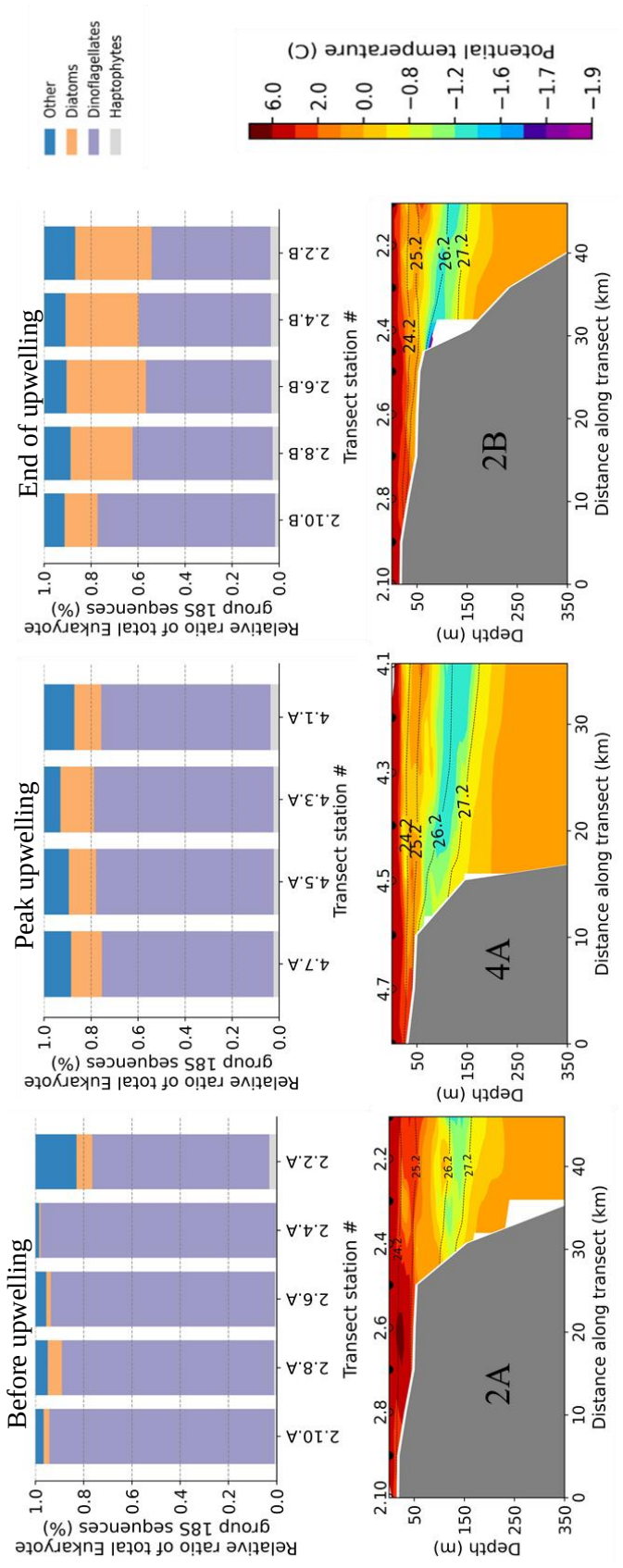

Fig 15. Relative abundance of eukaryotic phytoplankton groups plotted for each transect above the corresponding potential temperature (°C) and density (σ_t) contour profiles from CTD stations. Transects 2A, 4A, and 2B, which were sampled at different stages of the first upwelling event.

The 2A transect hydrography is consistent with the mooring as warm surface water is evident along the shelfbreak and shoaling of isopycnals has not begun, except only slightly at 120 m depth (Fig. 15). The phytoplankton community during the time of transect 2A is dominated by dinoflagellates. During 4A there is shoaling of the 26.2 isopycnal to ~60 m and small appearance of BSW (Temperature = 0-3 °C, Salinity = 32-33; Yang and Bai 2020) at 120m (Fig. 15), consistent with the mooring data in Fig. 14, although there is a greater shoaling of the isopycnals at the AON mooring. Transect 4 is further west of the mooring than transect 2 (Fig. 13), which can explain why there is a difference between mooring and transect hydrographic data. The hydrographic data from the transect is a snapshot image of the physical dynamics while the mooring is continuous and a better descriptor of the overall physical dynamics of the shelfbreak jet and upwelling stages along the shelfbreak. Although there may be slight differences between mooring and transect hydrographic dynamics, they are consistent in showing upwelling along the shelfbreak. During transect 4A, diatoms increase in relative abundance on and along the shelf and shelfbreak compared with transect 2A and even higher relative abundances of diatoms are subsequently observed during transect 2B (Fig. 15). Sampling of transect 2B occurred close to the end of the first upwelling event, as the shelfbreak jet was rebounding in the deeper waters and the saltiest near-bottom water relaxed. This likely indicates that although the first upwelling event was already at its peak during transect 4A, the peak biological response to increased nutrients and turbulent surface water undergoes a slight lag relative to the timing of the physical dynamics of upwelling, about one day after peak upwelling.

Transect 2C was sampled between upwelling event one and two, at a point when the shelfbreak jet flow was complex and the AW was no longer seen (Fig. 14). In the Transect 2C hydrographic snapshot (Fig. 16), the 26.2 isopycnal is still shallow but warmer water is apparent

at >60 m depth, both of which are consistent with what is observed at the mooring. During the period that transect 2D was sampled, the second upwelling event was occurring, the shelfbreak jet had reversed and AW was present at the bottom again (Fig. 14) while the warmer water >60 m depth was gone, and colder water had reappeared on the shelf in the transect hydrography (Fig. 16). During the time that transect 4B was sampled, the shelfbreak jet was flowing to the east and no dense water was present in deeper waters indicating that the second upwelling event had relaxed before transect 4B was sampled (Fig. 14), which is supported by the warmer water reappearing at >60 m depth (Fig. 16). While alongstream velocity and density contours support that transect 4B was not sampled during upwelling, the easterly wind that would lead to the third upwelling event had already begun during transect 4B (Fig. 14A). Although transect 2C, 2D, and 4B overlap the full second upwelling event, the biological response is not consistent with "before", "during" and "after" upwelling. Where we might expect to see higher relative abundances of dinoflagellates, similar to transect 2A, "before" upwelling and a greater abundance of diatoms "during" and "after" the upwelling event, corresponding to transects 2D and 4B, the community is relatively similar between each of these transects (Fig. 16). A possible explanation for this is the fact that the first upwelling event occurred only ~1 day earlier and the sampling of 2C, 2D, and 4B, occurred over the span of ~3 days. This rapid timeline associated with consecutive upwelling events could result in small changes to biological observations because the organisms did not have time to equilibrate to rapidly changing physical dynamics along the shelfbreak and continuing upwelling events keep the responding phytoplankton on the shelf. In support of this, the hydrographic data for transects 2D and 4B, which are "before" and "after" the second upwelling event, are not consistent with that of transect 2A collected before the first upwelling event (Fig. 16), suggesting that the hydrography had not fully equilibrated to

upwelling relaxation. Given that, it is not surprising that the biological observations did not appear fully equilibrated to a state associated with a relaxation of upwelling.

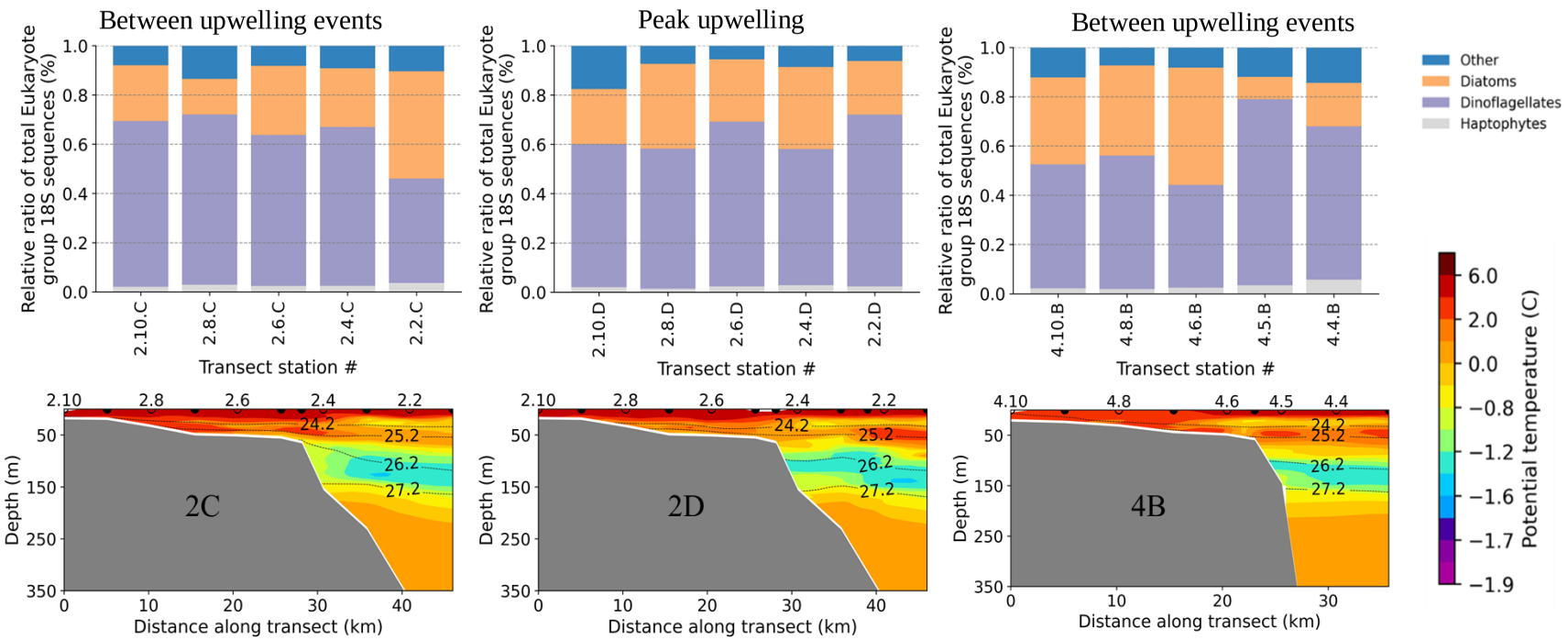

Fig. 16. Relative abundance of eukaryotic phytoplankton groups plotted for each transect above the corresponding potential temperature (°C) and density (σ_t) contour profiles from CTD stations. Transects 2C, 2D, and 4B, which were sampled at different stages of the second upwelling event.

Transect 6A was sampled at the peak of the third upwelling event when the easterly wind was at its maximum, the shelfbreak jet had reversed, and the dense bottom water had appeared again (Fig. 14). Consistent with the mooring, the hydrography (Fig. 17) shows the coldest temperatures on the shelf, and a reappearance of the BSW at ~80 m depth. During sampling of transect 5A, the third upwelling event was beginning to relax, the easterly wind had weakened, the shelfbreak jet had rebounded in the deeper waters, and the isopycnals near the bottom were relaxing (Fig. 14C and D). Additionally, the hydrographic data (Fig. 17) shows warmer waters on the shelf and less indication of BSW at ~80 m depth. Finally, transect 2E was collected at the end of the third upwelling event when the easterly wind had weakened further, the near-bottom dense water was gone, and the flow had become complex (Fig. 14). Although the hydrographic data available for transect 2E does not cover the whole transect, similar temperatures are apparent on the shelf compared to transect 5A (Fig. 15C). The biological response during the third upwelling event (Fig. 17) does not show a big change in diatom relative abundance compared to what was observed during and after the second upwelling event (Fig. 16), likely indicating that the short time frame between upwelling periods once again has not allowed for the biological response to respond to upwelling relaxation.

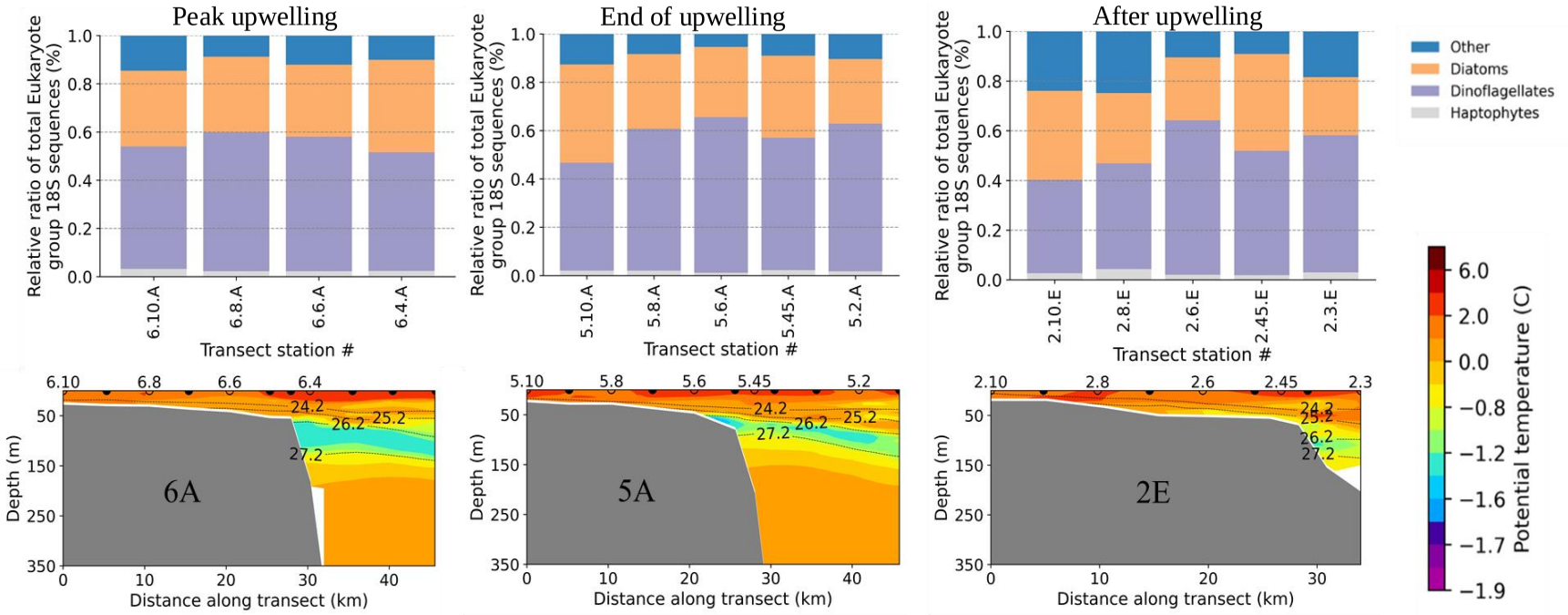

Fig. 17. Relative abundance of eukaryotic phytoplankton groups plotted for each transect above the corresponding potential temperature (°C) and density (σ_t) contour profiles from CTD stations. Transects 6A, 5A, and 2E, which were sampled at different stages of the third upwelling event.

Although the greater phytoplankton community from samples that included the slope did not appear to shift differently between each of the upwelling events, when examined at broad taxonomic groupings (Figs. 15, 16 and 17), stations located on the shelf and shelfbreak (bottom depth <120m) were further analyzed to determine if there were differences between upwelling events at the genus level. The bottom depth 120m was chosen as it is the same bottom depth of the AON mooring's deepest sensor and about 20 m above the bottom (Fig. 14). This analysis also used a proxy for upwelling that I determined could be indicative of upwelling influence on the shelf and shelf break phytoplankton community based on the continuous data from the AON mooring (Fig. 14B). The following explains the justification for this proxy. When winds became easterly and alongshore on August 30th (Fig. 14A), the shelfbreak jet begins to reverse over the next day until it is fully reversed on August 31st (Fig. 14B). During this shelfbreak jet reversal, the 26 kg m^{-3} isopycnal shoals, and salty AW appears at 120 m depth beginning August 30th-31st (Fig. 14C). This appearance of AW water has been shown previously to be a signature of upwelling in this region (Pickart *et al.*, 2011). The shallowest depth of the 26 kg m^{-3} isopycnal during the first upwelling event (just above 80 m) occurred during full reversal of the shelfbreak between September 1st and September 2nd. Once the easterly winds taper off at the end of the first upwelling event and the shelfbreak jet reverts to its normal directional flow, the 26 kg m^{-3} isopycnal sinks below 80 m depth and AW at the bottom is no longer detected. A similar pattern was observed in the two subsequent upwelling events. As such, each shelf and shelfbreak station was grouped based on my upwelling proxy of the 26 kg m^{-3} isopycnal depth at the AON mooring being either "above" or "below" 80 m depth (Fig. 14C and D, Table S3) as this depth was determined to be an indicator of likely upwelling at the shelfbreak.

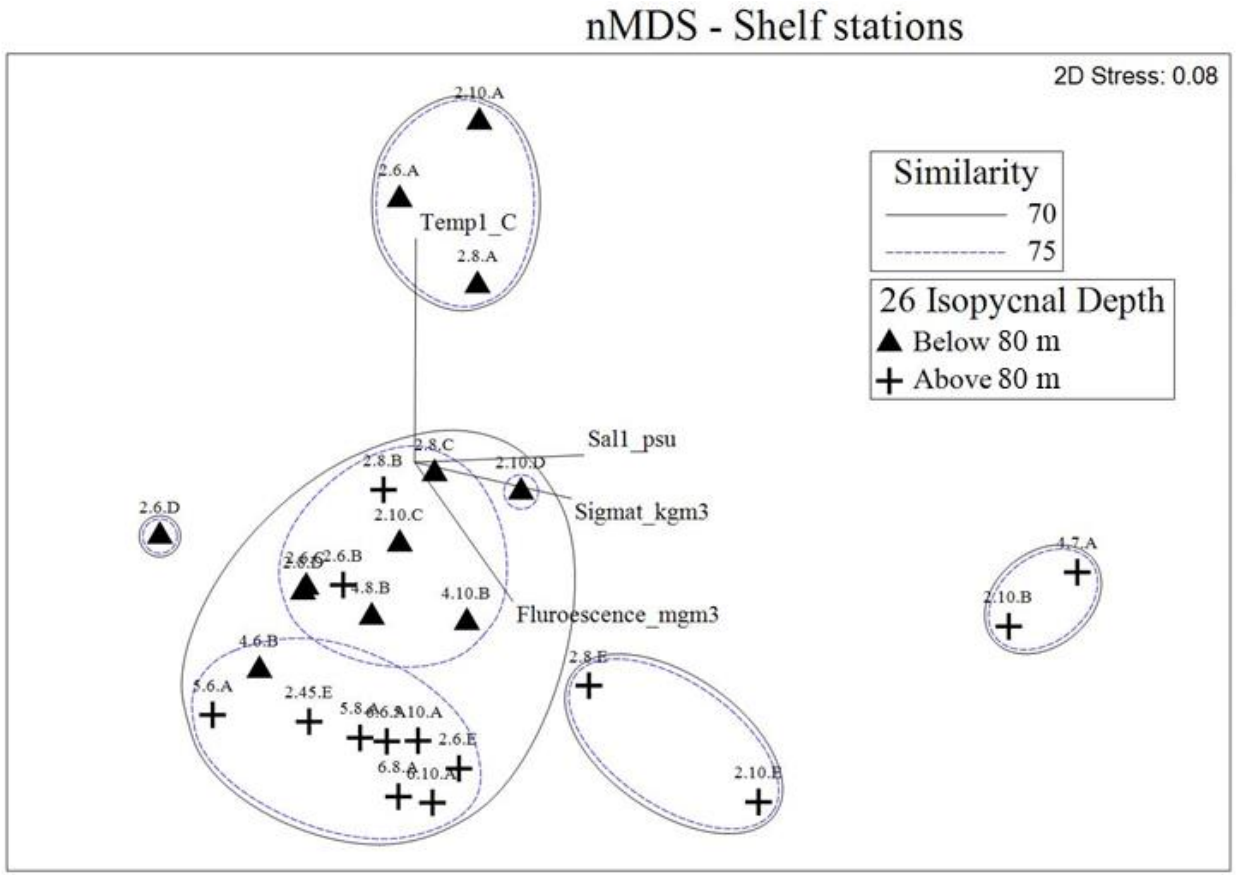

Fig. 18. nMDS plot of Bray-Curtis similarity based on phytoplankton sequences of all stations with <120m bottom depth. Stations are grouped by the depth of the 26 kg m^{-3} isopycnal as measured at the AON mooring being below or above the 80 m. Bray-Curtis similarities of 70% and 75% are visualized.

A two-dimensional nMDS plot of the Bray-Curtis similarity of all shelf stations (Fig. 16) shows a differentiation between the "below 80 m" and "above 80 m" groups, although there is overlap primarily with stations 2.6.B and 2.8.B. A PERMANOVA (Permutational Manova) test revealed a significant relationship between this grouping and the Bray-Curtis similarity of the phytoplankton community (10000 permutations; $p = 0.0003$), indicating that the depth of the 26 kg m^{-3} isopycnal correlates with phytoplankton community shifts on the shelf. BEST analysis on the relationship between continuous environmental variables and the Bray-Curtis similarity matrix for these shelf and shelfbreak stations shows a significant correlation to temperature and salinity ($\rho = 0.57$, $p = 0.001$). These data are a further indication that there is an influence of upwelling on the phytoplankton communities at the shelf stations, as during upwelling colder and saltier water replaces the warmer less saline Pacific surface water transported by the shelfbreak jet when upwelling is not occurring (Pickart *et al.*, 2013b). Fluorescence also appears to correlate with the sample ordination in the nMDS plot of shelf samples in all transects sampled after 2A, or during and after all three upwelling events (Fig. 18), indicating fluorescence increased as a response to the upwelling events. Samples were also grouped based on the direction of the shelfbreak jet, (Table S3). A PERMANOVA test did not show a significant relationship between this group and the Bray-Curtis similarity of the phytoplankton community (10000 permuations; $p = 0.415$). This may be due to a likely lag or disconnect between the shelfbreak jet flow and its influence on the phytoplankton community on the shelf, as upwelling usually begins about ~12 hours later after the shelfbreak reversal (Schulze and Pickart, 2012).

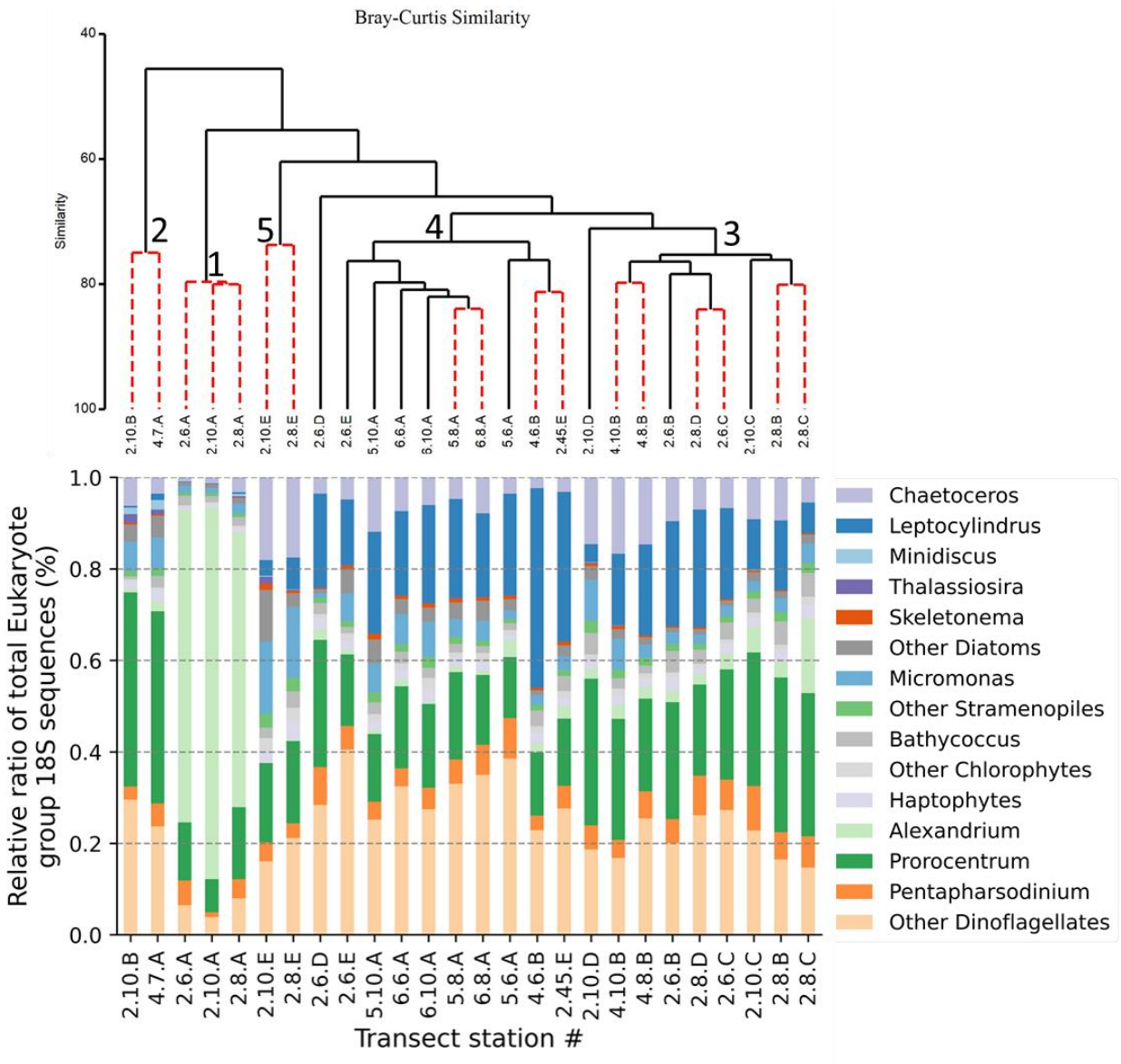

Fig. 19. Dendrogram (Bray-Curtis similarity) of shelf/shelfbreak stations with relative abundance of the phytoplankton community, grouped to the individual genus level if relative abundance > 5% and were otherwise grouped into “Other”. Dashed branches indicate non-significant differences in resemblance (SIMPROF). Each branch cluster is labeled when similarities are greater than 70 %, except for clusters 3 and 4 which are 70% similar and are differentiated at the 75 % similarity level.

The Bray-Curtis similarity of the 18S phytoplankton community classified down to genus level from all shelf/shelfbreak surface samples shows five main branch clusters that cluster together at > 75% similarity: Cluster 1 – 2.6.A, 2.8.A, & 2.10.A; Cluster 2 – 2.10.B & 4.7.A; Cluster 3 – 2D, 2C, 4B; Cluster 4 – 6A, 5A and 2E; and Cluster 5 – 2.10.E & 2.8.E (Fig. 19). Relating these cluster groups to upwelling stages, cluster 1 includes stations sampled before the first upwelling event, while cluster 2 includes stations located closest to the coast during the peak of the first upwelling event. Cluster 3 includes transect stations sampled during and just after the first and second upwelling events. Cluster 4 includes most transect stations collected during and after the third upwelling event, however the most coastal stations at the end of the third upwelling event grouped separately in Cluster 5.

The phytoplankton community in cluster 1, which groups together transect 2A shelf stations, is dominated by dinoflagellates and specifically the genus *Alexandrium* while few relative 18S sequence reads are seen for diatoms, haptophytes, and other dinoflagellates. When the first upwelling event nears its peak and 26 kg m^{-3} isopycnal shoals above 80 m (Fig. 14C), *Alexandrium* all but disappears from the 18S sequence reads. A more detailed discussion of the significance of elevated *Alexandrium* abundance on the shelf is presented in chapter III.

In cluster 2, which groups the most coastal stations of transect 4A and 2B, *Chaetoceros* (diatom), *Micromonas* (picoeukaryote), and *Prorocentrum* (dinoflagellate) reads increase the most in relative abundance in the phytoplankton community. *Chaetoceros* is a well-studied genus of diatoms commonly found in coastal upwelling regions and are known to respond quickly to nutrient pulses (Cupp, 1943; Assmy *et al.*, 2007; Hoffmann *et al.*, 2008). There is also a slight increase in two other diatom genera sequence reads, *Thalassiosira* and *Minidiscus*, associated with cluster 2. Species of the *Thalassiosira* genus are very diverse but generally are

abundant in diatom blooms and the relative abundance of certain species has been found to correlate with dissolved iron concentrations (Hoppenrath *et al.*, 2007; Chappell *et al.*, 2013), which likely increased because of upwelling. Species of the *Minidiscus* genus (as explained in Chapter II) are some of the smallest diatoms (Hasle and Syvertsen, 1997; Leblanc *et al.*, 2018). Some species of *Thalassiosira* can also be quite small, although the genus is diverse (Round *et al.*, 1990; Chappell *et al.*, 2013), but the predominant species of *Thalassiosira* sequenced here was the small *T. minima* (Guinder *et al.*, 2012). *Thalassiosira* and *Minidiscus* sequences were not seen again at that level throughout the remainder of sampling, suggesting that these smaller diatoms were only abundant during the first upwelling event. Likely indicating that carbon export increased in subsequent upwelling events, when these smaller diatoms were replaced by larger ones.

Micromonas is a ubiquitous genus of picoeukaryotes with efficient strategies of phosphate uptake (Whitney and Lomas, 2016) and seen to grow well under CO_2 elevated conditions (Meakin and Wyman, 2011). Upwelling normally brings high CO_2 concentrations and lower pH to the surface ocean (González-Dávila *et al.*, 2017), explaining why *Micromonas* was abundant in recent upwelling, which also likely resulted in elevated phosphate concentrations on the shelf/shelf break though this was not measured in this study, but its efficient phosphate uptake may have given it an advantage during upwelling. Future ocean predictions have the surface ocean becoming warmer with higher concentrations of CO_2; thus, it is likely to expect higher abundances of picoplankton such as *Micromonas*. This has implications for carbon export as *Micromonas* are not associated with enhanced carbon export due to their small size (De La Rocha and Passow, 2007). *Prorocentrum* on the other hand is a globally found dinoflagellate and often benthic or epiphytic (Tarazona-Janampa *et al.*, 2020) and known for the ability to produce

okadaic acid (OA) (Weimin *et al.*, 2010), a toxin associated with shellfish poisoning. Implications of which can range from bioaccumulation in upper trophic levels, to affected local fisheries.

While *Chaetoceros* and *Micromonas* are likely to be responding to increasing nutrient concentrations due to upwelling, *Prorocentrum* is presumably being brought up to the surface through mixing in this location of the shallow BS shelf. Although *Prorocentrum* is also seen in the relative community in cluster 1, which included stations sampled as the first upwelling event was being initiated, it accounts for a smaller fraction of the community compared to its relative abundance in cluster 2. From this, I hypothesize that *Prorocentrum* is consistently present on the Alaskan BS shelf, as has been previously detected in the Arctic (Caroppo *et al.*, 2017), but only proliferates in surface waters during mixing events that resuspend shelf bottom waters, such as might occur during upwelling. These data showing that before upwelling *Alexandrium* is abundant on the shelf while after upwelling *Prorocentrum* increases in abundance raise concerns as both these dinoflagellates can produce toxins and their presence should be monitored for bioaccumulation and shellfish poisoning.

Cluster 3 includes most shelf transect stations that were sampled at the peak of the first upwelling event (2B), before the second upwelling event (2C), at the peak of the second upwelling event (2D), and just before the third upwelling event has occurred (4B). As stated above, the shallowest station from transect 2B is in cluster 2. Shelf stations from transect 2D and 4B are divided between clusters 3 and 4, where the coastal and shallowest stations are grouped with cluster 3 (influenced by first & second upwelling event), while the shelfbreak samples are grouped in cluster 4 (influenced by third upwelling event). Cluster 3 shows an increase in the relative abundance of the diatom community (Fig. 17), with increasing *Chaetoceros* and

Leptocylindrus reads accounting for most of this increase. *Leptocylindrus* is larger centric diatom previously documented to increase in abundance in response to nutrient additions to coastal water sampled from the Chukchi Sea (Mills *et al.*, 2018) and globally abundant (Malviya *et al.*, 2016) especially in upwelling systems (Ajani *et al.*, 2018). *Prorocentrum* relative abundance is continuously between 10-30 % of the phytoplankton community throughout these upwelling stations.

Despite indications of relaxation of the first upwelling event and the development and relaxation of the brief second upwelling event, it is apparent that complex flow persists during the time that transects 2B-D and 4B were sampled. The result of this complex flow is that even though relaxation was initiated twice, there was not a complete shift in phytoplankton community composition across the shelf between the first and third upwelling events. For example, it does not appear that the phytoplankton community reverts to that observed in cluster 1, which was sampled before the peak of the first upwelling event, between upwelling events 1 and 3 (i.e., cluster 3 is not similar to cluster 1). A possible explanation is that the time between these upwelling events is short enough that the community does not have time to respond to the upwelling relaxation. This would seem to indicate that if <2 days elapse between upwelling events the community will likely not revert back to pre-upwelling conditions. Suggesting that phytoplankton community structure does not change within 2 days, or nutrients have not been depleted yet, which would not be surprising given that phytoplankton blooms usually last at least several days in response to nutrient pulses (Lafond *et al.*, 2019). With the subsequent upwelling and nutrient replenishment, the primary phytoplankton that respond to upwelling (larger diatoms) can continuously dominate the phytoplankton community even with short relaxation periods of a few days. However, if relaxation would last longer, silicate will likely become limiting to larger

diatoms and the community structure will shift to other phytoplankton, including coccolithoforids, dinoflagellates, and other picoeukaryotes.

Cluster 4 spans the third upwelling event (6A, 5A, and 2E shelfbreak stations). Before sampling 6A, the 26 kg m^{-3} isopycnal rapidly shoals to almost 60 m and BSW (Temperature = 0-3 °C, Salinity = 32-33) (Yang and Bai, 2020) appears at ~80 m depth. This upwelling event differentiates between clusters 3 and 4. While *Prorocentrum* relative abundance stays similarly elevated between these clusters, the "Other Dinoflagellates" group increases in relative abundance but did not show a significant increase in any particular dinoflagellate genera. *Chaetoceros* and *Leptocylindrus* are still as relatively abundant in cluster 4 as they were in cluster 3, especially in the samples from transects 5 and 6. Cluster 5 groups the two most coastal stations in transect 2E. Cluster five shows a further increase in *Micromonas* and *Chaetoceros* while *Leptocylindrus* decreases in the relative phytoplankton community abundance. This large increase in relative abundance of phytoplankton groups other than dinoflagellates in cluster 5 likely is due to the third upwelling event receding and the onset of nutrient depletion where *Leptocylindrus* may be outcompeted or under nutrient stress, decreasing its growth rate.

This study examines the influence of three separate upwelling events on the Alaskan BS shelf. The shelfbreak jet is documented to transport warm waters originating from the Pacific (Pickart *et al.*, 2009) where the phytoplankton community of cluster 1 (transect 2A) almost exclusively consists of sequence reads for dinoflagellates and correlates with warm temperatures consistent with the shelfbreak jet (4-6°C) (Pickart *et al.*, 2013b). As upwelling is in full swing along the shelfbreak, the phytoplankton community shifts towards an increasing relative abundance of diatoms and picoeukaryotes. Upwelling events in the BS have previously led to increases in abundance of upper trophic levels (Falk-Petersen *et al.*, 2015), which would likely

be supported by the increase in diatoms seen here. While this study documented three distinct upwelling events, the time span between each event is ~1-2 days and did not allow for a complete relaxation between subsequent upwelling events. This may explain why there was not as large a difference in community composition between each event as there was between the first transect (before upwelling) and all subsequent transects. Further sampling and analysis that spans a full relaxation of upwelling is necessary to document how long it takes before the community reverts back to being influenced by the warm shelfbreak jet. As upwelling events along the Alaskan BS shelf are predicted to increase in strength and abundance due to climate warming (Schulze and Pickart, 2012), which will influence the strength and direction of the shelfbreak jet, the phytoplankton community in the region is likely to continue to be highly dynamic. These results indicate that the normal shelfbreak jet flow leads to increased *Alexandrium* abundances on the shelf, and upwelling (and reversed shelfbreak jet flow) causes an increased abundance of diatoms and picoeukaryotes, which likely fuel productivity and upper trophic levels. That said, the dinoflagellate *Prorocentrum* also increases in abundance in response to upwelling this area needs be monitored for toxin production regardless of upwelling state.

Beaufort Sea upwelling events in the fall are expected to continue to increase with Arctic warming (Schulze and Pickart, 2012). The impact of upwelling on the phytoplankton community in the Alaskan BS has been shown here to increase relative abundances of large, carbon export enhancing diatoms (*Chaetoceros, Leptocylindrus)*. The increase in upwelling abundance and strength here will then presumably drive increased primary productivity and upper trophic level activity on the Alaskan BS shelf. As seen in stations further off the shelfbreak in Figs. 15, 16, and 17, diatom abundances are higher during and after upwelling events. These results would

suggest that larger phytoplankton are being transported with Ekman drift off the shelf and into the BS during upwelling events, thereby likely exporting carbon into deeper waters capable of more long-term storage than if the population stayed on the shelf. The implication is that the BS will become a location of enhanced productivity and carbon export in the future, as Arctic warming continues to increase upwelling abundance and strength in this region.

CHAPTER V

CONCLUSIONS AND FUTURE DIRECTIONS

Established throughout this dissertation is the importance of the phytoplankton community structure to carbon export, higher trophic levels, and toxicity (Kiørboe *et al.*, 1998; He and McGillicuddy Jr., 2008; Falk-Petersen *et al.*, 2015; Lefebvre *et al.*, 2016; Krause *et al.*, 2019). Dynamics of the ocean are changing with a warming climate, while upwelling is predicted become stronger and more frequent (Iles *et al.*, 2012; Pickart *et al.*, 2013b), increased stratification from surface ocean warming makes it less likely for nutrient rich deep water to reach the surface (Durski and Allen, 2005; Capet *et al.*, 2008). Deep water contact with the shelf is necessary for elevated dissolved iron concentrations in upwelled water in the CCS (Bruland *et al.*, 2001). Thus, there are implications for phytoplankton community composition and carbon export based on where upwelling occurs in relation to shelf width in the CCS. However, as the ocean becomes more stratified, the dissolved iron concentrations in upwelled water may be low regardless of shelf width. As seen in Chapter II, smaller diatoms are accounting for a greater proportion of the community when upwelling waters have lower dissolved iron concentrations and where evidence of iron limitation was previously reported (Till *et al.*, 2019). Some phytoplankton are associated with enhanced carbon export (e.g., larger diatoms) while others (e.g., picoplankton) are mostly remineralized in the euphotic zone (Buesseler, 1998). In a more stratified ocean, upwelling events may not lead to as much carbon export based on the results reported here, however, further study is needed to determine if enhanced silicification of diatoms drives carbon export or just increased silica export in response to iron limited upwelling.

Phytoplankton community upwelling response is clearly variable and dependent on chemical composition of the upwelled water. Although macro and micronutrients were not measured in the BS project, we can hypothesize that the iron concentrations are higher, since we see larger diatoms increase in relative abundance. Also, the upwelling in the BS occurs over a shallow portion of the shelf and thus likely upwells waters in contact with the sediments. These diatoms are also seen offshore after upwelling, likely due to Ekman drift transporting them off the shelf and presumably increasing carbon export in the BS. Upwelling events in the BS are increasing (Schulze and Pickart, 2012) and are expected to continue to increase with a warming Arctic, however, further study on the chemical composition of upwelled water in the BS is merited to determine the relationship between the phytoplankton community composition and upwelled water. Arctic warming is also increasing sea-ice melt (Schulze and Pickart, 2012) thereby decreasing salinity in the surface ocean of the Arctic. This enhanced stratification of the water column, in addition to increasing surface temperature stratification, will likely change the chemical composition of upwelled water in the BS and could result in lower macro and micronutrients on the BS shelf. Although upwelling events will likely increase and enhance production in the BS, I hypothesize that BS upwelling could ultimately meet the same fate as I've hypothesized for CCS upwelling, with lower macro and micronutrients in upwelled water and subsequent lower production and carbon export in this region, in spite of enhance upwelling events.

Upwelling primary production accounts for up to 50% of all primary production on Earth (Loubere, 2000) and changes to upwelling dynamics, physical or chemical, will induce dramatic shifts to global primary production. In an era of rising atmospheric CO_2 levels, and resulting climate change, upwelling events and any changes to primary production need to be studied

further to anticipate broad ecological challenges and biogeochemical changes to nutrient cycling and carbon export. Upwelling is also a cause of CO_2 outgassing from the ocean, when nutrient rich (including high CO_2 concentrations) upwelled waters reach the surface ocean (Gray *et al.*, 2018). If increased stratification causes upwelling water masses with low iron levels in the CCS, we have to expect lower primary production and carbon export as smaller diatoms and other small picoplankton will likely be the primary response and associated with less carbon export (De La Rocha and Passow, 2007). CO_2 concentrations may, as a result, net outgas more into the atmosphere in CCS upwelling due to decreased primary production and carbon export. That said, it is possible that waters upwelling from shallower depths could result in the CO_2 concentrations of the upwelled waters also decreasing along with decreased nutrients in future upwelled waters. As a result of these competing factors, the impact on net CO_2 outgassing may be less clear, however decreased primary production and upper trophic level transport is expected.

Heat transport and Arctic amplification are decreasing sea-ice and leading to stronger and more frequent upwelling events in the BS (Schulze and Pickart, 2012; Marshall *et al.*, 2014; Marshall *et al.*, 2015). While this may increase primary production in the Alaskan BS, this dissertation has documented expansion of the temperate dinoflagellate *Alexandrium tamerense* further into the Arctic than previously seen. Bioaccumulation of neurotoxins have been documented along the Alaskan coast by the ACC (Lefebvre *et al.*, 2016) but our results suggest this may expand as the Arctic continues to warm. Especially in the summer when upwelling events are fewer, I predict that *Alexandrium* will continue to accumulate at least this far east in the Arctic and may be transported further east along the path of the warm shelfbreak jet. The *Prorocentrum* genus of dinoflagellates also have the ability to produce toxins (Bravo *et al.*, 2001) and increased in abundance as a result of Alaskan BS upwelling, as documented in

Chapter IV. The distribution, extent, and potential toxin production of this species also merits further attention in this area of the Arctic. The results from Chapters III and IV indicate that two competing forces are influencing these potential toxin producing dinoflagellate communities. The warm shelfbreak jet is introducing the *Alexandrium* population onto the shelf but the shelfbreak jet reversal and subsequent upwelling reduces that population to almost non-existent. While the upwelling increases the abundance of *Prorocentrum* on the shelf, the genera was not seen in any significant amount before upwelling. The phytoplankton community in this region should be monitored and further studied for toxin production from both genera, as the shelfbreak jet will likely continue to warm and upwelling strength is predicted to increase (Pickart *et al.*, 2013b).

Dinoflagellates are clearly an important part of the phytoplankton community, as determined by their relative abundance in chapter IV. However, dinoflagellates are documented to have orders of magnitude higher 18S gene counts than other phytoplankton (Guo *et al.*, 2016; Gong and Marchetti, 2019), which can lead to an over estimation of the dinoflagellate proportion of the relative community composition. I am heartened that the relative abundance of *A. tamarense* was determined to corroborate with absolute gene abundance and FlowCam imaging in Chapter III. As such, I suggest that future genetic work on the phytoplankton community be done in conjunction with imaging techniques, such as those performed by the following instruments, the FlowCam, Imagining Flow Cytobot, CytoSense, or any of their successors. These flow cytometry-related imagining platforms allow for imaging of the greater phytoplankton community and can correct scaling of the relative community composition based on 18S sequencing. Even though smaller phytoplankton, such as picoeukaryotes, are often difficult to image, they are less likely to have multiple gene copies due to their size and thus may

not have to be scaled accordingly. This corroboration should allow for more accurate analysis of phytoplankton community structure.

This study did not have the opportunity or capacity to examine the phytoplankton community after the 3 upwelling events in the BS. The first transect was collected a few days after a previous upwelling event (not shown), based on the mooring analysis the week before. This indicates that the first transect (2A; Chapters III and IV) was presumably collected after the phytoplankton community had equilibrated to normal shelfbreak jet directional flow, and upwelling cessation, since the community was dominated by the dinoflagellate *A. tamarense*, and the temperatures on the shelf were warmer than collected at any point throughout the subsequent sample collection period. I posit that the community composition can be predicted, based on the mooring and measurements of temperature, shelfbreak reversal, and my upwelling proxy, the 26 kg m^{-3} density isopycnal depth. My data suggests that the community will shift from an *Alexandrium* dominated community before an upwelling event to a community predominately consisting of the diatom genus *Leptocylindrus*, *Chaetoceros,* picoeukaryote *Micromonas*, and the dinoflagellate *Prorocentrum* during upwelling events. Although my data suggests that the community does not shift dramatically when upwelling events are less than ~1-2 days apart, I cannot say for certain how long it will take for the community to shift back once upwelling ceases and normal shelfbreak jet directional flow restarts.

Ocean surface currents clearly influence the phytoplankton community. Chapters III and IV show that the shelfbreak jet is influencing whether the phytoplankton community on the shelf is dominated by diatoms or dinoflagellates, depending on flow direction. In addition, Chapter II shows that diatom communities in CCS upwelling are also influenced by surface currents. Results from chapter II show that the diatom community, mostly larger diatoms like

Chaetoceros, are dispersed when an upwelling plume reaches the California Current (higher iron upwelling, transect 2). Additionally, the diatom community is seen to shift dramatically to smaller, more oligotrophic diatoms, after the path crosses the current. Presumably this is also a result of the current having transported the diatoms responding to upwelling southward with the current. The strong currents in the CCS are not the only surface dynamics influencing the diatom community in the region. Eddies, either anti-cyclone or cyclone, are known to transport nutrients and phytoplankton (Uchiyama *et al.*, 2017) and we see it disrupting the diatoms in an upwelling plume (lower iron upwelling, transect 9), likely transporting the diatom community with it as it moves through the area. These results indicate that surface currents, measured by remote sensing, are a useful tool for predicting likely dispersal of diatoms from upwelling to determine areas of enhanced carbon export.

The results reported and visualized throughout this dissertation show that the phytoplankton community response to upwelling is dependent not only on the upwelling itself, but on chemical composition of the upwelling water mass, and surface currents. Programs such as TARA OCEANS are examining the phytoplankton and other microbiology throughout the oceans but, as I have shown here, the fine scale dynamics of coastal oceans are dependent on seasons, climate change, and global warming. If we can scale the coverage of oceanic sampling programs to cover finer scale dynamics, such as upwelling fronts and eddies, we can determine phytoplankton response to some of the most productive events in the ocean, and further predict areas of enhanced or diminished carbon export and phytoplankton distribution throughout a changing ocean.

REFERENCES

Abdala, Z.M. (2020) Diatom Community Composition Shifts Driven by Coherent Cyclonic Mesoscale Eddies in the California Current System. In *Ocean & Earth Sciences*: Old Dominion University.

Ajani, P.A., Kahlke, T., Siboni, N., Carney, R., Murray, S.A., and Seymour, J.R. (2018) The Microbiome of the Cosmopolitan Diatom Leptocylindrus Reveals Significant Spatial and Temporal Variability. *Front Microbiol* **9**: 2758.

Altschul, S.F., Gish, W., Miller, W., Myers, E.W., and Lipman, D.J. (1990) Basic local alignment search tool. *J Mol Biol* **215**: 403-410.

Amante, C., and Eakins, B. (2009) ETOPO1 1 Arc-Minute Global Relief Model: procedures, data sources and analysis.

Anderson, D.M., Alpermann, T.J., Cembella, A.D., Collos, Y., Masseret, E., and Montresor, M. (2012) The globally distributed genus Alexandrium: multifaceted roles in marine ecosystems and impacts on human health. *Harmful Algae* **14**: 10-35.

Anderson, D.M., Keafer, B.A., Kleindinst, J.L., McGillicuddy, D.J., Martin, J.L., Norton, K. et al. (2014) Alexandrium fundyense cysts in the Gulf of Maine: Long-term time series of abundance and distribution, and linkages to past and future blooms. *Deep Sea Res Part II* **103**: 6-26.

Anderson, D.M., Fachon, E., Pickart, R.S., Lin, P., Fischer, A.D., Richlen, M.L. et al. (2021) Evidence for massive and recurrent toxic blooms of Alexandrium catenella in the Alaskan Arctic. *Proc Natl Acad Sci USA* **118**: e2107387118.

Armbrust, E.V. (2009) The life of diatoms in the world's oceans. *Nature* **459**: 185-192.

Ashjian, C.J., Braund, S.R., Campbell, R.G., George, J.C.C., Kruse, J., Maslowski, W. et al. (2010) Climate Variability, Oceanography, Bowhead Whale Distribution, and Inupiat Subsistence Whaling near Barrow, Alaska. *Arctic* **63**: 179-194.

Assmy, P., Henjes, J., Klaas, C., and Smetacek, V. (2007) Mechanisms determining species dominance in a phytoplankton bloom induced by the iron fertilization experiment EisenEx in the Southern Ocean. *Deep Sea Res Part I* **54**: 340-362.

Basu, S., and Mackey, K.R.M. (2018) Phytoplankton as Key Mediators of the Biological Carbon Pump: Their Responses to a Changing Climate. *Sustainability* **10**: 869.

Behrenfeld, M.J., O'Malley, R.T., Siegel, D.A., McClain, C.R., Sarmiento, J.L., Feldman, G.C. et al. (2006) Climate-driven trends in contemporary ocean productivity. *Nature* **444**: 752-755.

Benoiston, A.S., Ibarbalz, F.M., Bittner, L., Guidi, L., Jahn, O., Dutkiewicz, S., and Bowler, C. (2017) The evolution of diatoms and their biogeochemical functions. *Philos Trans R Soc Lond B Biol Sci* **372**: 20160397.

Biassoni, R., and Raso, A. (2020) *Quantitative real-time PCR : methods and protocols*. New York, USA: Humana.

Biller, D.V., Coale, T.H., Till, R.C., Smith, G.J., and Bruland, K.W. (2013) Coastal iron and nitrate distributions during the spring and summer upwelling season in the central California Current upwelling regime. *Cont Shelf Res* **66**: 58-72.

Bravo, I., Fernández, M.L., Ramilo, I., and Martínez, A. (2001) Toxin composition of the toxic dinoflagellate Prorocentrum lima isolated from different locations along the Galician coast (NW Spain). *Toxicon* **39**: 1537-1545.

Bravo, L., Ramos, M., Astudillo, O., Dewitte, B., and Goubanova, K. (2016) Seasonal variability of the Ekman transport and pumping in the upwelling system off central-northern Chile (∼ 30° S) based on a high-resolution atmospheric regional model (WRF). *Ocean Sci* **12**: 1049-1065.

Bray, J.R., and Curtis, J.T. (1957) An Ordination of the Upland Forest Communities of Southern Wisconsin. *Ecol Monogr* **27**: 325-349.

Brosnahan, M.L., Ralston, D.K., Fischer, A.D., Solow, A.R., and Anderson, D.M. (2017) Bloom termination of the toxic dinoflagellate Alexandrium catenella: Vertical migration behavior, sediment infiltration, and benthic cyst yield. *Limnol Oceanogr* **62**: 2829-2849.

Bruland, K.W., Rue, E.L., and Smith, G.J. (2001) Iron and macronutrients in California coastal upwelling regimes: Implications for diatom blooms. *Limnol Oceanogr* **46**: 1661-1674.

Bruland, K.W., Rue, E.L., Smith, G.J., and DiTullio, G.R. (2005) Iron, macronutrients and diatom blooms in the Peru upwelling regime: Brown and blue waters of Peru. *Mar Chem* **93**: 81-103.

Brzezinski, M., Dickson, M.-L., Nelson, D., and Sambrotto, R. (2003) Ratios of Si, C and N Uptake by microplankton in the Southern Ocean. *Deep Sea Res Part II* **50**: 619-633.

Brzezinski, M.A., Krause, J.W., Bundy, R.M., Barbeau, K.A., Franks, P., Goericke, R. et al. (2015) Enhanced silica ballasting from iron stress sustains carbon export in a frontal zone within the California Current. *J Geophys Res: Oceans* **120**: 4654-4669.

Buesseler, K.O. (1998) The decoupling of production and particulate export in the surface ocean. *Global Biogeochem Cycles* **12**: 297-310.

Bustin, S.A., Benes, V., Garson, J.A., Hellemans, J., Huggett, J., Kubista, M. et al. (2009) The MIQE Guidelines: Minimum Information for Publication of Quantitative Real-Time PCR Experiments. *Clin Chem* **55**: 611-622.

Callahan, B.J., McMurdie, P.J., Rosen, M.J., Han, A.W., Johnson, A.J.A., and Holmes, S.P. (2016) DADA2: High-resolution sample inference from Illumina amplicon data. *Nat Methods* **13**: 581-583.

Capet, X., McWilliams, J.C., Molemaker, M.J., and Shchepetkin, A.F. (2008) Mesoscale to Submesoscale Transition in the California Current System. Part II: Frontal Processes. *J Phys Oceanogr* **38**: 44-64.

Caroppo, C., Pagliara, P., Azzaro, F., Miserocchi, S., and Azzaro, M. (2017) Late Summer Phytoplankton Blooms in the Changing Polar Environment of the Kongsfjorden (Svalbard, Arctic). *Cryptogam Algol* **38**: 53 - 72.

Chappell, P., Whitney, L., Haddock, T., Menden-Deuer, S., Roy, E., Wells, M., and Jenkins, B. (2013) Thalassiosira spp. community composition shifts in response to chemical and physical forcing in the northeast Pacific Ocean. *Front Microbiol* **4**: 273.

Chappell, P.D., Armbrust, E.V., Barbeau, K.A., Bundy, R.M., Moffett, J.W., Vedamati, J., and Jenkins, B.D. (2019) Patterns of diatom diversity correlate with dissolved trace metal concentrations and longitudinal position in the northeast Pacific coastal-offshore transition zone. *Mar Ecol Prog Ser* **609**: 69-86.

Chase, Z., Hales, B., Cowles, T., Schwartz, R., and van Geen, A. (2005) Distribution and variability of iron input to Oregon coastal waters during the upwelling season. *J Geophys Res: Oceans* **110**: C10.

Clarke, K.R., and Ainsworth, M. (1993) A Method Of Linking Multivariate Community Structure To Environmental Variables. *Mar Ecol Prog Ser* **92**: 205-219.

Cupp, E.E. (1943) Marine plankton diatoms of the west coast of North America. *Bull Scripps Inst Oceanogr* **5**: 1-238.

Cushing, D.H. (1971) Upwelling and the Production of Fish. *Adv Mar Biol* **9**: 255-334.

Cusick, K.D., and Sayler, G.S. (2013) An overview on the marine neurotoxin, saxitoxin: genetics, molecular targets, methods of detection and ecological functions. *Mar Drugs* **11**: 991-1018.

Davis, K.A., Banas, N.S., Giddings, S.N., Siedlecki, S.A., MacCready, P., Lessard, E.J. et al. (2014) Estuary-enhanced upwelling of marine nutrients fuels coastal productivity in the U.S. Pacific Northwest. *J Geophys Res: Oceans* **119**: 8778-8799.

De La Rocha, C.L., and Passow, U. (2007) Factors influencing the sinking of POC and the efficiency of the biological carbon pump. *Deep Sea Res Part II* **54**: 639-658.

Degerlund, M., and Eilertsen, H.C. (2010) Main Species Characteristics of Phytoplankton Spring Blooms in NE Atlantic and Arctic Waters (68-80° N). *Estuaries Coasts* **33**: 242-269.

Dufois, F., Hardman-Mountford, N.J., Greenwood, J., Richardson, A.J., Feng, M., and Matear, R.J. (2016) Anticyclonic eddies are more productive than cyclonic eddies in subtropical gyres because of winter mixing. *Sci Adv* **2**: e1600282.

Durski, S.M., and Allen, J.S. (2005) Finite-Amplitude Evolution of Instabilities Associated with the Coastal Upwelling Front. *J Phys Oceanogr* **35**: 1606-1628.

Falk-Petersen, S., Pavlov, V., Berge, J., Cottier, F., Kovacs, K.M., and Lydersen, C. (2015) At the rainbow's end: high productivity fueled by winter upwelling along an Arctic shelf. *Polar Biol* **38**: 5-11.

Fernandes, L., and Frassão-Santos, E. (2011) Mucilaginous species of Thalassiosira Cleve emend. Hasle (Diatomeae) in South Brazilian waters. *Acta Botanica Brasilica* **25**: 31-42.

Foukal, N.P., Pickart, R.S., Moore, G.W.K., and Lin, P. (2019) Shelfbreak Downwelling in the Alaskan Beaufort Sea. *J Geophys Res: Oceans* **124**: 7201-7225.

Ganachaud, A., Vega, A., Rodier, M., Dupouy, C., Maes, C., Marchesiello, P. et al. (2010) Observed impact of upwelling events on water properties and biological activity off the southwest coast of New Caledonia. *Mar Pollut Bull* **61**: 449-464.

Gerringa, L.J.A., Alderkamp, A.-C., Laan, P., Thuróczy, C.-E., De Baar, H.J.W., Mills, M.M. et al. (2012) Iron from melting glaciers fuels the phytoplankton blooms in Amundsen Sea (Southern Ocean): Iron biogeochemistry. *Deep Sea Res Part II* **71-76**: 16-31.

Gong, W., and Marchetti, A. (2019) Estimation of 18S Gene Copy Number in Marine Eukaryotic Plankton Using a Next-Generation Sequencing Approach. *Front Mar Sci* **6**: 219.

González-Dávila, M., Santana Casiano, J.M., and Machín, F. (2017) Changes in the partial pressure of carbon dioxide in the Mauritanian–Cap Vert upwelling region between 2005 and 2012. *Biogeosci* **14**: 3859-3871.

Gordon, L.I., J.C. Jennings, Jr., A.A. Ross, and J.M. Krest (1993) A suggested protocol for continuous flow automated analysis of seawater nutrients (phosphate, nitrate, nitrite and silicic acid) in the WOCE Hydrographic Program and the Joint Global Ocean Fluxes Study. *WOCE Hydrogr Prog Office, Method Manual* **WHPO**: 1-52.

Gray, W.R., Rae, J.W.B., Wills, R.C.J., Shevenell, A.E., Taylor, B., Burke, A. et al. (2018) Deglacial upwelling, productivity and CO2 outgassing in the North Pacific Ocean. *Nat Geosci* **11**: 340-344.

Guinder, V.A., Molinero, J.C., Popovich, C.A., Marcovecchio, J.E., and Sommer, U. (2012) Dominance of the planktonic diatom Thalassiosira minima in recent summers in the Bahía Blanca Estuary, Argentina. *J Plankton Res* **34**: 995-1000.

Guo, L., Sui, Z., and Liu, Y. (2016) Quantitative analysis of dinoflagellates and diatoms community via Miseq sequencing of actin gene and v9 region of 18S rDNA. *Sci Rep* **6**: 34709.

Hasle, G.R., and Syvertsen, E.E. (1997) Chapter 2 - Marine Diatoms. In *Identifying Marine Phytoplankton*. Tomas, C.R. (ed). San Diego: Academic Press, pp. 5-385.

He, R., and McGillicuddy Jr., D.J. (2008) Historic 2005 toxic bloom of Alexandrium fundyense in the west Gulf of Maine: 1. In situ observations of coastal hydrography and circulation. *J Geophys Res: Oceans* **113**: C7.

Hendy, I.L. (2015) Ironing out carbon export to the deep ocean. *Proc Natl Acad Sci* **112**: 306-307.

Hersbach, H., Rosnay, P., Schepers, D., Simmons, A., Soci, C., Abdalla, S. et al. (2018) Operational global reanalysis : progress, future directions and synergies with NWP including updates on the ERA5 production status. In *ECMWF*. Reading, UK.

Hoffmann, L.J., Peeken, I., and Lochte, K. (2008) Iron, silicate, and light co-limitation of three Southern Ocean diatom species. *Polar Biol* **31**: 1067-1080.

Holland, M.M., and Bitz, C.M. (2003) Polar amplification of climate change in coupled models. *Clim Dyn* **21**: 221-232.

Hoppenrath, M., Beszteri, B., Drebes, G., Halliger, H., Van Beusekom, J.E.E., Janisch, S., and Wiltshire, K.H. (2007) Thalassiosira species (Bacillariophyceae, Thalassiosirales) in the North Sea at Helgoland (German Bight) and Sylt (North Frisian Wadden Sea) – a first approach to assessing diversity. *Eur J Phycol* **42**: 271-288.

Hosoi-Tanabe, S., and Sako, Y. (2005) Species-specific detection and quantification of toxic marine dinoflagellates Alexandrium tamarense and A. catenella by Real-time PCR assay. *Mar Biotechnol* **7**: 506-514.

Hutchins, D.A., and Bruland, K.W. (1998) Iron-limited diatom growth and Si:N uptake ratios in a coastal upwelling regime. *Nature* **393**: 561-564.

Hyun, B., Choi, K.-H., Jang, P.-G., Jang, M.-C., Lee, W.-J., Moon, C.-H., and Shin, K. (2014) Effects of Increased CO 2 and Temperature on the Growth of Four Diatom Species (Chaetoceros debilis, Chaetoceros didymus, Skeletonema costatum and Thalassiosira nordenskioeldii) in Laboratory Experiments. *Int J Environ Sci* **23**: 1003-1012.

Iles, A.C., Gouhier, T.C., Menge, B.A., Stewart, J.S., Haupt, A.J., and Lynch, M.C. (2012) Climate-driven trends and ecological implications of event-scale upwelling in the California Current System. *Global Change Biol* **18**: 783-796.

Jackson, T., Bouman, H.A., Sathyendranath, S., and Devred, E. (2011) Regional-scale changes in diatom distribution in the Humboldt upwelling system as revealed by remote sensing: implications for fisheries. *ICES J Mar Sci* **68**: 729-736.

Jacox, M.G., Edwards, C.A., Hazen, E.L., and Bograd, S.J. (2018) Coastal Upwelling Revisited: Ekman, Bakun, and Improved Upwelling Indices for the U.S. West Coast. *J Geophys Res: Oceans* **123**: 7332-7350.

John, U., Litaker, R.W., Montresor, M., Murray, S., Brosnahan, M.L., and Anderson, D.M. (2014) Formal revision of the Alexandrium tamarense species complex (Dinophyceae)

taxonomy: the introduction of five species with emphasis on molecular-based (rDNA) classification. *Protist* **165**: 779-804.

Johnson, K.S., Chavez, F.P., and Friederich, G.E. (1999) Continental-shelf sediment as a primary source of iron for coastal phytoplankton. *Nature* **398**: 697-700.

Joon Sang Park, S.W.J., Jin Hwan Le (2009) A Study on the Fine Structure of the Marine Diatoms of Korean Coastal Waters - Genus Thalassiosira 4. *Algae* **24**: 67-77.

Kahru, M., Jacox, M.G., and Ohman, M.D. (2018) CCE1: Decrease in the frequency of oceanic fronts and surface chlorophyll concentration in the California Current System during the 2014–2016 northeast Pacific warm anomalies. *Deep Sea Res Part I* **140**: 4-13.

Kim, K.Y., Hamlington, B.D., Na, H., and Kim, J. (2016) Mechanism of seasonal Arctic sea ice evolution and Arctic amplification. *Cryosphere* **10**: 2191-2202.

Kiørboe, T., Tiselius, P., Mitchell-Innes, B., Hansen, J.L.S., Visser, A.W., and Mari, X. (1998) Intensive aggregate formation with low vertical flux during an upwelling-induced diatom bloom. *Limnol Oceanogr* **43**: 104-116.

Korb, R.E., Whitehouse, M.J., Ward, P., Gordon, M., Venables, H.J., and Poulton, A.J. (2012) Regional and seasonal differences in microplankton biomass, productivity, and structure across the Scotia Sea: Implications for the export of biogenic carbon. *Deep Sea Res Part II* **59-60**: 67-77.

Krause, J.W., Schulz, I.K., Rowe, K.A., Dobbins, W., Winding, M.H.S., Sejr, M.K. et al. (2019) Silicic acid limitation drives bloom termination and potential carbon sequestration in an Arctic bloom. *Sci Rep* **9**: 8149.

Krause, J.W., Brzezinski, M.A., Largier, J.L., McNair, H.M., Maniscalco, M., Bidle, K.D. et al. (2020) The interaction of physical and biological factors drives phytoplankton spatial distribution in the northern California Current. *Limnol Oceanogr* **65**: 1974-1989.

Lafond, A., Leblanc, K., Quéguiner, B., Moriceau, B., Leynaert, A., Cornet, V. et al. (2019) Late spring bloom development of pelagic diatoms in Baffin Bay. *Elem Sci Anth* **7**: 44.

Lampe, R.H., Mann, E.L., Cohen, N.R., Till, C.P., Thamatrakoln, K., Brzezinski, M.A. et al. (2018) Different iron storage strategies among bloom-forming diatoms. *Proc Natl Acad Sci USA* **115**: E12275-E12284.

Leblanc, K., Quéguiner, B., Diaz, F., Cornet, V., Michel-Rodriguez, M., Durrieu de Madron, X. et al. (2018) Nanoplanktonic diatoms are globally overlooked but play a role in spring blooms and carbon export. *Nat Commun* **9**: 953.

Lefebvre, K.A., Quakenbush, L., Frame, E., Huntington, K.B., Sheffield, G., Stimmelmayr, R. et al. (2016) Prevalence of algal toxins in Alaskan marine mammals foraging in a changing arctic and subarctic environment. *Harmful Algae* **55**: 13-24.

Lelong, A., Hégaret, H., Soudant, P., and Bates, S. (2012) Pseudo-nitzschia (Bacillariophyceae) Species, Domoic Acid and Amnesic Shellfish Poisoning: Revisiting Previous Paradigms. *Phycologia* **51**: 168-216.

Li, W., and Godzik, A. (2006) Cd-hit: a fast program for clustering and comparing large sets of protein or nucleotide sequences. *Bioinformatics* **22**: 1658-1659.

Lilly, E.L., Halanych, K.M., and Anderson, D.M. (2007) Species boundaries and global biogeography of the Alexandrium tamarense complex (Dinophyceae)1. *J Phycol* **43**: 1329-1338.

Lin, P., Pickart, R.S., Moore, G.W.K., Spall, M.A., and Hu, J. (2019) Characteristics and dynamics of wind-driven upwelling in the Alaskan Beaufort Sea based on six years of mooring data. *Deep Sea Res Part II* **162**: 79-92.

Lin, P., Pickart, R.S., Stafford, K.M., Moore, G.W.K., Torres, D.J., Bahr, F., and Hu, J. (2016) Seasonal variation of the Beaufort shelfbreak jet and its relationship to Arctic cetacean occurrence. *J Geophys Res: Oceans* **121**: 8434-8454.

Lin, S. (2011) Genomic understanding of dinoflagellates. *Res Microbiol* **162**: 551-569.

Loubere, P. (2000) Marine control of biological production in the eastern equatorial Pacific Ocean. *Nature* **406**: 497-500.

Malviya, S., Scalco, E., Audic, S., Vincent, F., Veluchamy, A., Poulain, J. et al. (2016) Insights into global diatom distribution and diversity in the world's ocean. *Proc Natl Acad Sci USA* **113**: E1516-E1525.

Manabe, S., and Stouffer, R.J. (1980) Sensitivity of a global climate model to an increase of CO2 concentration in the atmosphere. *J Geophys Res: Oceans* **85**: 5529-5554.

Marañón, E. (2015) Cell Size as a Key Determinant of Phytoplankton Metabolism and Community Structure. *Annu Rev Mar Science* **7**: 241-264.

Marchetti, A., and Maldonado, M.T. (2016) Iron. In *The Physiology of Microalgae*. Borowitzka, M.A., Beardall, J., and Raven, J.A. (eds). Cham: Springer, pp. 233-279.

Marret, F., and Zonneveld, K.A.F. (2003) Atlas of modern organic-walled dinoflagellate cyst distribution. *Rev Palaeobot Palynol* **125**: 1-200.

Marshall, J., Scott, J.R., Armour, K.C., Campin, J.M., Kelley, M., and Romanou, A. (2015) The ocean's role in the transient response of climate to abrupt greenhouse gas forcing. *Clim Dyn* **44**: 2287-2299.

Marshall, J., Armour, K.C., Scott, J.R., Kostov, Y., Hausmann, U., Ferreira, D. et al. (2014) The ocean's role in polar climate change: asymmetric Arctic and Antarctic responses to greenhouse gas and ozone forcing. *Philos Trans R Soc London, Ser A* **372**: 20130040.

McGillicuddy, D.J., Brosnahan, M.L., Couture, D.A., He, R., Keafer, B.A., Manning, J.P. et al. (2014) A red tide of Alexandrium fundyense in the Gulf of Maine. *Deep Sea Res Part II* **103**: 174-184.

McMinn, A., Martin, A., and Ryan, K. (2010) Phytoplankton and sea ice algal biomass and physiology during the transition between winter and spring (McMurdo Sound, Antarctica). *Polar Biol* **33**: 1547-1556.

McNair, H.M., Brzezinski, M.A., Till, C.P., and Krause, J.W. (2018) Taxon-specific contributions to silica production in natural diatom assemblages. *Limnol Oceanogr* **63**: 1056-1075.

Meakin, N.G., and Wyman, M. (2011) Rapid shifts in picoeukaryote community structure in response to ocean acidification. *ISME J* **5**: 1397-1405.

Mena, C., Reglero, P., Hidalgo, M., Sintes, E., Santiago, R., Martín, M. et al. (2019) Phytoplankton Community Structure Is Driven by Stratification in the Oligotrophic Mediterranean Sea. *Front Microbiol* **10**: 1698.

Mills, M.M., Brown, Z.W., Laney, S.R., Ortega-Retuerta, E., Lowry, K.E., van Dijken, G.L., and Arrigo, K.R. (2018) Nitrogen Limitation of the Summer Phytoplankton and Heterotrophic Prokaryote Communities in the Chukchi Sea. *Front Mar Sci* **5**: 362.

Moore, J.K., Doney, S.C., and Lindsay, K. (2004) Upper ocean ecosystem dynamics and iron cycling in a global three-dimensional model. *Global Biogeochem Cycles* **18**: GB4028.

Nikolopoulos, A., Pickart, R.S., Fratantoni, P.S., Shimada, K., Torres, D.J., and Jones, E.P. (2009) The western Arctic boundary current at 152°W: Structure, variability, and transport. *Deep Sea Res Part II* **56**: 1164-1181.

Nishikawa, T., Tarutani, K., and Yamamoto, T. (2009) Nitrate and phosphate uptake kinetics of the harmful diatom Eucampia zodiacus Ehrenberg, a causative organism in the bleaching of aquacultured Porphyra thalli. *Harmful Algae* **8**: 513-517.

Oliver, H., Zhang, W.G., Smith Jr., W.O., Alatalo, P., Chappell, P.D., Hirzel, A.J. et al. (2021) Diatom Hotspots Driven by Western Boundary Current Instability. *Geophys Res Lett* **48**: e2020GL091943.

Pickart, R.S., Spall, M.A., and Mathis, J.T. (2013a) Dynamics of upwelling in the Alaskan Beaufort Sea and associated shelf–basin fluxes. *Deep Sea Res Part I* **76**: 35-51.

Pickart, R.S., Moore, G.W.K., Torres, D.J., Fratantoni, P.S., Goldsmith, R.A., and Yang, J. (2009) Upwelling on the continental slope of the Alaskan Beaufort Sea: Storms, ice, and oceanographic response. *J Geophys Res: Oceans* **114**: C1.

Pickart, R.S., Spall, M.A., Moore, G.W.K., Weingartner, T.J., Woodgate, R.A., Aagaard, K., and Shimada, K. (2011) Upwelling in the Alaskan Beaufort Sea: Atmospheric forcing and local versus non-local response. *Prog Oceanogr* **88**: 78-100.

Pickart, R.S., Schulze, L.M., Moore, G.W.K., Charette, M.A., Arrigo, K.R., van Dijken, G., and Danielson, S.L. (2013b) Long-term trends of upwelling and impacts on primary productivity in the Alaskan Beaufort Sea. *Deep Sea Res Part I* **79**: 106-121.

Pitcher, G.C., Figueiras, F.G., Hickey, B.M., and Moita, M.T. (2010) The physical oceanography of upwelling systems and the development of harmful algal blooms. *Prog Oceanogr* **85**: 5-32.

Ragueneau, O., Tréguer, P., Leynaert, A., Anderson, R.F., Brzezinski, M.A., DeMaster, D.J. et al. (2000) A review of the Si cycle in the modern ocean: recent progress and missing gaps in the application of biogenic opal as a paleoproductivity proxy. *Global Planet Change* **26**: 317-365.

Ribeiro, S., Berge, T., Lundholm, N., Andersen, T.J., Abrantes, F., and Ellegaard, M. (2011) Phytoplankton growth after a century of dormancy illuminates past resilience to catastrophic darkness. *Nat Commun* **2**: 311.

Rossi, V., López, C., Sudre, J., Hernández-García, E., and Garçon, V. (2008) Comparative study of mixing and biological activity of the Benguela and Canary upwelling systems. *Geophys Res Lett* **35**: L11602.

Round, F.E., Crawford, R.M., and Mann, D.G. (1990) *Diatoms: biology and morphology of the genera*. Cambridge, UK: Cambridge University Press.

Rykaczewski, R.R., and Dunne, J.P. (2010) Enhanced nutrient supply to the California Current Ecosystem with global warming and increased stratification in an earth system model. *Geophys Res Lett* **37**: 21.

Schulze, L.M., and Pickart, R.S. (2012) Seasonal variation of upwelling in the Alaskan Beaufort Sea: Impact of sea ice cover. *J Geophys Res: Oceans* **117**: C06022.

Smayda, T.J., and Reynolds, C.S. (2003) Strategies of marine dinoflagellate survival and some rules of assembly. *J Sea Res* **49**: 95-106.

Smayda, T.J., and Trainer, V.L. (2010) Dinoflagellate blooms in upwelling systems: Seeding, variability, and contrasts with diatom bloom behaviour. *Prog Oceanogr* **85**: 92-107.

Smetacek, V. (1999) Diatoms and the Ocean Carbon Cycle. *Protist* **150**: 25-32.

Spall, M.A. (2004) Boundary Currents and Watermass Transformation in Marginal Seas. *J Phys Oceanogr* **34**: 1197-1213.

Spilling, K., Olli, K., Lehtoranta, J., Kremp, A., Tedesco, L., Tamelander, T. et al. (2018) Shifting Diatom—Dinoflagellate Dominance During Spring Bloom in the Baltic Sea and its Potential Effects on Biogeochemical Cycling. *Front Mar Sci* **5**: 327.

Steele, M., Morison, J., Ermold, W., Rigor, I., Ortmeyer, M., and Shimada, K. (2004) Circulation of summer Pacific halocline water in the Arctic Ocean. *J Geophys Res: Oceans* **109**: C2.

Stoeck, T., Bass, D., Nebel, M., Christen, R., Jones, M., Breiner, H.-W., and Richards, T.A. (2010) Multiple marker parallel tag environmental DNA sequencing reveals a highly complex eukaryotic community in marine anoxic water. *Mol Ecol* **19**: 21-31.

Sutak, R., Camadro, J.-M., and Lesuisse, E. (2020) Iron Uptake Mechanisms in Marine Phytoplankton. *Front Microbiol* **11**: 2831.

Tarazona-Janampa, U.I., Cembella, A.D., Pelayo-Zárate, M.C., Pajares, S., Márquez-Valdelamar, L.M., Okolodkov, Y.B. et al. (2020) Associated Bacteria and Their Effects on Growth and Toxigenicity of the Dinoflagellate Prorocentrum lima Species Complex From Epibenthic Substrates Along Mexican Coasts. *Front Mar Sci* **7**: 569.

Tenore, K.R., Alonso-Noval, M., Alvarez-Ossorio, M., Atkinson, L.P., Cabanas, J.M., Cal, R.M. et al. (1995) Fisheries and oceanography off Galicia, NW Spain: Mesoscale spatial and temporal changes in physical processes and resultant patterns of biological productivity. *J Geophys Res: Oceans* **100**: 10943-10966.

Till, C.P., Solomon, J.R., Cohen, N.R., Lampe, R.H., Marchetti, A., Coale, T.H., and Bruland, K.W. (2019) The iron limitation mosaic in the California Current System: Factors governing Fe availability in the shelf/near-shelf region. *Limnol Oceanogr* **64**: 109-123.

Torres, R., Pantoja, S., Harada, N., González, H.E., Daneri, G., Frangopulos, M. et al. (2011) Air-sea CO2 fluxes along the coast of Chile: From CO2 outgassing in central northern upwelling waters to CO2 uptake in southern Patagonian fjords. *J Geophys Res: Oceans* **116**: C9.

Uchiyama, Y., Suzue, Y., and Yamazaki, H. (2017) Eddy-driven nutrient transport and associated upper-ocean primary production along the Kuroshio. *J Geophys Res: Oceans* **122**: 5046-5062.

van der Linden, E.C., Le Bars, D., Bintanja, R., and Hazeleger, W. (2019) Oceanic heat transport into the Arctic under high and low CO2 forcing. *Clim Dyn* **53**: 4763-4780.

von Appen, W.-J., and Pickart, R.S. (2012) Two Configurations of the Western Arctic Shelfbreak Current in Summer. *J Phys Oceanogr* **42**: 329-351.

Wall, D. (1971) Biological Problems concerning Fossilizable Dinoflagellates. *Proc Ann Meeting, Amer Assoc Stratigr Palynol* **2**: 1-15.

Wang, D.-Z. (2008) Neurotoxins from Marine Dinoflagellates: A Brief Review. *Mar Drugs* **6**: 349-371.

Weimin, H., Jing, X., Jari, S., and Jun, W. (2010) Polyketides from Marine Dinoflagellates of the Genus Prorocentrum, Biosynthetic Origin and Bioactivity of Their Okadaic Acid Analogues. *Mini-Rev Med Chem* **10**: 51-61.

Weise, A., Levasseur, M., Saucier, F., Senneville, S., Bonneau, E., Roy, S. et al. (2002) The link between precipitation, river runoff, and blooms of the toxic dinoflagellate Alexandrium tamarense in the St. Lawrence. *Can J Fish Aquat Sci* **59**: 464-473.

Whitney, L.P., and Lomas, M.W. (2016) Growth on ATP Elicits a P-Stress Response in the Picoeukaryote Micromonas pusilla. *PLoS One* **11**: e0155158-e0155158.

Woodgate, R.A. (2018) Increases in the Pacific inflow to the Arctic from 1990 to 2015, and insights into seasonal trends and driving mechanisms from year-round Bering Strait mooring data. *Prog Oceanogr* **160**: 124-154.

Woodgate, R.A., Weingartner, T., and Lindsay, R. (2010) The 2007 Bering Strait oceanic heat flux and anomalous Arctic sea-ice retreat. *Geophys Res Lett* **37**: 1.

Wyatt, T., and Jenkinson, I.R. (1997) Notes on Alexandrium population dynamics. *J Plankton Res* **19**: 551-575.

Xiu, P., Chai, F., Curchitser, E.N., and Castruccio, F.S. (2018) Future changes in coastal upwelling ecosystems with global warming: The case of the California Current System. *Sci Rep* **8**: 2866.

Yang, Y., and Bai, X. (2020) Summer Changes in Water Mass Characteristics and Vertical Thermohaline Structure in the Eastern Chukchi Sea, 1974–2017. *Water* **12**: 1434.

Zimmermann, J., Jahn, R., and Gemeinholzer, B. (2011) Barcoding diatoms: evaluation of the V4 subregion on the 18S rRNA gene, including new primers and protocols. *Org Divers Evol* **11**: 173-192.

APPENDICES

A. SUPPLEMENTAL INFORMATION FOR CHAPTER II

Supplemental Table 1. Relative ratios of diatom genera for each sample collected in the CCS. Each number is a proportion of a whole.

Station	Other	Rhizos-olenia	Lauderia annulata	Thalassiosira eccentrica	Thalassiosira minicosmica	Chaetoceros constrictus	Navicula sp.
T2S1	0.203795	0.006255	6.98E-05	0.002052	0.001382	0.022911	0.021919
T2S2	0.169153	0.004321	0.000117	0.008893	0.002703	0.012747	0.018437
T2S3	0.08292	0.001897	0	0.001436	0.000433	0.008385	0.004051
T2S4	0.072979	0.006027	0	0.004122	0.002293	0.007856	0.002972
T2S5	0.090293	0.017552	0	0.0035	0.01103	0.006604	0.004915
T2S6	0.08722	0.005418	0	0.00415	0.004171	0.009844	0.005479
T2S7	0.10434	0.001852	0	0.003632	0.003414	0.018621	0.001986
T2S8	0.268391	0.007689	0.000165	0.02296	0.015908	0.055685	0.00908
T2S9	0.148916	0.008533	0	0.005098	0.014509	0.002796	0.004002
T2S10	0.12795	0.003555	0	0.006122	0.020058	0.005896	0.00299
T2S11	0.115813	0.001996	0	0.003478	0.00414	0.012251	0.0027
T2S12	0.142201	0.027933	0	0.001374	0.014942	0.008074	0.000888
T2S13	0.182563	0.006005	0	0.001804	0.019522	0.004478	0.000984
T2S14	0.298121	0.011377	0	0.002066	0.041212	0.000525	0
T2S15	0.093274	0.00508	0	0	0.024389	0	0.00052
T2S16	0.10292	0.004067	0	0.000426	0.012522	0.000106	0.001342
T2S17	0.092779	0.002041	0.000233	0.00033	0.011955	0	0.000272
T2S18	0.143826	0.007984	0	0.001772	0.00336	0.004868	0.001079
T2S19	0.132212	0.006528	0	0.000653	0.008586	0.000854	0.001105
T2S20	0.133254	0.009282	0	0	0.002321	0.000738	0
T2S21	0.167358	0.009101	0	0.007687	0.002688	0.006932	0.000377
T2S22	0.144598	0.012289	0	0.003072	0.004813	0.00768	0.004352
T2S23	0.125726	0.013087	0.000147	0	0.003088	0	0
T9S1	0.118614	0	0.000577	0.035371	0.00385	0.000692	0.009546
T9S2	0.09109	0	4.97E-05	0.009981	0	0	0.002802
T9S3	0.073308	0	0.000164	0.011904	0	0	0.004048
T9S4	0.109634	0	0.016156	0.022392	0.000465	0.000319	0.020836
T9S5	0.321504	0	0.084584	0.018592	0	0.000412	0.014483
T9S6	0.292737	0	0.092783	0.014555	0	0.000311	0.014389
T9S7	0.130942	0	0.021465	0.01808	0	0.000324	0.010378
T9S8	0.101023	0	0.001385	0.007918	0.002379	0.001385	0.009126
T9S9	0.204378	0.015182	0.010059	0.008165	0.00416	0.013753	0.054393
T9S10	0.154171	0.007856	0.002699	0.003251	0.002824	0.018952	0.011961
T9S11	0.163361	0.009935	0.005457	0.004607	0.003063	0.018519	0.017541
T9S12	0.207459	0.005813	0.014651	0.002373	0.000786	0.010558	0.04035
T9S13	0.156908	0.001824	0.006302	0.002282	0.001216	0.009018	0.013087
T9S14	0.235243	0.004536	0.009287	0.006206	0.004965	0.00095	0.012489
T9S15	0.255553	0.003331	0.010913	0.007656	0.001656	0.000736	0.01625
T9S16	0.099098	0.001853	0.004137	0.000692	0	0.013219	0.017043

Supplemental Table 1. Cont.

Station	Skeletonema costatum	Chaetocer-os neogracile	Asteromp-halus sp.	Corethron inerme like	Eucampia zodiacus	Actinocyclus sp.	Fragilariop-sis sublineata like
T2S1	0.003853	0	0.000237	0.004831	0.371946	0.001424	0.001047
T2S2	0.009494	0.002753	0.001034	0.013131	0.022408	0.007375	0.004739
T2S3	0.001273	0	0.000122	0.004714	0.065892	0.000989	0.001124
T2S4	0.004777	0.000427	0.000899	0.024085	0.006667	0.003909	0.021708
T2S5	0.004345	0.001262	0.001374	0.024278	0.004345	0.018468	0.041667
T2S6	0.004723	0	0.000889	0.028317	0.002934	0.006992	0.015753
T2S7	0.004347	7.26E-05	0.000944	0.008257	0.023621	0.006138	0.006647
T2S8	0.020166	0	0.003149	0.029376	0.031994	0.017618	0.033963
T2S9	0.00392	0.040009	0.002394	0.028058	0.002531	0.019744	0.030616
T2S10	0.002031	0.048029	0.006333	0.008647	0.005416	0.020157	0.017886
T2S11	0.00269	0.000357	0.007186	0.005758	0.007691	0.008689	0.008321
T2S12	0.000318	0.00232	0.015411	0.042347	0.003719	0.040948	0.010763
T2S13	0.001455	0.083385	0.002644	0.023529	0.001455	0.018456	0.014849
T2S14	0	0.17147	0.017147	0.008131	0.001016	0.063014	0.075243
T2S15	0.000245	0	0.074699	0	0.002295	0.107871	0.0646
T2S16	0.000618	0	0.037117	0.001682	0.001938	0.072808	0.057348
T2S17	0.000447	0.000136	0.032054	0.002605	0.002313	0.097152	0.043892
T2S18	0.00334	0.000163	0.035926	0.00279	0.017841	0.079693	0.08456
T2S19	0.000452	0	0.073161	0.002009	0.002611	0.200653	0.154456
T2S20	0.000633	0	0.049153	0	0.000527	0.118416	0.112791
T2S21	0.001462	0	0.042535	0.004621	0.010705	0.147411	0.227483
T2S22	0.001741	0	0.044803	0.002919	0.01746	0.125141	0.171377
T2S23	0	0	0.063378	0.000588	0	0.21197	0.207191
T9S1	0.015616	0	0.001875	0.085031	0.007383	0.017073	0.073005
T9S2	0.000879	0	0	0	0.001641	0.000696	0.015618
T9S3	0.001538	0.001389	0	7.47E-05	0.001763	0.000792	0.017147
T9S4	0.001636	0	0	0.000239	0.017951	0.009574	0.000971
T9S5	0.034313	0	0.001031	0	0.021844	0.015213	0.004013
T9S6	0.037445	0	0.000809	0	0.10599	0.019096	0.002965
T9S7	0.003426	0	0.000162	0.000162	0.043782	0.006669	0.001358
T9S8	0.017541	0	0.005113	0.182231	0.004794	0.020098	0.05163
T9S9	0.05371	0	0.03027	0.044582	0.014623	0.014685	0.017852
T9S10	0.032414	0	0.025058	0.054096	0.01268	0.009377	0.01541
T9S11	0.047693	0	0.038427	0.097355	0.011994	0.024426	0.008545
T9S12	0.028546	0	0.006777	0.009802	0.037236	0.004656	0.006732
T9S13	0.019835	0	0.006016	0.023904	0.012839	0.013335	0.007654
T9S14	0.00449	0	0.018267	0.008183	0.011033	0.053895	0.024228
T9S15	0.002632	0	0.015938	0.003994	0.0113	0.047224	0.021127
T9S16	0.013519	0	0.001775	0.003758	0.013324	0.005063	0.00599

Supplemental Table 1. Cont.

Station	Thalassiosira sp.	Thalassiosira concaviuscula	Thalassiosira diporocyclus	Minidiscus sp.	Pseudo-nitzschia americana	Chaetoceros debilis	Chaetoceros
T2S1	0.002513	0.001145	0.008209	0.02534	0.03098	0.286642	0.003448
T2S2	0.010245	0.00307	0.047753	0.055945	0.083559	0.51832	0.003804
T2S3	0.001002	0.00061	0.006516	0.010147	0.020984	0.785052	0.002452
T2S4	0.008229	0.002918	0.062091	0.05806	0.138506	0.565965	0.005509
T2S5	0.010419	0.002808	0.129833	0.056705	0.137139	0.429446	0.004019
T2S6	0.008587	0.001993	0.057983	0.048384	0.125166	0.577253	0.004743
T2S7	0.026285	0.000605	0.004504	0.018355	0.024396	0.738834	0.003148
T2S8	0.115781	0.005719	0.041227	0.073587	0.085544	0.158766	0.003231
T2S9	0.009685	0.002394	0.058684	0.061598	0.129391	0.423989	0.003134
T2S10	0.011693	0.001269	0.039001	0.045391	0.047154	0.576515	0.003907
T2S11	0.011547	0.000704	0.068797	0.018029	0.048025	0.664443	0.007386
T2S12	0.003275	0.00062	0.258036	0.024876	0.179088	0.213369	0.009498
T2S13	0.003689	0.001363	0.027997	0.043542	0.101688	0.456104	0.004488
T2S14	0	0	0.141274	0.079538	0.070162	0.018262	0.001443
T2S15	0.000949	0.000337	0.477936	0.070292	0.053155	0.023165	0.001193
T2S16	0.001917	0.000809	0.474371	0.088354	0.092421	0.046998	0.002236
T2S17	0.003421	0.00449	0.480921	0.063699	0.074585	0.083915	0.00276
T2S18	0.010916	0.005723	0.230647	0.078491	0.0523	0.23472	0
T2S19	0.00226	0.000854	0.168265	0.116997	0.088426	0.038966	0.000954
T2S20	0.001231	0.004254	0.338408	0.095563	0.102173	0.030764	0.000492
T2S21	0.020843	0.002405	0.022022	0.131614	0.047251	0.147505	0
T2S22	0.011674	0.014951	0.052227	0.100922	0.055402	0.223605	0.000973
T2S23	0.000956	0.001691	0.202853	0.095949	0.060069	0.013308	0
T9S1	0.048795	0.068247	0.010295	0.268864	0.156941	0.078225	0
T9S2	0.005571	0.346304	0	0.153447	0.168087	0.203833	0
T9S3	0.007513	0.281792	0	0.156863	0.226617	0.215086	0
T9S4	0.108291	0.302679	0.000293	0.267748	0.049771	0.069849	0.001197
T9S5	0.223738	0.01856	7.93E-05	0.112837	0.05714	0.047479	0.024176
T9S6	0.177873	0.012606	0	0.090253	0.034024	0.07914	0.025025
T9S7	0.082315	0.323239	6.08E-05	0.192115	0.06841	0.094172	0.002939
T9S8	0.046836	0.028514	0.008664	0.19995	0.192849	0.115972	0.002592
T9S9	0.027569	0.001273	0.094846	0.084446	0.107451	0.190158	0.008445
T9S10	0.022099	0.000594	0.091719	0.072996	0.098387	0.350903	0.012555
T9S11	0.035828	0.000888	0.035545	0.071797	0.18605	0.213461	0.005508
T9S12	0.020019	0.00307	0.018166	0.080344	0.087106	0.403144	0.012412
T9S13	0.018111	0.002543	0.008249	0.078746	0.09223	0.499156	0.026745
T9S14	0.030848	0.007233	0.079119	0.210325	0.063075	0.152951	0.062676
T9S15	0.031139	0.005208	0.082283	0.204796	0.056076	0.150229	0.071958
T9S16	0.008012	0.002166	0.007125	0.031528	0.057248	0.699338	0.015111

Supplemental Table 2. Variables collected by the onboard flow through system (Temperature, Salinity, and Fluorescence) and macronutrients (Nitrate, Phosphate, and Silicate) collected and analyzed as per methods in chapter 2.

Station	Temp. (°C)	Salinity	Fluor. ($\mu g\ L^{-1}$)	NO_3 ($\mu mol\ kg^{-1}$)	PO_4 (µmol kg-1)	SiO_4 (µmol kg-1)
T2S1	10.53	33.764	20.667	6.84	0.75	14.14
T2S2	10.208	33.693	14.338	11.35	0.98	14.74
T2S3	10.594	33.772	22.509	13.67	1.24	18.74
T2S4	10.212	33.399	2.737	14.43	1.46	13.86
T2S5	10.755	33.301	1.358	14.48	1.23	11.08
T2S6	10.432	33.378	5.06	13.58	1.13	12.92
T2S7	11.31	33.662	7.259	9.82	1	10.64
T2S8	11.305	33.649	10.666	9.85	1.01	10.43
T2S9	10.937	33.349	4.734	12.38	1.07	10.33
T2S10	11.663	33.397	2.18	10.63	1.01	8.6
T2S11	11.743	33.353	6.108	8.53	0.81	4.21
T2S12	12.807	33.389	2.083	8.87	0.88	2.52
T2S13	11.308	33.291	8.189	9.33	0.86	6.47
T2S14	12.688	33.078	2.138	5.23	0.7	3.27
T2S15	13.917	32.962	1.08	4.28	0.56	2.36
T2S16	14.098	32.803	1.585	2.75	0.45	2.44
T2S17	14.488	32.771	1.683	2.19	0.4	2.34
T2S18	15.319	32.739	1.38	1.48	0.56	2.5
T2S19	15.797	32.748	1.644	0.51	0.32	2.75
T2S20	15.696	32.753	2.229	0.85	0.35	2.62
T2S21	16.008	32.74	1.287	0.1	0.3	2.76
T2S22	16.043	32.74	1.112	0.12	0.28	2.59
T2S23	16.029	32.745	1.163	0.12	0.29	2.59
T9S1	10.381	33.592	0.961	18.55	1.41	18.39
T9S2	10.408	33.608	3.043	19.97	1.49	22.74
T9S3	10.145	33.488	2.308	19.71	1.49	22.49
T9S4	10.398	33.205	0.962	14.56	1.18	16.52
T9S5	11.264	32.384	0.733	2.2	0.5	5.18
T9S6	11.943	32.33	0.708	0.57	0.38	3.5
T9S7	9.551	32.855	0.546	11.97	1.07	14.29
T9S8	10.894	33.475	1.104	15.5	1.17	16.73
T9S9	11.057	32.964	1.271	14.11	1.06	10.36
T9S10	10.997	33.125	1.546	10.23	0.84	6.8
T9S11	11.186	33.322	2.719	11.44	0.87	10.75
T9S12	11.856	32.819	2.926	6.65	0.59	1.8
T9S13	12.476	32.938	5.037	6.62	0.53	1.09
T9S14	13.118	32.611	2.112	4.38	NaN	5.09
T9S15	14.541	32.437	2.085	NaN	NaN	NaN
T9S16	13.676	32.54	2.132	NaN	NaN	NaN

B. SUPPLEMENTAL INFORMATION FOR CHAPTER III

The analysis and abbreviations in Supplemental Table 2 are explained as follows:

Sample_Name = Sample name including SK17 (For Sikuliaq 2017) S# for sample number and either S (surface) or C (chlorophyll max). For aligning with sequence samples submitted to NCBI

Date = sampling date in Month Day Year format

Time = time (UTC) in hour:minute:second format

Lat = Latitude in decimal degrees

Lon = Longitude in decimal degrees

CTD_Bottle = CTD bottle number that collected seawater sample

Station_Number = Cruise specific CTD station number

Description = Station descption (Transect_TransectStation_Occupation_depth)

Alexandrium_FlowCAM = Samples that had *Alexandrium* imaged during FlowCAM analysis

qPCR_Atamarense_mean = average concentrations of *A. tamarense* 28S gene copies per liter

qPCR_Atamarense_sd = standard deviation of *A. tamarense* 28S concentrations (gc/L)

Ratio_ATam_Phytos = number of 18S rRNA reads identified as *A. tamarense* / number of reads identified as belonging to eukaryotic phytoplankton

Volume_filtered = Volume of seawater sample filtered (mL)

Depth = Depth of water sample collected

Bottom_Depth = Station bathymetry (m)

Temp = CTD measured temperature (C) for this sample

Sal = CTD measured salinity (PSU) for this sample

Density = CTD measured density (kg/m3) for this sample

Fluroescence = CTD measured fluorescence (mg/m3)

Information on qPCR analysis:

BDL = below effective detection limit. DNQ = above effective detection limit but below effective limit of quantification ("did not quantify").

Effective Limits of detection and quantification

Theoretical LOD = 3 gc/rxn (Bustin et al 2009) --> anything above this can be reported as detectable but not quantifiable (DNQ)

effective LOD (gc/L SW) = (LOD/Vt) * vd/Vf

Vt = volume of DNA templated added to rxn (ul)

Vd = volume of entire DNA extract (ul)

Vf = volume of seawater filtered to obtain extract (L)

Theoretical LOQ = 10 gc/rxn

effective LOQ calculated as above for LOD

These ELOD and ELOQ values varied due to different sample filtration volumes but were in the range of 174-347 gc/L and 580-1157 gc/L, respectively.

(Bustin *et al.*, 2009; Biassoni and Raso, 2020)

Supplemental Table 3. CTD measurements, *Alexandrium* imaging and abundance (qPCR and 18S)

Sample Name	Date	Time	Lat (N)	Long	CTD_Bottle	Station Number	Description	*A.* in Flow-CAM	qPCR_Atamarense_mean	qPCR_Atamarense_sd
SK17S1S	8/29/2017	6:40	71.76914	-153.34	12	ctd001	Test_s	x	1.23E+10	9.81E+08
SK17S1C	8/29/2017	6:40	71.76914	-153.34	10	ctd001	Test_9	x	6.21E+10	5.14E+09
SK17S5S	8/30/2017	18:26	71.42427	-151.017	7	ctd005	2_2_A_Surf		33200000	2370000
SK17S5C	8/30/2017	18:26	71.4243	-151.017	5	ctd005	2_2_A_30		102000	49800
SK17S7S	8/30/2017	19:59	71.33325	-151.073	4	ctd007	2_4_A_Surf	x	3.11E+09	11600000
SK17S7C	8/30/2017	19:56	71.33322	-151.073	2	ctd007	2_4_A_29		1230000	295000
SK17S9S	8/30/2017	23:22	71.24314	-151.128	4	ctd009	2_6_A_Surf		7.68E+08	37900000
SK17S9C	8/30/2017	23:22	71.24314	-151.128	2	ctd009	2_6_A_23		1.22E+09	1.05E+08
SK17S11S	8/30/2017	1:30	71.15284	-151.184	4	ctd011	2_8_A_Surf		1.11E+09	28700000
SK17S11C	8/30/2017	1:30	71.15284	-151.184	2	ctd011	2_8_A_20		1.62E+08	20200000
SK17S13S	8/31/2017	3:56	71.0611	-151.243	4	ctd013	2_10_A_Surf	x	3.92E+09	90900000
SK17S13C	8/31/2017	3:56	71.0611	-151.243	2	ctd013	2_10_A_14	x	8.09E+09	4.15E+08
SK17S37S	9/1/2017	21:18	71.42577	-151.018	7	ctd037	2_2_B_Surf		4470000	125000
SK17S37C	9/1/2017	21:18	71.4261	-151.018	4	ctd037	2_2_B_34		2020000	590000
SK17S39S	9/2/2017	4:40	71.33304	-151.073	6	ctd039	2_4_B_Surf		55200	15600
SK17S39C	9/2/2017	4:40	71.33306	-151.073	2	ctd039	2_4_B_42		BDL	0
SK17S42S	9/2/2017	7:21	71.24283	-151.129	4	ctd042	2_6_B_Surf		3890000	333000
SK17S42C	9/2/2017	7:21	71.24286	-151.13	2	ctd042	2_6_B_30		4590000	342000
SK17S44S	9/2/2017	9:37	71.15228	-151.186	3	ctd044	2_8_B_Surf		6160000	149000
SK17S44C	9/2/2017	9:37	71.15228	-151.186	2	ctd044	2_8_B_24		18800000	624000
SK17S46S	9/2/2017	11:47	71.06153	-151.241	3	ctd046	2_10_B_Surf		483000	205000
SK17S46C	9/2/2017	11:47	71.06156	-151.241	2	ctd046	2_10_B_17		43400000	862000
SK17S53S	9/3/2017	8:35	71.42376	-151.017	3	ctd053	2_2_C_Surf		3280000	102000
SK17S53C	9/3/2017	8:35	71.42376	-151.017	2	ctd053	2_2_C_35		BDL	BDL
SK17S55S	9/3/2017	11:45	71.33356	-151.073	6	ctd055	2_4_C_Surf		BDL	BDL
SK17S55C	9/3/2017	11:45	71.33356	-151.073	5	ctd055	2_4_C_32		BDL	BDL
SK17S58S	9/3/2017	14:18	71.24278	-151.129	3	ctd058	2_6_C_Surf		914000	22100

Supplemental Table 3. Cont.

Sample Name	Date	Time	Lat (N)	Long	CTD_Bottle	Station Number	Description	*A.* in Flow-CAM	qPCR_Atamarense_mean	qPCR_Atamarense_sd
SK17S58C	9/3/2017	14:18	71.24278	-151.129	2	ctd058	2_6_C_38		261000	16600
SK17S60S	9/3/2017	16:32	71.15258	-151.183	3	ctd060	2_8_C_Surf		37100000	2890000
SK17S60C	9/3/2017	16:32	71.15258	-151.183	2	ctd060	2_8_C_25		2140000	190000
SK17S62S	9/3/2017	18:20	71.06146	-151.241	4	ctd062	2_10_C_Surf		4580000	236000
SK17S62C	9/3/2017	18:20	71.06146	-151.241	2	ctd062	2_10_C_18		7240000	1610000
SK17S72S	9/4/2017	14:41	71.42492	-151.016	3	ctd072	2_2_D_Surf		1870000	102000
SK17S72C	9/4/2017	14:42	71.42488	-151.016	2	ctd072	2_2_D_36		730000	156000
SK17S75S	9/5/2017	1:47	71.3336	-151.075	7	ctd075	2_4_D_Surf		1650000	97200
SK17S75C	9/5/2017	1:47	71.3336	-151.075	5	ctd075	2_4_D_24		BDL	BDL
SK17S78S	9/5/2017	4:18	71.24248	-151.129	4	ctd078	2_6_D_Surf		73500	77300
SK17S78C	9/5/2017	4:18	71.24248	-151.129	2	ctd078	2_6_D_29		BDL	BDL
SK17S80S	9/5/2017	6:34	71.15228	-151.185	4	ctd080	2_8_D_Surf		440000	208000
SK17S80C	9/5/2017	6:34	71.15228	-151.185	2	ctd080	2_8_D_29		114000	31400
SK17S82C	9/5/2017	8:51	71.06168	-151.241	4	ctd082	2_10_D_18		4450000	301000
SK17S82S	9/5/2017	8:51	71.06168	-151.241	6	ctd082	2_10_D_Surf		1320000	116000

Supplemental Table 3. Cont.

Sample_Name	Ratio_Atam_Phytos	Volume_filtered	Depth	Bottom_Depth	Temp	Sal	Density	Fluroescence
SK17S1S	0.48447	3200	3	160	5.0519	26.6586	1021.079	1.8257
SK17S1C	0.49819	2840	9	160	4.3334	28.9809	1023.013	3.0683
SK17S5S	0.102464	3475	3	376	4.9988	27.8004	1021.987	0.0382
SK17S5C	0.004493	3220	30	376	3.8709	31.2004	1024.918	0.9876
SK17S7S	0.462613	4060	3	157	4.806	28.2968	1022.399	0.1216
SK17S7C	0.004638	3820	29	157	3.3404	31.1861	1024.949	0.9509
SK17S9S	0.414179	4000	3	56	4.7976	28.7117	1022.728	0.0832
SK17S9C	0.305371	4180	23	56	6.3264	31.3483	1024.735	0.9828
SK17S11S	0.381761	4050	3	36	4.3546	29.4544	1023.359	0.1593
SK17S11C	0.083894	3200	20	36	4.0552	31.1415	1024.806	1.1041
SK17S13S	0.456281	4270	5	21	4.3113	29.2018	1023.172	0.2239
SK17S13C	0.485309	3880	14	21	3.157	29.8631	1023.84	0.5724
SK17S37S	0.004119	4290	3	376	4.7066	28.216	1022.344	0.0103
SK17S37C	0.004085	4310	34	376	-0.1412	30.5279	1024.666	0.431
SK17S39S	0.001744	4180	4	157	5.3664	28.0736	1022.171	0.2952
SK17S39C	0.002461	4300	42	157	-0.0342	30.9177	1025.015	0.4664
SK17S42S	0.009002	4100	3	56	5.2225	28.3263	1022.381	0.298
SK17S42C	0.008739	3780	30	56	0.04	30.2789	1024.439	0.521
SK17S44S	0.014225	3960	3	36	4.5379	29.076	1023.042	0.2966
SK17S44C	0.025622	3040	24	36	2.434	31.123	1024.949	0.9058
SK17S46S	0.007209	3400	3	21	4.3499	29.5222	1023.413	0.3399
SK17S46C	0.019132	2300	17	21	2.5371	30.6234	1024.509	0.9554
SK17S53S	0.012794	4080	3	376	5.4825	27.3247	1021.563	0.311
SK17S53C	0.005524	3920	35	376	-0.3562	30.3635	1024.546	0.5128
SK17S55S	0.000713	4150	3	157	4.0059	28.1522	1022.358	0.3808
SK17S55C	0.000489	4100	32	157	-0.0364	30.2954	1024.465	0.438
SK17S58S	0.002577	4240	4	56	5.1164	28.6501	1022.652	0.3052

Supplemental Table 3. Cont.

Sample_Name	Ratio_Atam_Phytos	Volume_filtered	Depth	Bottom_Depth	Temp	Sal	Density	Fluroescence
SK17S58C	0.00034	4240	38	56	3.0133	31.2063	1025.035	0.5745
SK17S60S	0.147599	4200	3	36	4.3444	29.2926	1023.232	0.2523
SK17S60C	0.002623	3320	25	36	1.74	30.8733	1024.803	0.9877
SK17S62S	0.02296	4300	3	21	4.3266	29.1959	1023.157	0.187
SK17S62C	0.003317	2500	18	21	2.7302	30.7907	1024.633	0.8427
SK17S72S	0.005708	4200	4	376	5.5443	26.6694	1021.044	0.4675
SK17S72C	0.003318	4170	36	376	2.2342	31.0341	1024.949	0.4458
SK17S75S	0.002169	4100	4	157	5.4644	27.1192	1021.407	0.2363
SK17S75C	0	3940	24	157	2.2789	29.316	1023.516	0.4995
SK17S78S	0.001106	4330	4	56	4.9652	28.5444	1022.584	0.3051
SK17S78C	0.001621	4050	29	56	0.2967	30.348	1024.479	0.4022
SK17S80S	0.002035	4350	3	36	4.4909	28.808	1022.834	0.261
SK17S80C	0	3900	29	36	2.6092	31.0097	1024.869	1.1988
SK17S82C	0.003744	2160	18	21	1.2779	30.8162	1024.753	1.0514
SK17S82S	0.003357	3980	3	21	3.583	29.79	1023.695	0.4186

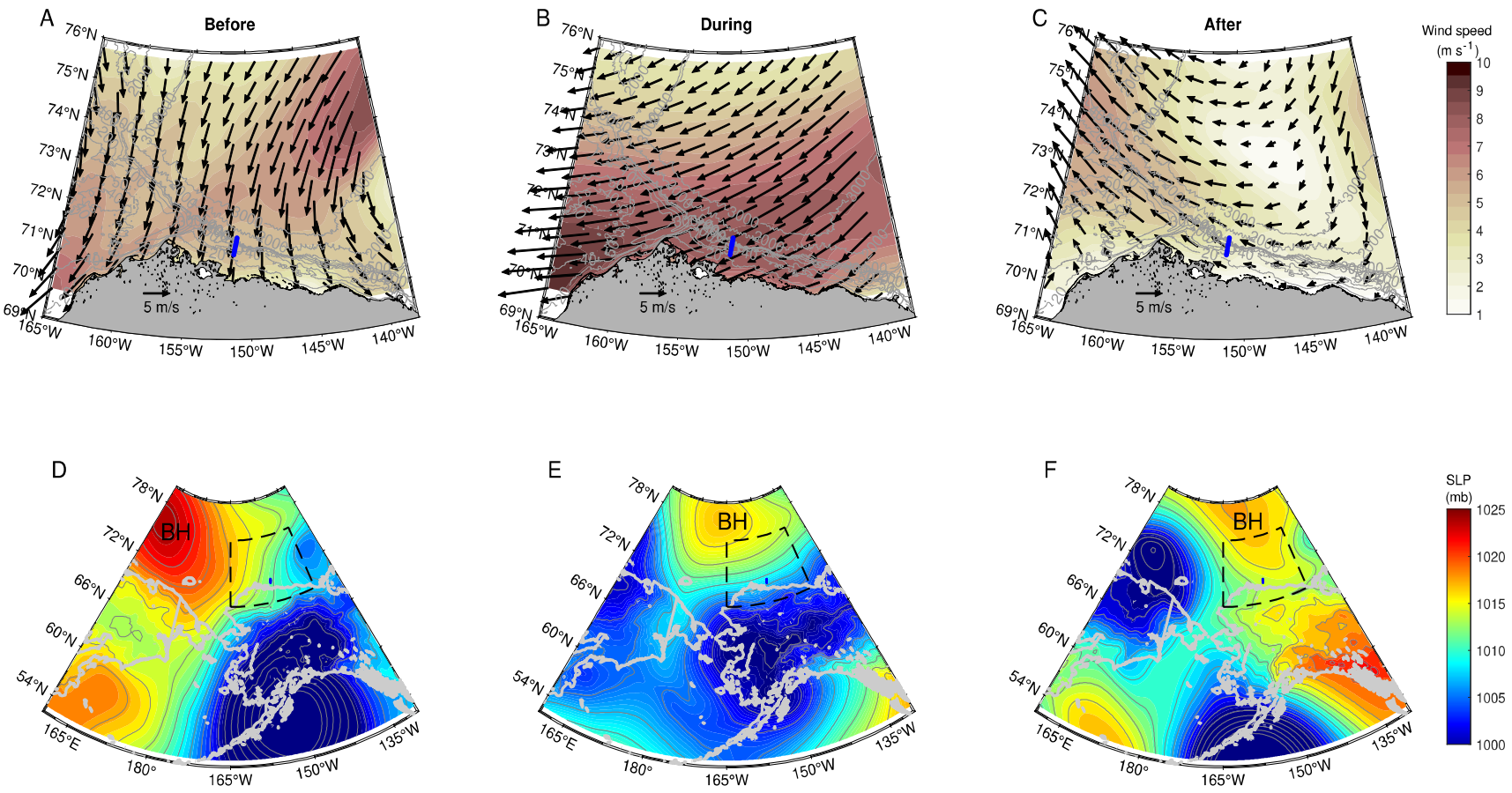

Supplemental Fig. 1. 10-m winds and sea-level pressure for the period before the upwelling (29-30 Aug), during the upwelling (31 Aug – 1 Sep), and after the upwelling (3 Sep). The top row shows the wind vectors and speed (color) in the western Beaufort / eastern Chukchi Seas. The blue dots are the stations of the repeat transect. The bottom row shows the sea-level pressure over a larger domain. The black dashed box is the domain shown in the top row. The center of the Beaufort High (BH) is indicated.

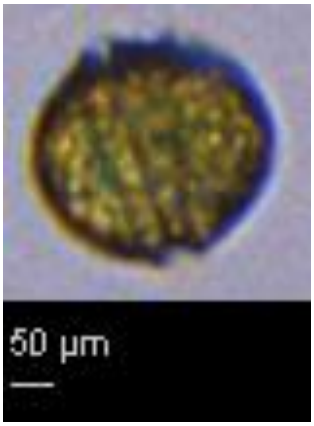

Supplemental Fig. 2. *Alexandrium spp*. images taken during FlowCAM analysis.

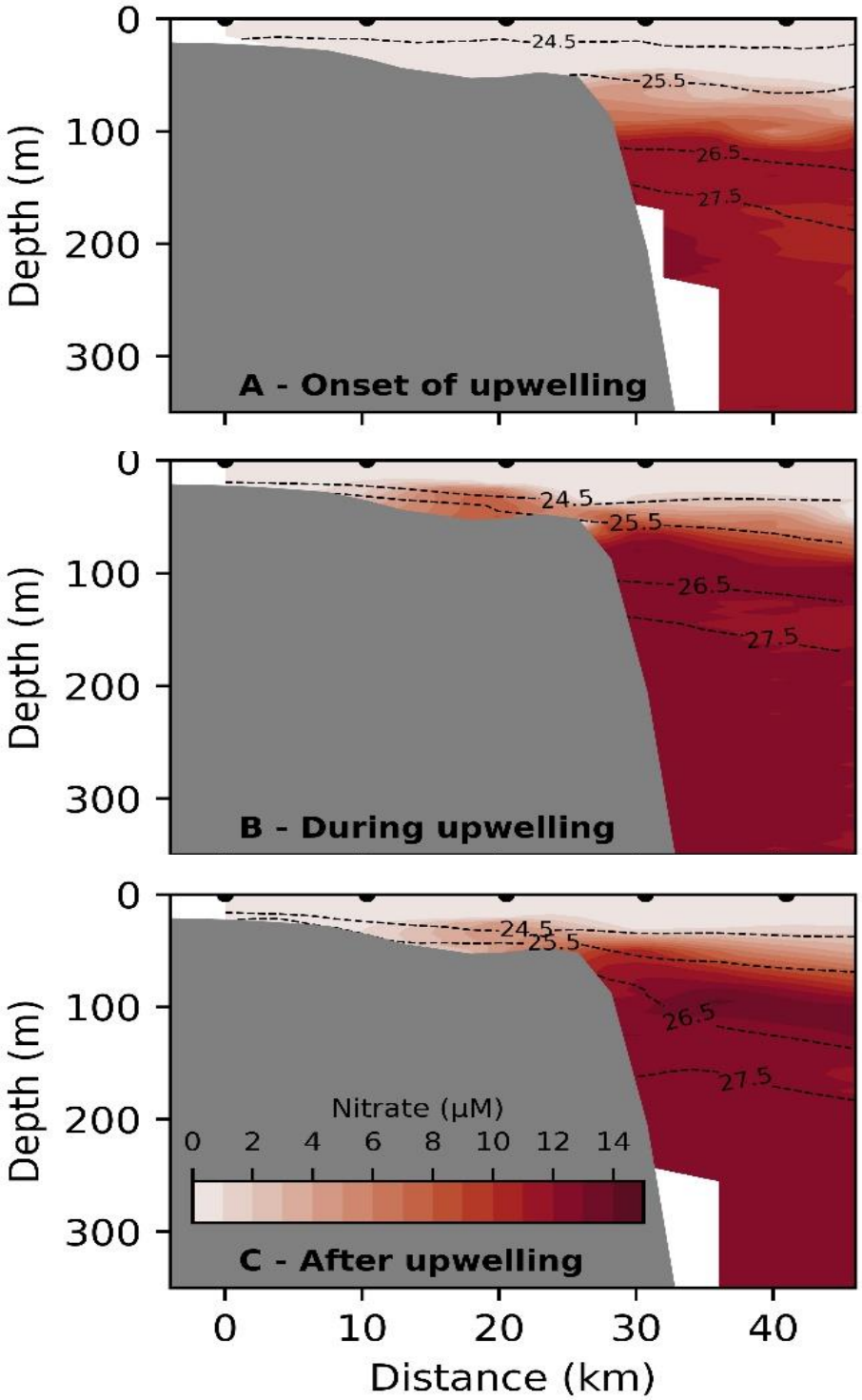

Supplemental Fig. 3. Vertical sections of nitrate (color, µM) measured by the SUNA V2 sensor, with potential density contours overlain (kg m^{-3}). A. onset of upwelling, B. during upwelling, and C. after upwelling. Transect occupation D is not shown due to fewer casts with the SUNA sensor.

C. SUPPLEMENTAL INFORMATION FOR CHAPTER IV

Supplemental Table 4. All surface station parameters, including location, corresponding CTD station, and CTD measured temperature, salinity, density, fluorescence, PAR, and phytoplankton groups from 18S sequencing (Diatoms, Dinoflagellates, Haptophytes, Other) as a proportion of a whole.

ShortName	26 Isopyc	CTD	Bottom (m)	Station Name	Lat (N)	Long	Temp (°C)
2.2.A	NaN	ctd005	378	2_2_A_Surf	71.42427	-151.017	4.9988
2.4.A	NaN	ctd007	157	2_4_A_Surf	71.33325	-151.073	4.806
2.6.A	Below	ctd009	54	2_6_A_Surf	71.24314	-151.128	4.7976
2.8.A	Below	ctd011	36	2_8_A_Surf	71.15284	-151.184	4.3546
2.10.A	Below	ctd013	21	2_10_A_Surf	71.0611	-151.243	4.3113
4.1.A	NaN	ctd020	1350	4_1_A_Surf	71.40815	-150.186	4.6712
4.3.A	NaN	ctd022	1180	4_3_A_Surf	71.31768	-150.229	5.308
4.5.A	NaN	ctd024	147	4_5_A_Surf	71.228	-150.287	4.6208
4.7.A	Above	ctd026	47	4_7_A_Surf	71.13824	-150.345	4.8235
2.2.B	NaN	ctd037	378	2_2_B_Surf	71.42577	-151.018	4.7066
2.4.B	NaN	ctd039	157	2_4_B_Surf	71.33304	-151.073	5.3664
2.6.B	Above	ctd042	54	2_6_B_Surf	71.24283	-151.129	5.2225
2.8.B	Above	ctd044	36	2_8_B_Surf	71.15228	-151.186	4.5379
2.10.B	Above	ctd046	21	2_10_B_Surf	71.06153	-151.241	4.3499
2.2.C	NaN	ctd053	371	2_2_C_Surf	71.42376	-151.017	5.4825
2.4.C	NaN	ctd055	157	2_4_C_Surf	71.33356	-151.073	4.0059
2.6.C	Below	ctd058	54	2_6_C_Surf	71.24278	-151.129	5.1164
2.8.C	Below	ctd060	36	2_8_C_Surf	71.15258	-151.183	4.3444
2.10.C	Below	ctd062	21	2_10_C_Surf	71.06146	-151.241	4.3266
2.2.D	NaN	ctd072	377	2_2_D_Surf	71.42492	-151.016	5.5443
2.4.D	NaN	ctd075	157	2_4_D_Surf	71.3336	-151.075	5.4644
2.6.D	Below	ctd078	54	2_6_D_Surf	71.24248	-151.129	4.9652
2.8.D	Below	ctd080	36	2_8_D_Surf	71.15228	-151.185	4.4909
2.10.D	Below	ctd082	21	2_10_D_Surf	71.06168	-151.241	3.583
4.4.B	NaN	ctd086	877	4_4_B_Surf	71.27356	-150.255	5.0842
4.5.B	NaN	ctd087	147	4_5_B_Surf	71.2281	-150.285	5.4313
4.6.B	Below	ctd089	52	4_6_B_Surf	71.18292	-150.314	4.0706
4.8.B	Below	ctd091	34	4_8_B_Surf	71.09266	-150.374	3.151
4.10.B	Below	ctd093	24	4_10_B_Surf	71.00256	-150.434	3.1777
6.4.A	NaN	ctd108	182	6_4_A_Surf	71.21091	-149.432	3.3744
6.6.A	Above	ctd111	44	6_6_A_Surf	71.12458	-149.5	1.0401
6.8.A	Above	ctd113	33	6_8_A_Surf	71.03819	-149.565	1.9831
6.10.A	Above	ctd115	29	6_10_A_Surf	70.94537	-149.626	1.7576
5.2.A	NaN	ctd128	1440	5_2_A_Surf	71.33252	-149.784	1.7595
5.45.A	NaN	ctd131	208	5_45_A_Surf	71.21956	-149.862	2.6021
5.6.A	Above	ctd133	49	5_6_A_Surf	71.15446	-149.908	2.8631
5.8.A	Above	ctd135	31	5_8_A_Surf	71.06497	-149.967	1.9491
5.10.A	Above	ctd137	26	5_10_A_Surf	70.97357	-150.031	2.1807
2.10.E	Above	ctd138	22	2_10_E_Surf	71.06132	-151.242	1.6887
2.8.E	Above	ctd140	36	2_8_E_Surf	71.15196	-151.185	2.0511

Supplemental Table 4 Cont.

Short Name	Salinity	σ_t (kg m^{-3})	Fluro. (mg m^{-3})	PAR	Haptophytes	Dinoflagellates	Diatoms	Other
2.2.A	27.8004	21.973	0.0382	205.46	0.030146	0.734219	0.064823	0.170812
2.4.A	28.2968	22.3847	0.1216	430.59	0.00325	0.974869	0.006268	0.015612
2.6.A	28.7117	22.7139	0.0832	302.33	0.007563	0.928392	0.018683	0.045362
2.8.A	29.4544	23.3451	0.1593	157.44	0.011116	0.879223	0.058035	0.051626
2.10.A	29.2018	23.1488	0.2239	104.64	0.008803	0.933394	0.023542	0.034262
4.1.A	27.3213	21.6247	0.1628	6.9394	0.036613	0.719407	0.114942	0.129038
4.3.A	27.9242	22.0401	0.0758	302.89	0.023857	0.763178	0.143182	0.069783
4.5.A	28.975	22.9397	0.1525	73.144	0.022582	0.755577	0.115874	0.105967
4.7.A	28.8427	22.8152	0.2195	1.3388	0.023824	0.730336	0.130457	0.115383
2.2.B	28.216	22.3302	0.0103	643.63	0.036523	0.50561	0.325154	0.132714
2.4.B	28.0736	22.1522	0.2952	78.329	0.034435	0.562419	0.311593	0.091553
2.6.B	28.3263	22.3667	0.298	0.64084	0.0325	0.53336	0.338586	0.095554
2.8.B	29.076	23.0276	0.2966	0.59851	0.02721	0.595666	0.264093	0.113031
2.10.B	29.5222	23.3993	0.3399	0.62403	0.017027	0.755061	0.140533	0.087379
2.2.C	27.3247	21.5486	0.311	0.60313	0.036506	0.423951	0.435978	0.103566
2.4.C	28.1522	22.344	0.3808	0.52104	0.024663	0.645572	0.238095	0.091671
2.6.C	28.6501	22.6334	0.3052	0.63485	0.024315	0.613146	0.280932	0.081608
2.8.C	29.2926	23.2176	0.2523	37.243	0.029334	0.691634	0.144554	0.134479
2.10.C	29.1959	23.1426	0.187	231.66	0.021024	0.673118	0.226361	0.079496
2.2.D	26.6694	21.025	0.4675	1.19	0.023871	0.697055	0.217359	0.061715
2.4.D	27.1192	21.3882	0.2363	297.26	0.029002	0.552201	0.332497	0.086299
2.6.D	28.5444	22.565	0.3051	60.411	0.023543	0.668347	0.253076	0.055033
2.8.D	28.808	22.8197	0.261	1.8099	0.014456	0.568609	0.343524	0.073411
2.10.D	29.79	23.681	0.4186	0.54355	0.020208	0.58075	0.223366	0.175676
4.4.B	25.2325	19.9343	0.442	0.59845	0.056966	0.622951	0.176554	0.143529
4.5.B	25.4334	20.0604	0.4836	0.3394	0.034783	0.755368	0.090195	0.119654
4.6.B	27.4906	21.8123	0.3342	1.7695	0.024489	0.417602	0.476099	0.081809
4.8.B	29.361	23.3749	0.2209	51.664	0.018928	0.542103	0.365713	0.073256
4.10.B	29.7308	23.6673	0.3387	98.755	0.022105	0.503004	0.353245	0.121646
6.4.A	27.7699	22.0907	0.3445	62.818	0.023773	0.492402	0.383265	0.10056
6.6.A	28.8922	23.1349	0.1283	174.11	0.022366	0.558036	0.298715	0.120882
6.8.A	29.1746	23.3086	0.5137	99.101	0.022708	0.57612	0.313498	0.087674
6.10.A	29.1849	23.3306	0.2866	58.292	0.031687	0.508014	0.314776	0.145524
5.2.A	28.4291	22.7253	0.222	1.2583	0.017598	0.610885	0.267662	0.103854
5.45.A	28.0817	22.3949	0.3192	124.79	0.022555	0.547982	0.339488	0.089975
5.6.A	28.21	22.4792	0.1569	349.82	0.011648	0.644001	0.290615	0.053736
5.8.A	28.8822	23.0768	0.1269	308.94	0.02041	0.587047	0.309191	0.083352
5.10.A	29.1139	23.2474	0.2477	163.66	0.020121	0.446723	0.406828	0.126329
2.10.E	30.3902	24.3002	1.0367	0.003133	0.026982	0.375374	0.358273	0.239371

Supplemental Table 4 Cont.

Short Name	Salinity	σ_t (kg m^{-3})	Fluro. (mg m^{-3})	PAR	Haptophytes	Dinoflagellates	Diatoms	Other
2.8.E	29.757	23.7701	0.7261	0.096406	0.04318	0.425724	0.283243	0.247853
2.6.E	29.266	23.3956	0.6531	0.34283	0.020656	0.62153	0.253327	0.104487
2.45.E	27.9063	22.2454	0.3473	0.25074	0.018803	0.500017	0.390297	0.090883
2.3.E	27.6498	22.0716	0.2732	0.26092	0.030215	0.551632	0.234196	0.183957

Supplemental Table 5. Relative abundance of phytoplankton genera and groups for each shelf and shelfbreak station (>120 m bottom depth).

Short Name	Chaetoceros	Leptocylindrus	Minidiscus	Thalassiosira	Skeletonema	Other Diatoms	Micromonas
2.10.B	0.062419	0.003554	0.014299	0.018825	0.003913	0.037524	0.063858
4.7.A	0.035672	0.013988	0.020918	0.010571	0.002778	0.04653	0.068183
2.6.A	0.009326	0.002163	0.000849	0	0.000609	0.005736	0.01479
2.10.A	0.01322	0.001902	0.001411	0	0.00115	0.005859	0.011165
2.8.A	0.032319	0.004144	0.004996	0.002474	0.001333	0.01277	0.020464
2.10.E	0.180959	0.034046	0.002012	0.015156	0.013726	0.112375	0.157621
2.8.E	0.175265	0.069745	0.001007	0.001629	0.005716	0.029882	0.154623
2.6.D	0.035678	0.20582	0	0	0.002649	0.00893	0.010041
2.6.E	0.048449	0.142427	0	0.001837	0.0081	0.052514	0.060253
5.10.A	0.118762	0.222678	0	0.000501	0.012053	0.052834	0.063078
6.6.A	0.073837	0.183982	0	0.000954	0.006901	0.033042	0.066144
6.10.A	0.060447	0.21433	0	0.001029	0.008553	0.030417	0.077456
5.8.A	0.047173	0.216378	0	0.000856	0.008966	0.035819	0.039581
6.8.A	0.078491	0.182412	0	0.001469	0.007547	0.043578	0.043228
5.6.A	0.035694	0.22234	0	0.000723	0.0077	0.024158	0.018931
4.6.B	0.023484	0.43606	0	0.000342	0.005818	0.010395	0.020811
2.45.E	0.031983	0.326398	0	0.00064	0.00845	0.022826	0.030637
2.10.D	0.146334	0.038722	0.001446	0.001653	0.006116	0.029093	0.08947
4.10.B	0.167153	0.155976	0.000801	0.000896	0.007152	0.021266	0.066945
4.8.B	0.146701	0.198362	0	0	0.004791	0.01586	0.028863
2.6.B	0.096116	0.229316	0	0	0.003216	0.009938	0.025971
2.8.D	0.070696	0.257115	0	0	0.004274	0.011439	0.020691
2.6.C	0.066934	0.198272	0	0	0.003931	0.011794	0.022912
2.10.C	0.091624	0.110837	0.000941	0.000107	0.003676	0.019177	0.022285
2.8.B	0.094432	0.151866	0	0	0.002784	0.015011	0.030855
2.8.C	0.05479	0.067295	0.000315	0.000186	0.002356	0.019611	0.042711

Supplemental Table 5 Cont.

Short Name	Other Stramenopiles	Bathycoccus	Other Chlorophytes	Haptophytes	Alexandrium	Prorocentrum	Pentapharsodinium	Other Dinoflagellates
2.10.B	0.011697	0.006917	0.004907	0.017027	0.006346	0.424773	0.028576	0.295366
4.7.A	0.016958	0.025133	0.00511	0.023824	0.023026	0.41989	0.050299	0.237122
2.6.A	0.00681	0.020926	0.002836	0.007563	0.682578	0.127145	0.05379	0.064878
2.10.A	0.006564	0.013189	0.003343	0.008803	0.811775	0.072281	0.010782	0.038556
2.8.A	0.008562	0.018488	0.004112	0.011116	0.600353	0.157016	0.04247	0.079383
2.10.E	0.031251	0.02269	0.027809	0.026982	0	0.173135	0.041244	0.160996
2.8.E	0.030178	0.035628	0.027424	0.04318	0.002428	0.179915	0.032074	0.211307
2.6.D	0.011451	0.024398	0.009144	0.023543	0.023757	0.277987	0.082849	0.283755
2.6.E	0.013671	0.01364	0.016923	0.020656	0.008552	0.156399	0.051882	0.404697
5.10.A	0.022258	0.025435	0.015558	0.020121	0.007625	0.148182	0.038817	0.252099
6.6.A	0.016359	0.025228	0.013152	0.022366	0.015039	0.179091	0.039435	0.324471
6.10.A	0.024082	0.022202	0.021784	0.031687	0.003183	0.183335	0.046991	0.274504
5.8.A	0.015341	0.018518	0.009912	0.02041	0.013021	0.190764	0.052872	0.33039
6.8.A	0.012372	0.01481	0.017264	0.022708	0.007898	0.152959	0.065468	0.349796
5.6.A	0.009035	0.015039	0.010731	0.011648	0.036667	0.133604	0.088152	0.385578
4.6.B	0.012576	0.034328	0.014095	0.024489	0.019142	0.137675	0.032253	0.228532
2.45.E	0.01313	0.033397	0.013719	0.018803	0.027623	0.146484	0.049625	0.276285
2.10.D	0.027523	0.046739	0.011943	0.020208	0.020746	0.320977	0.052194	0.186834
4.10.B	0.019111	0.022525	0.013065	0.022105	0.030745	0.264691	0.039519	0.168049
4.8.B	0.016827	0.017158	0.010408	0.018928	0.025866	0.202752	0.059025	0.25446
2.6.B	0.015004	0.046619	0.00796	0.0325	0.024765	0.255512	0.052794	0.200289
2.8.D	0.012394	0.031175	0.009151	0.014456	0.021445	0.199341	0.086509	0.261313
2.6.C	0.013347	0.037361	0.007988	0.024315	0.032954	0.241117	0.066283	0.272793
2.10.C	0.016336	0.030772	0.010104	0.021024	0.055933	0.292221	0.096756	0.228208
2.8.B	0.019834	0.051177	0.011165	0.02721	0.033238	0.337916	0.060075	0.164437
2.8.C	0.021467	0.052174	0.018127	0.029334	0.163571	0.312837	0.068315	0.14691

VITA

Sveinn V. Einarsson

Department of Ocean and Earth Sciences
Old Dominion University
4600 Elkhorn Ave
Norfolk, VA 23529

Education

2018-2021	Doctor of Philosophy, Oceanography, Old Dominion University, Norfolk, Virginia, USA
2018	Master of Science, Ocean and Earth Science, Old Dominion University, Norfolk, Virginia, USA Degree Granted: June 2018
2016	Bachelor of Science – *cum laude*, Major: Ocean and Earth Science, Minor: Computer Engineering, Old Dominion University, Norfolk, Virginia, USA Degree Granted: June 2016
2013 - 2014	FAA Private Pilot License, Epix Aviation, Chesapeake, Virginia, USA License Granted: June 2014
2012	Emergency Medical Technician, University of Iowa Hospitals and Clinics, Iowa City, Iowa, USA Degree Granted: July 2012
2007 - 2011	Matricular Examination with Physics concentration, Verslunarskóli Íslands (Commercial College of Iceland), Reykjavik, Iceland Degree Granted: May 2011

Conference Presentations (As first author)

Sveinn Einarsson, Kate Lowry, Carin Ashjian, Robert Pickart, P. Dreux Chappell. Alexandrium in the Arctic: Are harmful algae spreading as the Arctic warms. Graduate Research Achievement Day, March 2021, Old Dominion University, Norfolk, Virginia, USA. (Poster Presentation)

Sveinn Einarsson, Kate Lowry, Carin Ashjian, Robert Pickart, P. Dreux Chappell. Beaufort Sea Upwelling and Corresponding Shifts in the Eukaryotic Community. Presented at 2020 Ocean Science Meeting, San Diego, CA, 16-21 Feb. (Oral Presentation)

Sveinn Einarsson, Zuzanna M Abdala, Kimberly Powell, Claire P. Till, Dreux Chappell. High and Low Iron Upwelling and Corresponding Shifts in the Diatom Community. Presented at 2018 Ocean Sciences Meeting, Portland, OR, 12-16 Feb. (Oral Presentation)

Sveinn Einarsson, Zuzanna M. Abdala, Kimberly Powell, P. Dreux Chappell. Diatom community composition through upwelling over thin and broad continental shelves. Ocean Carbon and Biogeochemistry Workshop, 26-29 June 2017, Woods Hole, Massachusetts, USA. (Poster Presentation)

Sveinn Einarsson, Zuzanna M. Abdala, Kimberly Powell, Benjamin Twining, Claire P. Till, Tyler Coale, P. Dreux Chappell. Diatom community composition along Oregon Coast upwelling in relation to environmental variables. Ocean Carbon and Biogeochemistry Workshop, 25-28 July 2016, Woods Hole, Massachusetts, USA. (Poster Presentation)